

**Scientific and Technological Alliance for
Guaranteeing the European Excellence in
Concentrating Solar Thermal Energy**



FP7 Grant Agreement number: 609837
Start date of project: 01/02/2014
Duration of project: 48 months

Project Deliverable 7.12:

**Performance comparison of
advanced thermal energy storage
systems through simulations**

WP7 – Task 7.3.7	Deliverable 7.12
Due date:	July/2017
Submitted	July/2017
Partner responsible	CENER
Person responsible	Fritz Zaversky
Author(s):	Fritz Zaversky (CENER), Bernhard Seubert (Fraunhofer ISE), Jiahui Lu (Fraunhofer ISE), Martin Karl (Fraunhofer ISE), Ralf Müller (Fraunhofer ISE), Thomas Fluri (Fraunhofer ISE), Alaric Montenon (Cyprus Institute), Luis Guerreiro (Uni Evora), Diogo Canavarro (Uni Evora), Manuel Collares Pereira (Uni Evora)
Document version:	7
Reviewed/supervised by:	Marcelino Sanchez
Dissemination Level	PU

1. Table of contents	
2. Introduction	7
3. Transient response simulation of a passive sensible heat storage system and the comparison to a conventional active indirect two-tank unit (CENER)	7
3.1 Passive sensible heat storage and its modeling	7
3.1.1 Development of a specific heat transfer correlation for Therminol VP1 .	13
3.1.2 Model validation against experimental data	15
3.1.3 Up-scaling and typical simulation results	19
3.2 Modeling of the conventional active indirect two-tank heat storage	26
3.3 Comparison of the transient response of both heat storage systems for idealized changes in load	29
3.4 The impact of the HTF outlet temperature characteristics on the power cycle downstream	38
3.4.1 Rankine steam cycle configuration and its modeling	41
3.4.2 Impact of the storage units' outlet temperature characteristic on power cycle and the electric energy output	42
3.5 Conclusions and outlook	45
4. Performance comparison of advanced thermal energy storage systems through simulations (FISE)	48
4.1 Technology overview and configurations	48
4.2 System design and cost assumptions	48
4.3 Simulation and operating strategy	53
4.4 Result	54
4.5 Conclusion	62
5. Influence of heat source location on the efficiency of small molten salts based storage for steam generation with direct immersed helical coil at steady-state (CyI)....	63
5.1 Description of the systems	63
5.2 Simulation results	65
5.2.1 Comparison with different location	65
5.2.2 Comparison with a smaller tank	67
5.3 Conclusion	69
6. Design of a Fresnel Concentrator Type Collector (Uni Evora)	70
7. References	75

Figures

Figure 1: Concrete module layout with dimensions according to Refs. [2, 4, 5]	8
Figure 2: Finite volume discretization scheme according to the staggered grid approach [11]	10
Figure 3: Modelica concrete TES model scheme	11
Figure 4: Cylindrical conduction model scheme (example for steel tube).....	11
Figure 5: Gnielinski correlation (gray) vs. simulated data points in ANSYS Fluent (green dots).....	14
Figure 6: The proposed correlation (Eq. (16) - red) vs. simulated data points in ANSYS Fluent (green dots) [18]	15
Figure 7: Storage module inlet and outlet temperature – measured inlet temperature (black solid), measured outlet temperature (red solid), simulated outlet temperature (black dashed).....	17
Figure 8: Storage module mass flow rate	18
Figure 9: Reynolds number of fluid flow in tubes – first control volume (black solid), last control volume (black dashed).....	18
Figure 10: Forced convective heat transfer coefficient between fluid and tubes inner wall – first control volume (black solid), last control volume (black dashed)	19
Figure 11: Module mass flow rate of grid independence test A (at constant inlet temperature of 391 °C)	20
Figure 12: Module cold end temperatures of grid independence test A.....	20
Figure 13: Module inlet temperature of grid independence test B (at constant mass flow rate of 600 kg/s).....	21
Figure 14: Module outlet temperatures of grid independence test B	21
Figure 15: Hot (red) and cold (blue) end temperature of periodic simulation to reach periodic steady state – dot-dashed line: solar field outlet temperature – dashed line: steam generator return temperature	23
Figure 16: Center fluid (CV 150) temperature evolution during periodic simulation ...	24
Figure 17: Periodic mass flow rate through concrete TES system according to cut-off temperature conditions	24
Figure 18: Longitudinal temperature profile evolution, starting at switching time ($t = 0$ s) from discharging to charging.....	25
Figure 19: Conventional active indirect two-tank TES system layout [25]	26
Figure 20: Conventional active indirect two-tank TES system model scheme in Modelica [24]	28
Figure 21: Idealized HTF mass flow rate boundary for the TES system (charging positive, discharging negative).....	29
Figure 22: Molten salt mass flow rate according to idealized HTF mass flow boundary (see Figure 20 for positive flow directions).....	30
Figure 23: Molten salt temperature at heat exchanger outlet (hot storage tank inlet) – first charging interval.....	31

Figure 24: HTF outlet temperature (cold side) during first charging interval – two tank (black) and concrete (red).....	31
Figure 25: HTF outlet temperature (cold side) during second charging interval – two tank (black) and concrete (red).....	32
Figure 26: HTF outlet temperature (hot side) during first discharging interval – two tank (black) and concrete (red) – 3 °C per minute rate-of-change limit (blue dashed) – 2 °C per minute rate-of-change limit (blue dotted).....	34
Figure 27: HTF outlet temperature (hot side) during second discharging interval – two tank (black) and concrete (red) – 3 °C per minute rate-of-change limit (blue dashed) – 2 °C per minute rate-of-change limit (blue dotted).....	34
Figure 28: Temperature plot of radial conduction nodes in the concrete layer (concrete node 1 to concrete node 25) and the corresponding HTF control volume (blue) temperature at the center of the module (CV 150)	35
Figure 29: Reynolds number in the center (CV 150) of the concrete storage unit.....	36
Figure 30: Nusselt number in the center (CV 150) of the concrete storage unit.....	36
Figure 31: Forced convective heat transfer coefficient in the center (CV 150) of the concrete storage unit.....	37
Figure 32: Storage system HTF outlet temperatures: two-tank TES (black) and concrete TES (red)	39
Figure 33: Rankine cycle model – 350 °C HTF inlet temperature – Live steam conditions: 72 bar, 343 °C	40
Figure 34: Thermal power to power cycle: two-tank TES (black), concrete TES (red)	43
Figure 35: Thermal energy discharged to power cycle: two-tank TES (black), concrete TES (red)	43
Figure 36: Power cycle net conversion efficiencies: two-tank TES (black), concrete TES (red)	44
Figure 37: Power cycle electric power output: two-tank TES (black), concrete TES (red)	44
Figure 38: Electric energy generated: two-tank TES (black), concrete TES (red).....	45
Figure 39: Layout of the reference system	50
Figure 40: Layout for the systems using salt as HTF	50
Figure 41: Operating strategy for the annual simulations	54
Figure 42: Relative LCOE for reference system PTC-NS-VP1-TTID at different storage sizes and SM.....	55
Figure 43: Relative LCOE for configuration PTC+NS+SS+TTD at different storage sizes and SM.....	55
Figure 44: Relative LCOE for configuration PTC+NS+SS+STD at different storage sizes and SM.....	56
Figure 45: Relative LCOE for configuration LFC+NS+SS+TTD at different storage sizes and SM.....	56
Figure 46: Relative LCOE for configuration LFC+EW+SS+TTD at different storage sizes and SM.....	57
Figure 47: Relative LCOE for configuration PTC+NS+Hitec+TTD at different storage sizes and SM.....	57

Figure 48: Relative LCOE for configuration PTC-NS-Hitec-STD at different storage sizes and SM.....	58
Figure 49: Relative LCOE for configuration LFC-NS-Hitec-TTD at different storage sizes and SM.....	58
Figure 50: Relative LCOE for configuration LFC-EW-Hitec-TTD at different storage sizes and SM.....	59
Figure 51: Max. SOC level throughout the year	61
Figure 52. TESLAB tank (left) and drawing of the helical coil (right).....	63
Figure 53. Simulation Studio template of TESLAB facility	63
Figure 54. Comparison of the outlet steam temperatures (with different locations of the heaters).....	65
Figure 55. Duty cycle of the heaters.....	66
Figure 56. Nodal temperature with bottom configuration.....	66
Figure 57. Nodal temperatures with top configuration	67
Figure 58. Comparison of the outlet steam temperatures (with reduced tank).....	68
Figure 59. Nodal temperatures with reduced tank.....	68
Figure 60: Proposed cross section of the ALFR (Dual asymmetric macro focal CEC Concentrator), notice the two CEC, each for its own evacuated tube and illuminated by an asymmetric primary, on the single tower.	71
Figure 61: Detail of the second stage showing the asymmetric CEC, the involute part and the V-groove addition, for zero gap losses.	71
Figure 62: Render view of the ALFR solar concentrator	73

Tables

Table 1: Concrete storage module specifications [2, 4, 5]	8
Table 2: Pilot-scale concrete storage module specifications [5]	16
Table 3: Isentropic efficiency values for the turbine stages	41
Table 4: Analyzed options	48
Table 5: Analyzed combinations	48
Table 6: Design parameter for the solar field including different HTF options.....	49
Table 7: Design parameters for the two-tank storage system with a 12 h capacity	49
Table 8: Design parameter of the power block system	49
Table 9: Relative cost for the solar field.....	51
Table 10: Relative storage cost overview for the three different HTF	51
Table 11: Power block cost overview for the three different HTFs	52
Table 12: Cost items and assumptions for the LCOE calculation.....	52
Table 13: Investment cost for the different collector technologies and HTF for a solar multiple of 1	53
Table 14: Plant configurations for which the lowest LCOE have been obtained.....	59
Table 15: Configurations with 12 h storage which have led to the lowest LCOE	60
Table 16: Utilization numbers of the storage system for the configurations.....	61
Table 17: Reference case.....	62
Table 18. Molten salts mixture at TESLAB	64
Table 19. Position of the nodes of the coil in the tank	64
Table 20. Performance of the tanks	69
Table 21: Comparison of ground area for Fresnel and PTC commercial solutions for the same mirror area.	70
Table 22: Geometric characteristics of the ALFR concentrator	72
Table 23: Optical performance of the concentrator	73
Table 24: Yearly results, energy and final conversion efficiency for ALFR (corresponding to 58MWe _p at 950 W/m ² DNI) concept plant collector with a total mirror area of 250 000m ² (no storage)	74

2. Introduction

Thermal energy storage (TES) is the big advantage of CSP. This work focuses on several aspects of TES, including transient response studies, the impact of several TES and collector solutions on the levelized cost of electricity (LCOE), as well as the influence of heat source location on the efficiency of a molten salt heat storage.

On the one hand, Section 3 discusses the modeling and transient simulation of a passive sensible heat storage system using high-temperature concrete as storage medium. In particular, its transient behavior will be compared to a conventional active indirect two-tank storage unit using molten salt as storage medium, being able to point out advantages and disadvantages over state-of-the-art technology regarding its transient behavior.

On the other hand, Section 4 treats the comparison of different system combinations comprising different collector technologies, solar field layouts, heat transfer fluids, heat storage media and storage technologies. It gives an overview of the state-of-the-art technology options for CSP collectors, solar field layout, heat transfer fluid, heat storage media and storage methods. In total, 9 different combinations are analyzed, out of which the case using parabolic trough collectors (north-south orientation), Therminol VP1 as HTF and two-tank molten salt TES is regarded as reference case.

Section 5 analyzes the influence of heat source location on the efficiency of small molten salts based storage for steam generation with direct immersed helical coil at steady-state.

Section 6 presents a linear Fresnel collector design with dual receiver configuration reaching higher area concentration factors than conventional Fresnel systems.

3. Transient response simulation of a passive sensible heat storage system and the comparison to a conventional active indirect two-tank unit (CENER)

3.1 Passive sensible heat storage and its modeling

Passive sensible heat storage has already been subject of prior publications. Several studies have already been published by the German Aerospace Center (DLR) [1-6], which treat numerical simulation [1, 5], the experimental testing [2, 5] as well as the theoretical integration in PTC plants [1] and the economic and life cycle assessment [6]. In this context, Jian et al. [7] also presented a specific modular charging and discharging operation strategy to improve the utilization of the storage capacity.

The typical layout of a passive sensible heat storage module is shown in Figure 1, consisting of a cuboid-shaped concrete block containing a tube bundle in staggered configuration. Through this tube bundle the HTF is flowing, either charging or

discharging the module. A complete heat storage system is supposed to consist of many such modules connected in series and in parallel, according to the desired thermal capacity. For 1100 MWh thermal, Laing et al. [4] proposed 252 modules, each having the specifications as indicated in Table 1. The dimensions of the basic storage module are limited due to manufacturing and transport. The complete storage system with housings, thermal insulations and pipework is expected to cover 300 x 100 square meters [2]. Such a 1100 MWh system would consist of 18 parallel rows of basic modules, having 14 modules connected in series in each row [2].

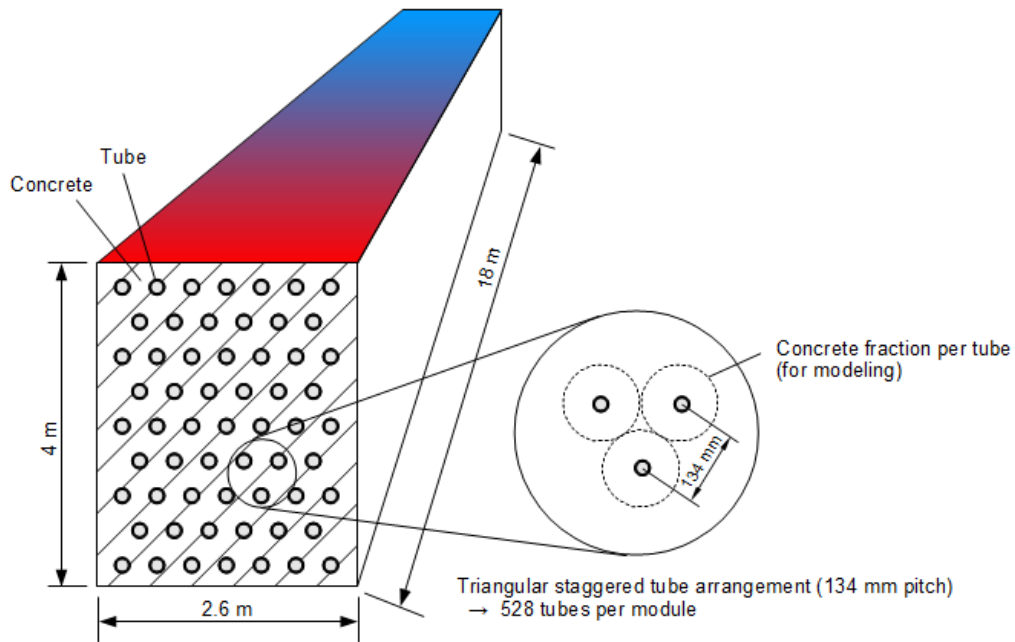


Figure 1: Concrete module layout with dimensions according to Refs. [2, 4, 5]

Table 1: Concrete storage module specifications [2, 4, 5]

Module parameter	Value/Specification
Module length (m)	18
Module height (m)	4
Module width (m)	2.6
Number of tubes per module (-)	528
Triangular tube pitch (mm)	134
Tube outer diameter (mm)	18
Tube inner diameter (mm)	15

Tube material	18Cr-8Ni stainless steel with thermo-physical properties according to Peet et al. [8]
Concrete type	N4-Concrete with thermo-physical properties according to Laing et al. [4]

When modeling the system, certain simplifications have to be made so that the simulation effort can be kept reasonably small. The typical key assumption is that all tubes behave in the same way, thus only one tube with its surrounding concrete volume has to be modeled. Figure 1 indicates the concrete volume fraction per tube as dashed circles in the detailed view. Hence, the modeling of the storage module is reduced to the simple problem of a steel tube embedded in a concentric cylinder of high-temperature concrete. Nevertheless, between the tube and the concrete, an additional contact resistance has to be modeled, since the steel tube and the surrounding concrete are not in direct contact with each other, in order to avoid mechanical stress due to different thermal expansion. Typically, this is solved by applying a very thin layer of graphite [5] between tubes and concrete, which however may also include air gaps. A good way to model this graphite/air layer is to assume an air gap of 0.2 mm thickness with a thermal conductivity of 0.0261 W/(m K) [5]. This has also been done in this work and has shown good agreement with experimental data.

According to the above, the model of the storage module consists of a tube with a concentric thin layer of air and a concentric cylinder of concrete. In the following, the 1-D model setup used in this work will be presented in detail. As in previous works [1, 5], Modelica [9] has been used as modeling language. Modelica is a multi-purpose physical system modeling language and has been developed in an international effort in order to unify already existing similar modeling approaches and to enable developed models and model libraries to be easily exchanged. The concept is based on non-causal models featuring true ordinary differential and algebraic equations, i.e. differential-algebraic equation (DAE) systems [9].

The 1-D HTF flow inside the steel tube is modeled using the finite volume method (FVM) according to the Modelica Standard Library (MSL) [10] extending from the base model class “partial distributed volume”, which defines the mass and energy balances in terms of net mass flow, net enthalpy flow, net heat flow \dot{Q}_{net} and net work flow \dot{W}_{net} , for each control volume i (see Figure 2). This can be written as follows:

$$m_i = V_i \cdot \rho_i \quad (1)$$

$$\frac{dm_i}{dt} = \dot{m}_{a, i} - \dot{m}_{b, i} \quad (2)$$

$$U_i = m_i \cdot u_i \quad (3)$$

$$\frac{dU_i}{dt} = \dot{m}_{a, i} \cdot h_{a, i} - \dot{m}_{b, i} \cdot h_{b, i} + \dot{Q}_{net, i} + \dot{W}_{net, i} \quad (4)$$

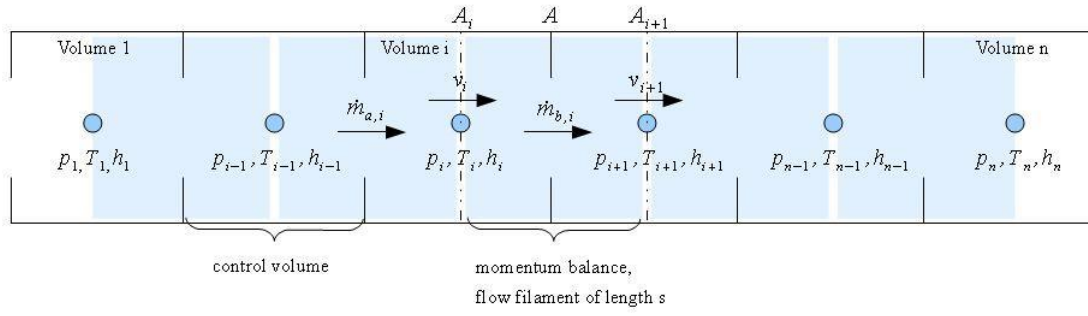


Figure 2: Finite volume discretization scheme according to the staggered grid approach [11]

Of course, in this case, the net work flows $\dot{W}_{net, i}$ are set to zero as there is no work flow involved in the process. The HTF fluid properties have been implemented according to Ref. [12].

This 1-D HTF flow model is then coupled to 1-D cylindrical radial conduction models, representing (i) the steel tube, (ii) the air gap and (iii) the concrete volume (see Figure 3). The heat flow is only modeled in radial direction normal to HTF flow direction, neglecting axial conduction in the storage module. This is definitely a simplification, since axial conduction is present. However, it is not dominant due to the relatively small axial temperature gradient.

According to Figure 3, each fluid control volume is coupled with a set of 1-D cylindrical radial conduction models, differing only in the number of radial temperature nodes and the thermo-physical properties. Grid independent solutions have been obtained for 1 conduction node for the tube and the air gap, respectively, and 25 conduction nodes for the concrete volume (in Figure 3 only 4 of the 25 nodes are shown). Figure 4 shows the conduction model details for one single discrete longitudinal section i for the case of the steel tube, having one temperature node in radial direction. The corresponding thermal capacitance $C_{tube i}$ of each pipe segment is assumed to be lumped in this single temperature node (see Figure 3, $T_{tube 1}$ to $T_{tube n}$). This 1-D conduction model is based on the so-called “single layer cylinder” model of the free Modelica Buildings Library [13], which has been adapted to allow for an easier definition of 1-D conduction model arrays. The governing equations for each discrete longitudinal section i can be described as follows:

$$R_1 = \frac{\ln(r_{center}/r_{inner})}{2 \cdot \pi \cdot L_i \cdot k_{tube}} \quad (5)$$

$$R_2 = \frac{\ln(r_{outer}/r_{center})}{2 \cdot \pi \cdot L_i \cdot k_{tube}} \quad (6)$$

$$\dot{Q}_1 = \frac{T_{tube inner i} - T_{tube i}}{R_1} \quad (7)$$

$$\dot{Q}_2 = \frac{T_{tube i} - T_{tube outer i}}{R_2} \quad (8)$$

$$C_{tube\ i} \cdot \frac{dT_{tube\ i}}{dt} = \dot{Q}_1 - \dot{Q}_2 \quad (9)$$

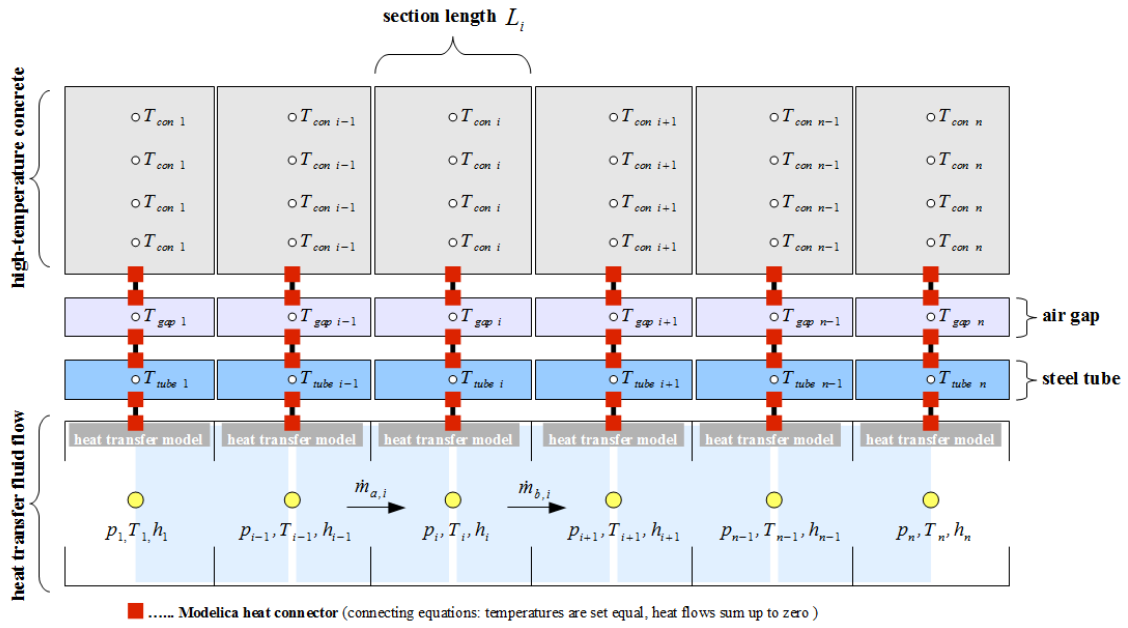


Figure 3: Modelica concrete TES model scheme

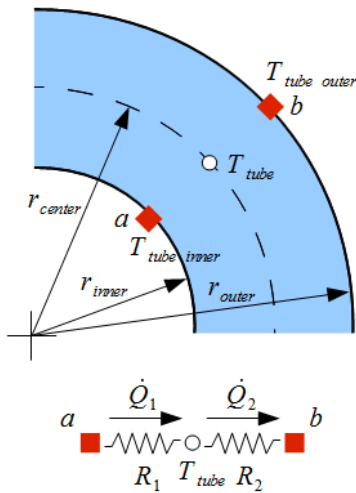


Figure 4: Cylindrical conduction model scheme (example for steel tube)

In order to complete the model, the forced convective coupling between the HTF fluid flow and the steel tube inner wall has to be stated. According to the MSL, this is done by using a replaceable wall heat transfer model (see “heat transfer model” in Figure 3), which defines the relationship between the tube’s inner wall temperatures, the fluid bulk temperatures (see Figure 3, T_i to T_n) and the heat flows $\dot{Q}_{net\ i}$. Thus, the default tube model can easily be adapted for different flow conditions, by simply exchanging the

heat transfer sub-model, which basically means that the heat transfer coefficient is estimated by using different Nusselt number correlations, fulfilling Newton's convective heat transfer law:

$$\dot{Q}_{net\ i} = h_{fluid\ i} \cdot A_{tube\ i} \cdot (T_{tube\ inner\ i} - T_i) \quad (10)$$

The default setting in the model is the widely accepted Gnielinski correlation [14]. Nevertheless, in Section 3.1.1 a specific correlation for Therminol VP1 [12] will be presented.

Next, the model has to be brought from tube level to system level, where the total number of tubes goes up to several thousands. In the specific above discussed case of 1100 MWh thermal capacity, the total number of tubes would be 9504 (18 parallel rows of basic modules of 528 tubes each). Basically, there are two possible options: (a) modeling the storage system just by one tube element as shown in Figure 3 and reducing the entering HTF mass flow to the corresponding fraction (total HTF mass flow divided by 9504), or, (b) introducing a representative system-level model by defining the equivalent thermal capacitance, the equivalent thermal resistance as well as the equivalent HTF volume. Option (b), which is applied in this work, can easily be achieved by a slight modification of the model explained above. It is required to multiply each control volume size V_i and each conduction model section length L_i (see Figure 3), and each area of heat transfer ($A_{tube\ i}$ of the distributed wall heat transfer models) by the number of total tubes. Note: The radial dimensions for the tube, the gap and the concrete stay the same, i.e. the real dimensions for one tube element. Obviously, this also implies that the hydraulic diameter stays the same, and for flow velocity calculation (Reynolds number calculation) the total mass flow has to be divided by the total number of tubes.

The big advantage of option (b) is that the control volume size and the thermal capacitance of the radial conduction nodes keep sufficiently big to avoid a stiff system of equations for larger system-level plant models. One may speak about a stiff system of equations when there are greatly differing time constants within the modeled system [15]. For instance, small control volumes react very fast to changes in net heat flow or net enthalpy flow, hence they approach very fast their new steady state and have thus relatively small time constants when compared to large fluid volumes whose temperature changes slowly due to the difference in mass. Generally, the term time constant is used by engineers and physicists to refer to the rate of decay of state variables [15]. The differences between the rates of decay of the state variables of the system have a strong influence on the stability of the numerical method applied. Typically, the fastest rates of decay control the stability of the numerical method used to solve the system of equations [15].

Last but not least, thermal losses are neglected for the present transient response study. Thus the heat storage system is considered as adiabatic. Nevertheless, for model

validation (Section 3.1.2) the following empirical heat loss correlation has been applied, which is valid for a pilot-scale (8.37 x 1.3 x 1.7 m) concrete storage module [5]:

$$\dot{Q}_{loss} = 9.35 \cdot (T_{average} - T_{ambient})^{1.201} \quad (11)$$

In the following numerical studies, the developed Modelica code has been translated into numerical simulation code using a state-of-the-art commercial Modelica tool, applying its differential-algebraic system solver DASSL [16, 17]. This algorithm applies an implicit method for the numerical integration of the governing ordinary differential equations. In particular, it approximates the derivatives using a k^{th} order backward differentiation formula, where k ranges from 1 to 5. At every step it chooses the order and the step size based on the behavior of the solution. Newton's method is used to solve the resulting equations for the solutions at each discrete point in time [16, 17].

3.1.1 Development of a specific heat transfer correlation for Therminol VP1

Typically, when modeling forced convective heat transfer in tubes, Nusselt number correlations are taken from literature in order to calculate the convective heat transfer coefficient. A very popular and often reconfirmed correlation is the one proposed by Gnielinski [14] in the year 1975. However, for some applications with special heat transfer fluids and operation in the transition region between laminar and turbulent flow, large errors may be introduced by using the original Gnielinski correlation. This is the case when using Therminol VP1 [12] with typical flow parameters for passive sensible heat storage modules as discussed above. Figure 5 compares the Gnielinski correlation (gray) with data points obtained from CFD simulations in ANSYS Fluent (green dots) [18]. As can be seen in the graphic, at Reynolds numbers close to $3 \cdot 10^4$, the Gnielinski correlation agrees well with the simulated data. However, at lower and upper values, significant deviations are observed.

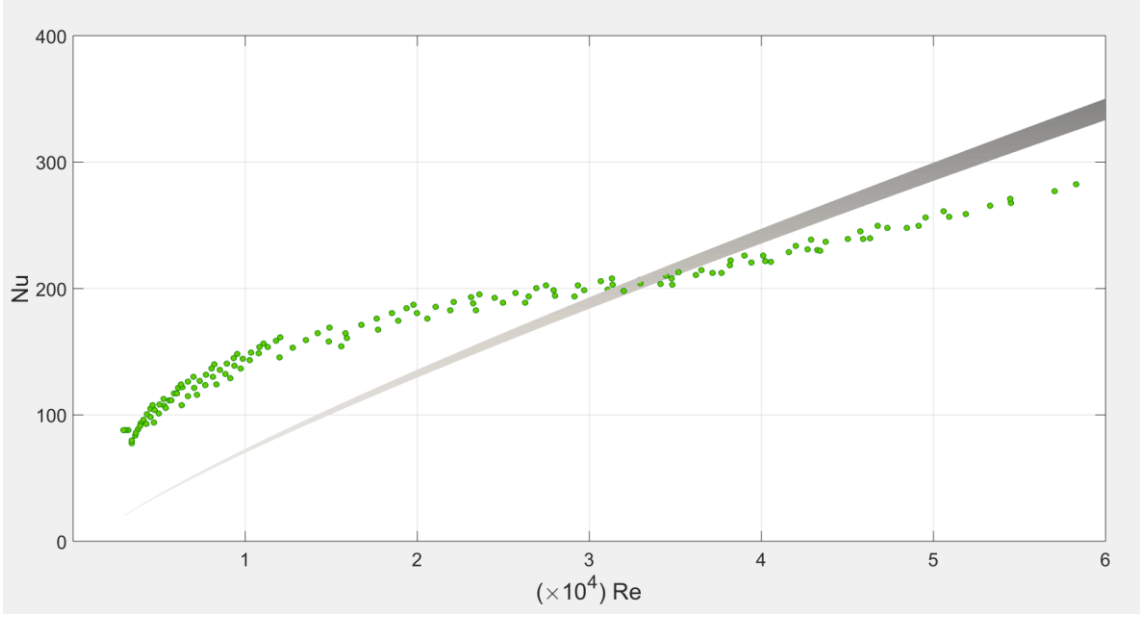


Figure 5: Gnielinski correlation (gray) vs. simulated data points in ANSYS Fluent (green dots)

For this reason, a specific correlation has been developed for Therminol VP1 and typical flow parameters ($3000 < Re < 60000$, $5 < Pr < 5.6$) as observed in passive sensible heat storage modules for PTC plants. This new correlation, Eq. (16), is based on the Gnielinski correlation introducing two parameters a and b , for the turbulent region (Eq. (15)) and for the transition region (Eq. (14)), respectively. These two parameters have been chosen such for each region that we obtain together with a transition function s a good agreement with the numerical data points from ANSYS Fluent [18].

$$Nu = \frac{a \cdot \frac{f}{8} \cdot (Re + b) \cdot Pr}{1 + 12.7 \cdot \left(\frac{f}{8}\right)^{\frac{1}{2}} (Pr^{\frac{2}{3}} - 1)} \quad (12)$$

$$f = (0.79 \cdot \ln(Re) - 1.64)^{-2} \quad (13)$$

$$Nu_{transition} = \frac{1.15 \cdot \frac{f}{8} \cdot (Re + 2500) \cdot Pr}{1 + 12.7 \cdot \left(\frac{f}{8}\right)^{\frac{1}{2}} (Pr^{\frac{2}{3}} - 1)} \quad (14)$$

$$Nu_{turbulent} = \frac{0.58 \cdot \frac{f}{8} \cdot (Re + 19500) \cdot Pr}{1 + 12.7 \cdot \left(\frac{f}{8}\right)^{\frac{1}{2}} (Pr^{\frac{2}{3}} - 1)} \quad (15)$$

$$Nu = s \cdot Nu_{turbulent} + (1 - s) \cdot Nu_{transition} \quad (16)$$

The transition function s returns the value 1 for Reynolds numbers larger than 10000. Between Reynolds numbers 2300 and 10000 it smoothly varies between 0 and 1 to allow for a numerical sound transition. The so-called “Stepsmoother” function [19] from the Modelica Standard Library [10] is used. Figure 6 shows the comparison of the new correlation (Eq. (16)) with the simulation results of ANSYS Fluent. The maximum relative error between CFD simulation results and the new correlation is reduced to 15% [18]. It must be noted that this new correlation is only valid for the specific fluid and the operating temperature ranges observed in a passive sensible TES for parabolic trough collector plants.

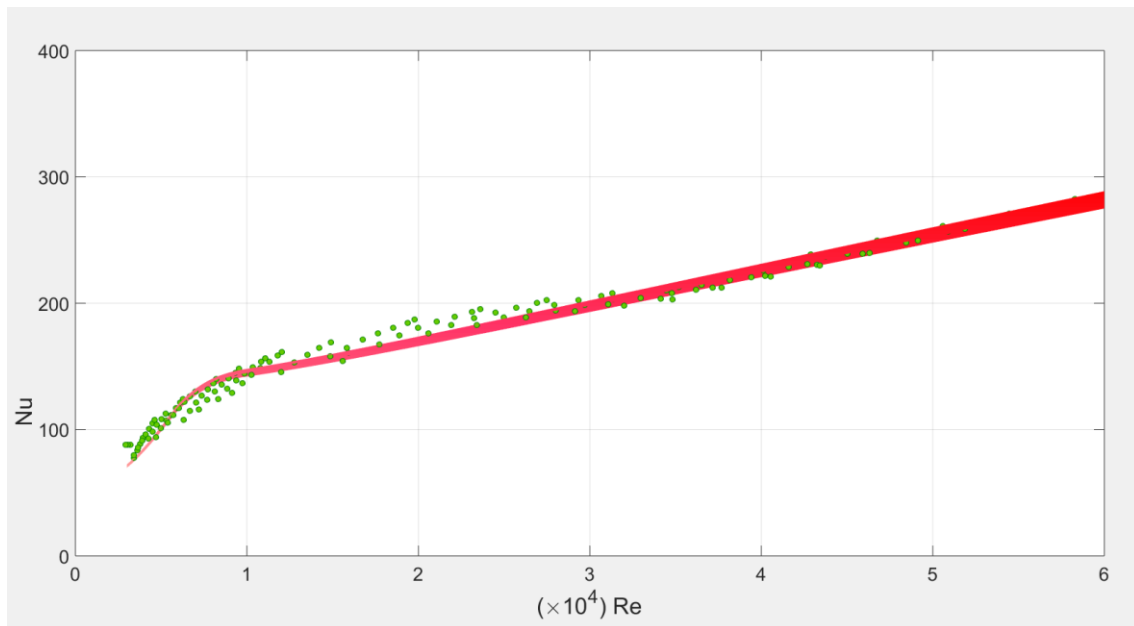


Figure 6: The proposed correlation (Eq. (16) - red) vs. simulated data points in ANSYS Fluent (green dots) [18]

3.1.2 Model validation against experimental data

The concrete storage model explained above has been validated against experimental data obtained from the work of Stückle [5]. He described a pilot-scale concrete storage module having the specifications as given in Table 2.

Table 2: Pilot-scale concrete storage module specifications [5]

Module parameter	Value/Specification
Module length (m)	8.37
Module height (m)	1.3
Module width (m)	1.7
Number of tubes (-)	132
Triangular tube pitch (mm)	134
Tube outer diameter (mm)	18
Tube inner diameter (mm)	15
Tube material	Steel
Concrete type	N4-Concrete with thermo-physical properties according to Laing et al. [4]
HTF system pressure (bar)	12
HTF type	Syltherm 800 [20]
HTF nominal volume flow for 8 h charging/ discharging (m ³ /h)	20
Temperature measurement sensor at inlet and outlet	Pt 100 resistance temperature sensor
Temperature measurement uncertainty (K)	±1.5

For model validation purpose, fluid properties have been implemented according to Ref. [20], as Syltherm 800 is applied in the experimental installation. The default Nusselt number correlation according to Gnielinski [14] is applied, since fluid properties differ from Therminol VP1. Grid independence has been reached with 15 nodes (CVs) in axial direction along HTF flow, and 25 nodes in radial direction in the concrete conduction model. This corresponds with the information given in Ref. [5].

Figure 7 shows an 8 hours charging experiment where the measured module inlet temperature is plotted as solid black line. The measured module outlet temperature is plotted as solid red line. To validate the model, the measured inlet temperature has been taken as boundary condition, together with the given volume flow constraint of 20 m³/h. The simulated module outlet temperature is then compared with the measured

experimental value (see black dashed line in Figure 7). As can be seen, the simulation agrees very well with the experiment. The deviation stays within the temperature measurement uncertainty.

The following figures (Figure 8 to Figure 10) show key simulation data which should serve for future model comparison. Figure 8 displays the module mass flow rate. Figure 9 shows the HTF flow Reynolds number of the first control volume (black solid) and the last control volume (black dashed). Figure 10 gives the forced convective heat transfer coefficient according to Gnielinski [14] also for the first CV (black solid) and the last CV (black dashed).

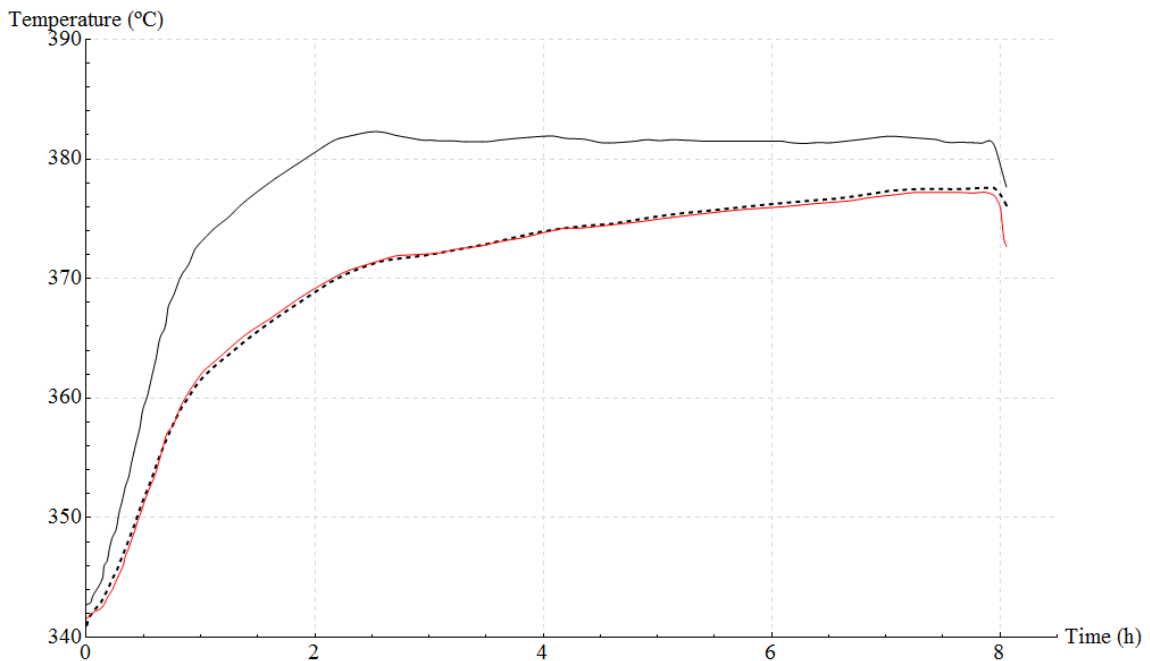


Figure 7: Storage module inlet and outlet temperature – measured inlet temperature (black solid), measured outlet temperature (red solid), simulated outlet temperature (black dashed)

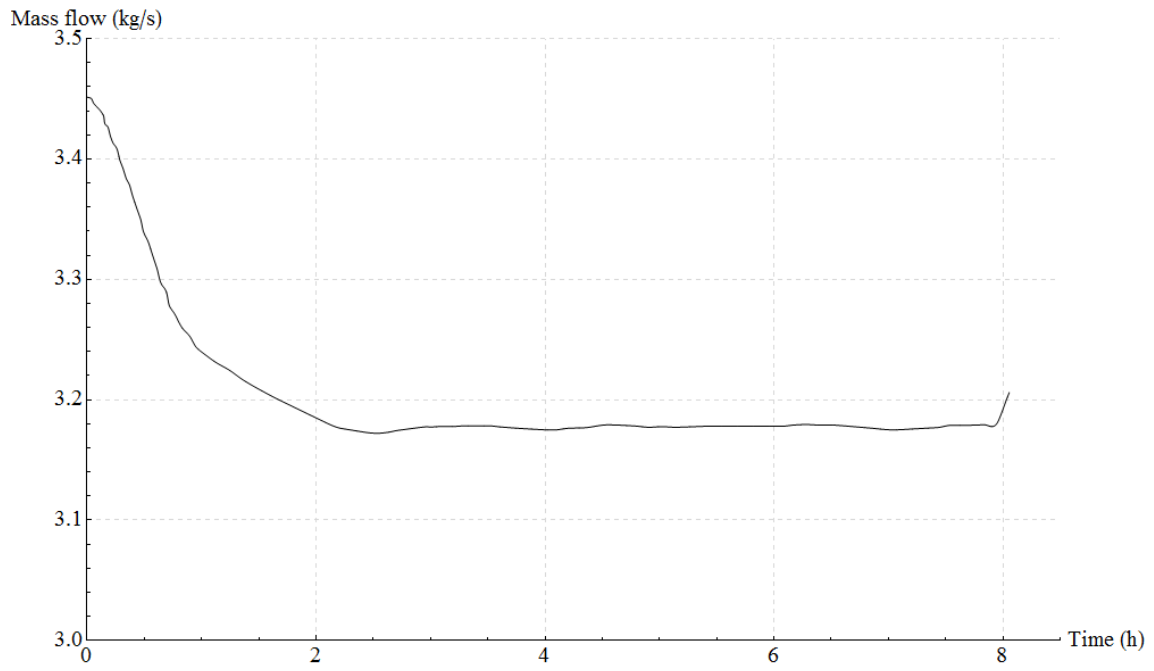


Figure 8: Storage module mass flow rate

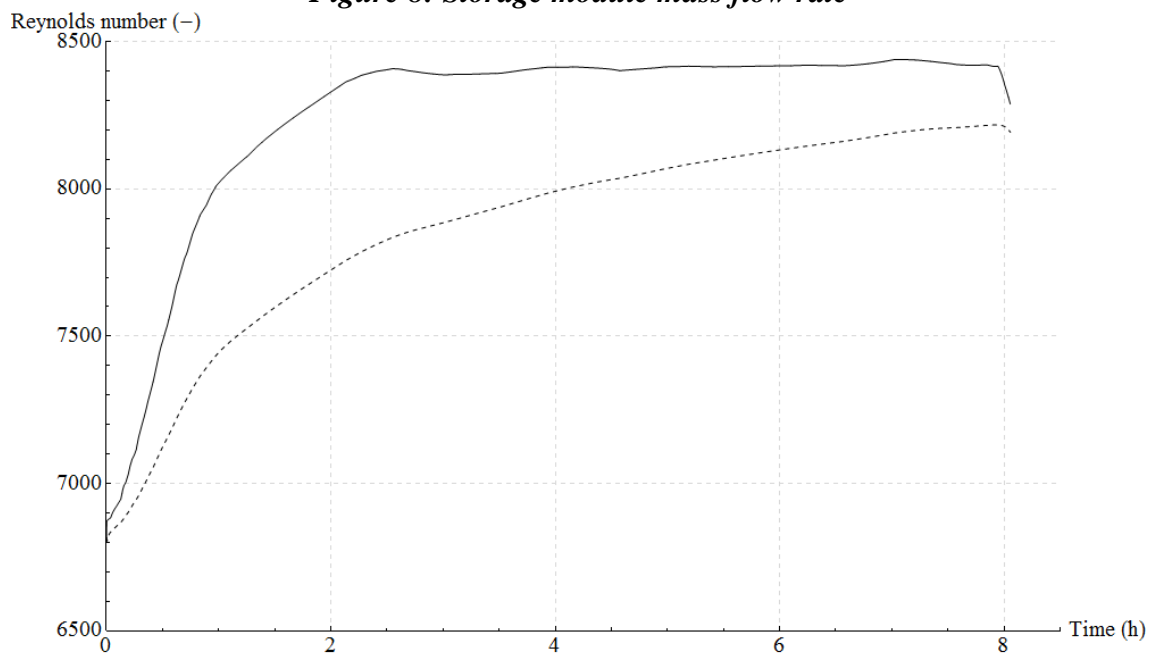


Figure 9: Reynolds number of fluid flow in tubes – first control volume (black solid), last control volume (black dashed)

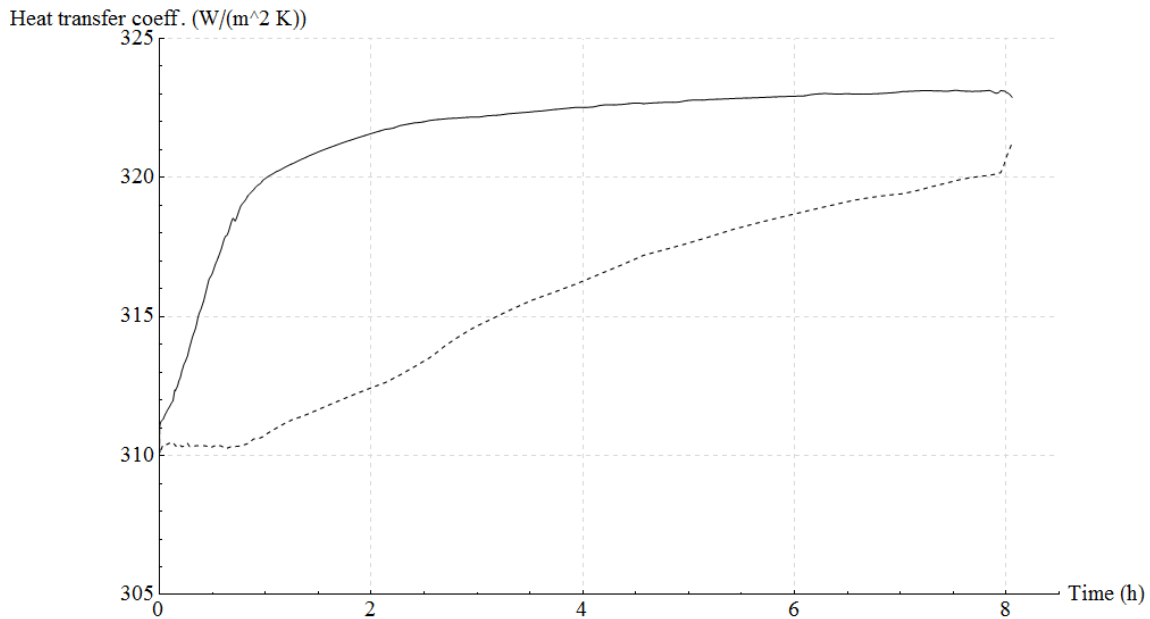


Figure 10: Forced convective heat transfer coefficient between fluid and tubes inner wall – first control volume (black solid), last control volume (black dashed)

3.1.3 Up-scaling and typical simulation results

As a next step, this section will deal with the model up-scaling and typical transient simulation results. In particular, it is important to guarantee grid independence for a commercial-sized concrete TES system having 1100 MWh of thermal capacity. Such a system is assumed to consist of 18 parallel rows of basic modules (according to Table 1), having 14 modules connected in series in each row [2]. Another important point is to obtain the cyclic steady state of the system before starting the transient response comparison with a conventional two-tank TES system.

Obtaining grid independence

In order to obtain grid independence of the above mentioned concrete TES system, two simulation types will be done, applying (A) ideal step changes in mass flow rate at constant inlet temperature of 391 °C, and (B) an ideal inlet temperature step change at constant mass flow rate of 600 kg/s. Figure 11 and Figure 12 display simulation type A. Figure 11 gives the ideal mass flow boundary condition for an 8 hours experiment. It starts with a completely empty storage system (initialized at ≈ 285 °C) at the nominal charging flow rate of 600 kg/s and changes after a simulation time of 3 hours abruptly to -600 kg/s, which is nominal discharging rate. Again, after 3 hours the system switches over to nominal charging until the end of the simulation. Figure 12 displays the corresponding temperature of the last control volume at the outlet (cold end) for different numbers of nodes, i.e. control volumes (CVs), in axial direction (in direction of HTF flow). As can be seen, grid independence is approximately reached at 320 CVs. The difference in simulation result between 160 CVs and 320 CVs is negligible small.

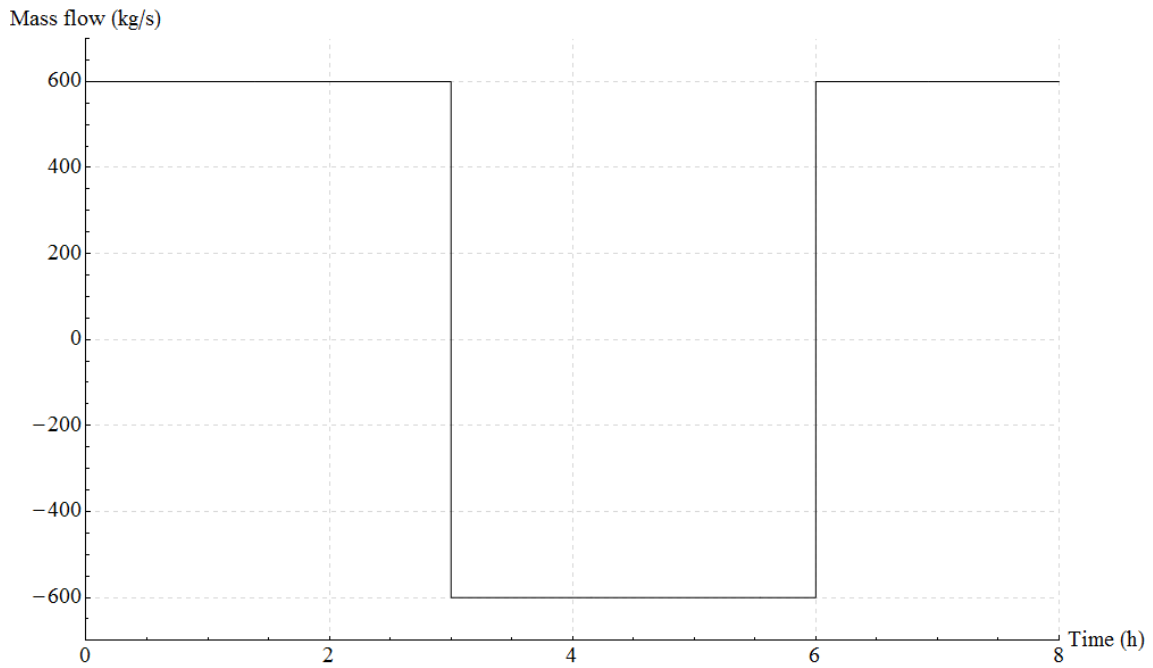


Figure 11: Module mass flow rate of grid independence test A (at constant inlet temperature of 391 °C)

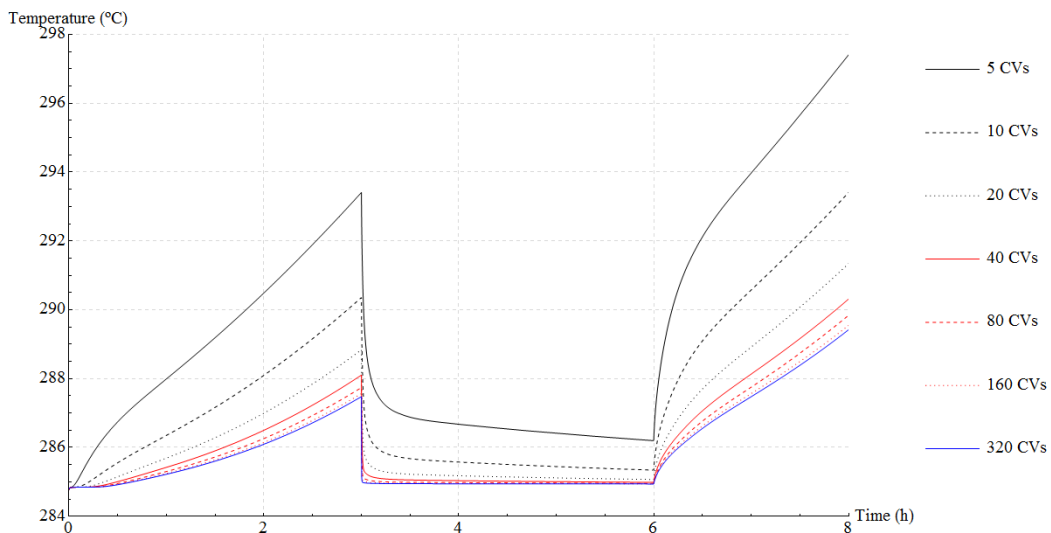


Figure 12: Module cold end temperatures of grid independence test A

Simulation type (B) is shown in Figure 13 and Figure 14. Figure 13 displays the idealized HTF inlet temperature at a constant mass flow rate of 600 kg/s (charging mode). Again, the simulations start at a completely empty storage system (initialized at ≈ 285 °C) having an inlet temperature of 341 °C. After 4 hours, the inlet temperature abruptly changes to 391 °C. Figure 14 shows the storage system outlet temperature (temperature of the last control volume at the cold end) for different numbers of nodes, i.e. control volumes (CVs), in axial direction (in direction of HTF flow). Again, it can

be observed that the simulation results converge at around 320 CVs. The difference between 160 and 320 CVs is negligible small. For the following transient simulations, 300 CVs have been chosen. However, for larger system-level models including all power plant components, the number of CVs may be reduced to 160.

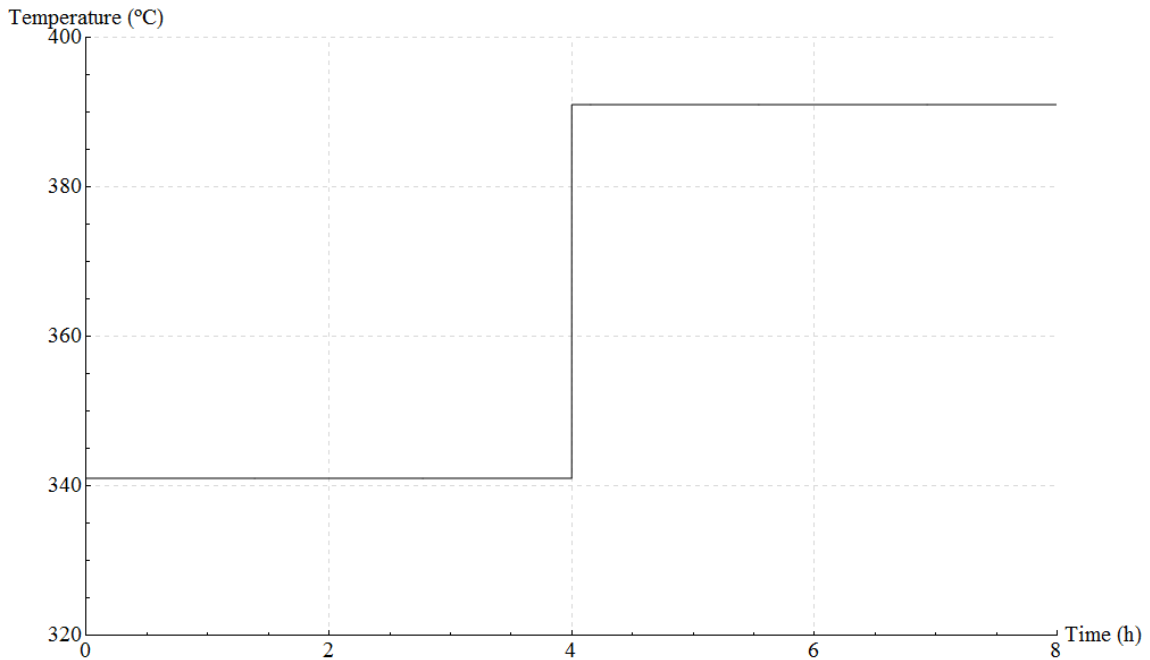


Figure 13: Module inlet temperature of grid independence test B (at constant mass flow rate of 600 kg/s)

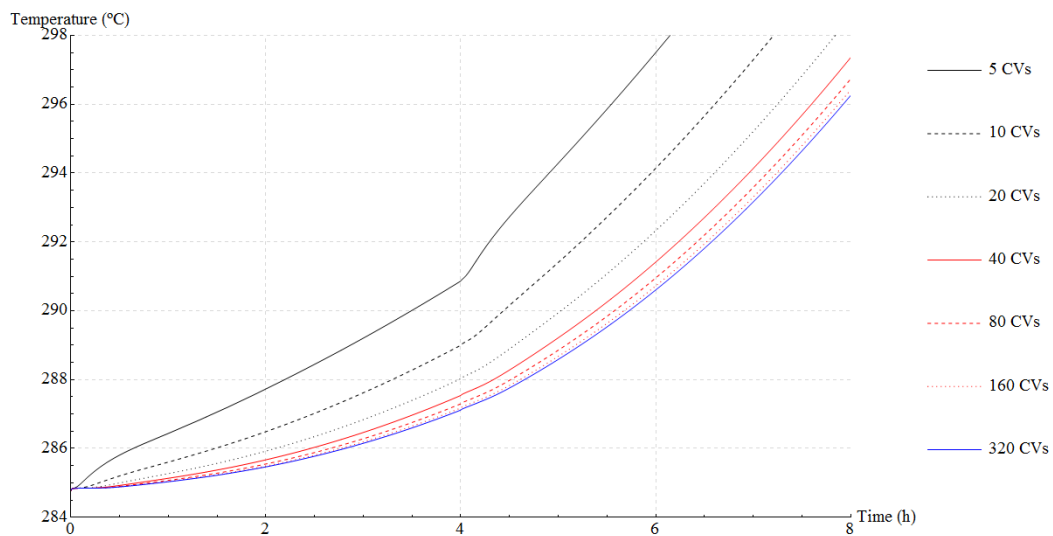


Figure 14: Module outlet temperatures of grid independence test B

Reaching cyclic steady-state

As known from packed-bed thermocline TES, the thermocline needs to be established during the first cyclic operation of the system. Also the concrete TES system is to be expected to behave similarly, although no clear thermocline zone is observed. Tamme et al. [1] showed that the temperature distribution over the concrete storage system length is clearly different from that of packed-bed thermocline storage systems, where the temperature profile can be distinguished into three zones, (i) a rather constant low temperature zone, (ii) a pronounced temperature gradient zone (the thermocline zone), and (iii) a rather constant high temperature zone [21]. On the contrary, the concrete TES system shows an almost linear temperature profile from the high-temperature to the low-temperature end, which however develops towards a “thermocline” shape for increasing TES system length and lower mass flow rates.

In summary, before starting with the transient performance comparison, the concrete TES system model has to reach its cyclic steady state, which needs to be later on imported as initial condition when doing the transient response comparison. In order to do so, the concrete TES system model will be simulated in a cyclic way, providing typical boundary conditions (a HTF solar field outlet temperature of 391 °C and a HTF steam generator return temperature of 285 °C) and cut-off temperature constraints. According to Tamme et al. [1], the cut-off temperature constraints are 315 °C for charging and 350 °C for discharging. This means that the charging process is terminated when the temperature at the cold end (storage outlet to solar field inlet) rises to 315 °C, and the discharging process is terminated when the temperature at the hot end (storage outlet to steam generator inlet) falls to 350 °C. These constraints are established so that the solar field inlet temperature is not too high, and the steam generator inlet temperature is above minimum [1].

Figure 15 displays the hot end temperature (first control volume: red solid) and the cold end temperature (last control volume: blue solid) of the periodic simulation. The simulation starts with a completely empty storage system initialized at 285 °C and nominal charging rate of 600 kg/s HTF mass flow. When the cold end temperature reaches the cut-off temperature of 315 °C, the HTF mass flow is inverted to nominal load discharging (-600 kg/s) applying a Modelica “when” statement [22] in the model code. Accordingly, when the hot end temperature falls to 350 °C, the HTF mass flow is switched again to nominal load charging. The solar field outlet temperature and the steam generator return temperature is assumed to be constant at 391 °C and 285 °C, respectively. It has to be noted that this is an idealized assumption, especially for the steam generator, as the outlet temperature changes according to its thermal characteristic when the inlet temperature changes. However, these boundary conditions should be sufficient for the purpose of this study.

Figure 16 displays the corresponding temperature evolution of the central fluid control volume (CV 150). It can be well observed that the system approaches its cyclic steady

state approximately between 1.5 and 2 days of simulation time after about 4 complete cycles. Figure 17 displays the alternating HTF mass flow rate.

Figure 18 displays the longitudinal temperature profile at switching from discharging to charging after the cyclic steady state has been reached. It can be well observed how the hot HTF enters and the charging temperature profile establishes. As already commented above, no thermocline zone is achieved, as could be expected thinking of packaged-bed single-tank TES systems [23]. This is clearly a major disadvantage of the tubular layout.

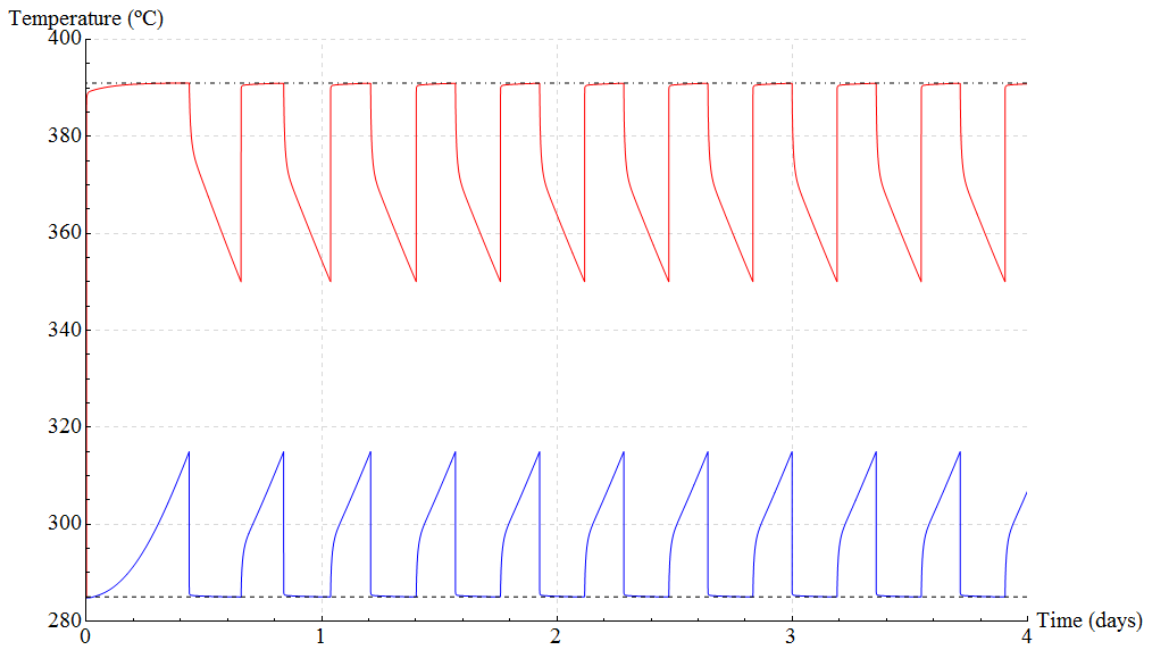


Figure 15: Hot (red) and cold (blue) end temperature of periodic simulation to reach periodic steady state – dot-dashed line: solar field outlet temperature – dashed line: steam generator return temperature

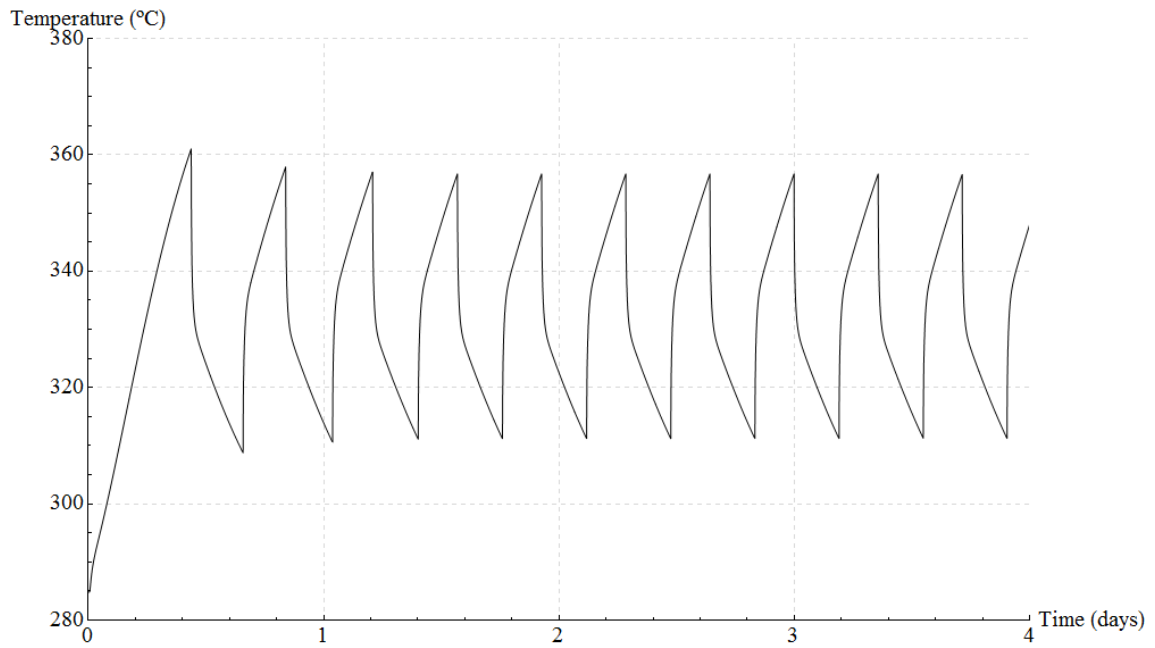


Figure 16: Center fluid (CV 150) temperature evolution during periodic simulation

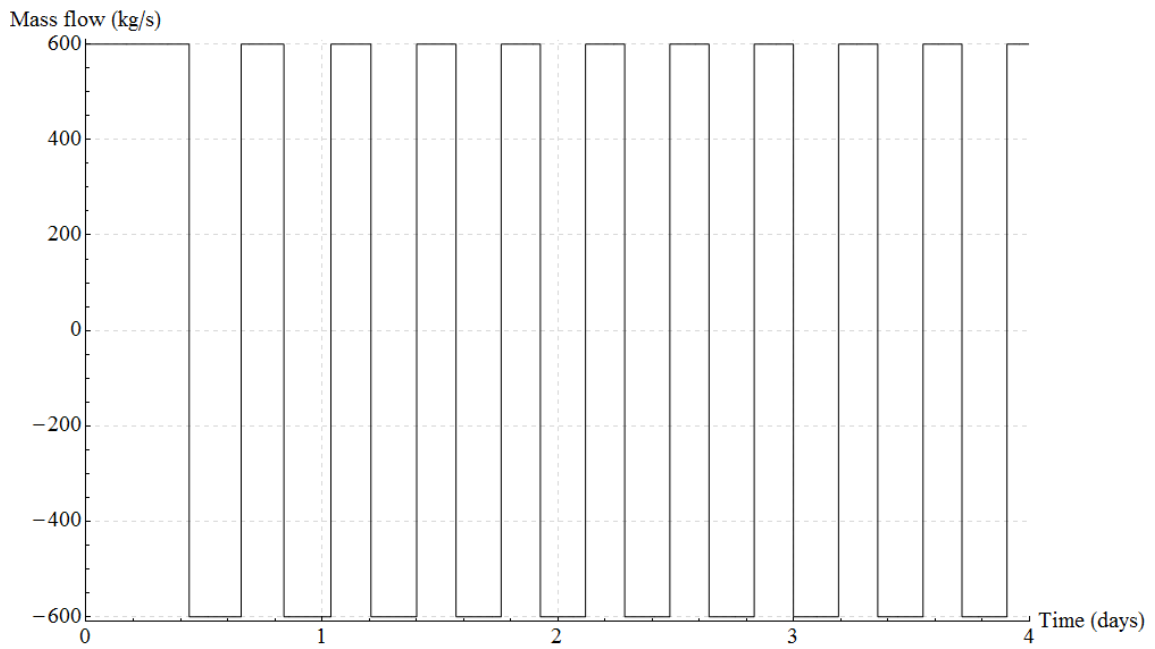


Figure 17: Periodic mass flow rate through concrete TES system according to cut-off temperature conditions

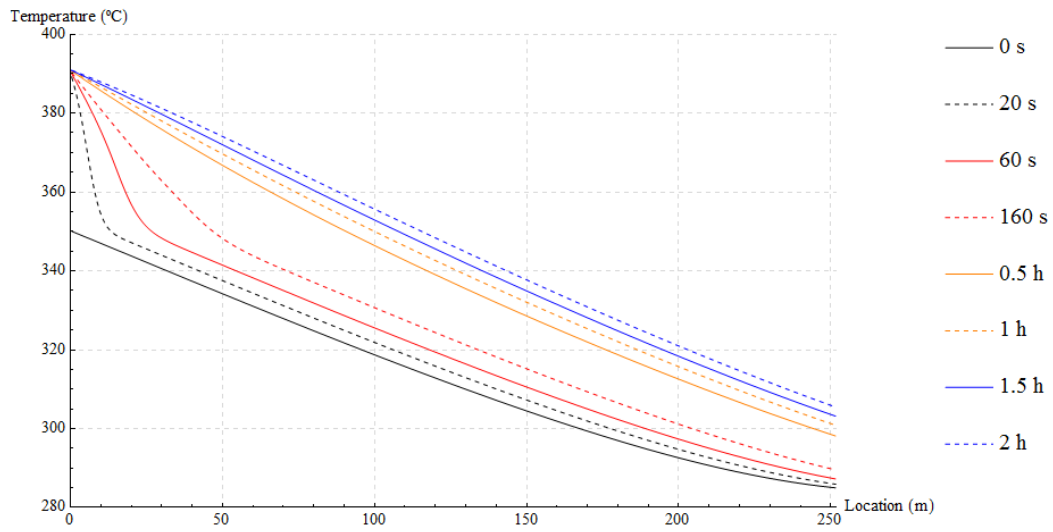


Figure 18: Longitudinal temperature profile evolution, starting at switching time ($t = 0$ s) from discharging to charging

3.2 Modeling of the conventional active indirect two-tank heat storage

This section briefly presents the model of the conventional active indirect two-tank TES using molten salt as storage medium. The model is explained in detail in previous publications [24-26] and the interested reader is referred to them for all model specifications.

Figure 19 shows the general setup of an active indirect two-tank thermal energy storage system for CSP. The basic components are the molten salt storage tanks (the hot tank at 386 °C and the cold tank at 292 °C) and the oil-to-molten-salt heat exchanger train, which typically consists of 3 shell-and-tube subunits connected in series [27]. Each shell-and-tube subunit is considered to have two shell passes with a longitudinal baffle and two tube passes in U-tube design, which corresponds to a TEMA-F [28] type design. For detailed heat exchanger specifications, it is referred to Table 1 of Ref. [26]. Note, that the molten salt suction pumps as well as the distribution headers are not displayed in the storage tank schemes.

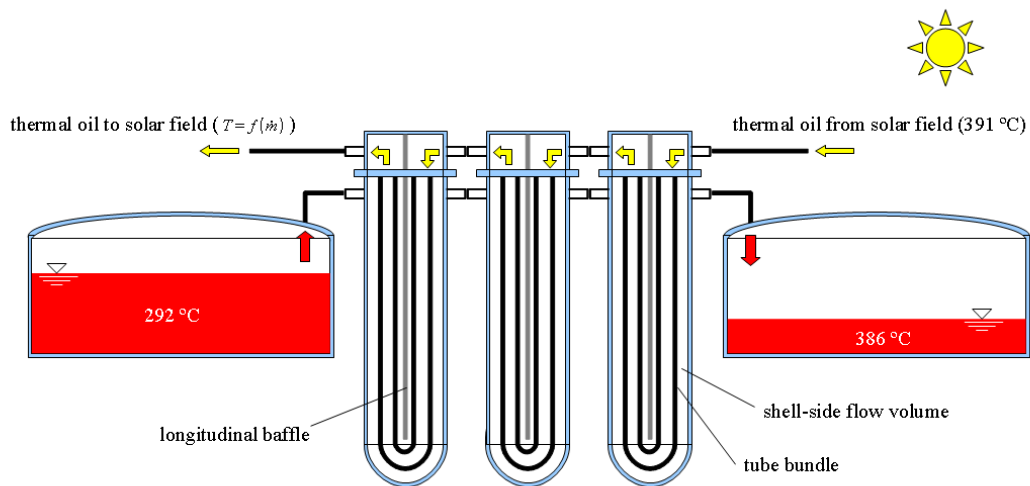


Figure 19: Conventional active indirect two-tank TES system layout [25]

When thinking of the transient response of such a system, the oil-to-molten-salt heat exchanger train forms a key component that has to be modeled in sufficient detail. According to a previous work [26], it turns out that it is sufficiently accurate to consider a simple counter-flow model setup as shown in Figure 20, having 80 CVs for each fluid stream (60 m total heat exchanger train length).

The HTF mass flow rate is a given boundary condition of the model. The same holds for the HTF inlet temperatures. As already stated above for the concrete TES system, they are set to the constant values of 391 °C, for charging (solar field HTF outlet temperature), and 285 °C, for discharging (power block HTF return temperature). The

molten salt mass flow rate is controlled in such a way that either the molten salt outlet temperature (charging), or the HTF outlet temperature (discharging) keeps to the assigned set-point.

In particular, during storage system charging mode, the molten salt outlet temperature is kept to the hot tank's design temperature (386 °C). On the other hand, during storage system discharging mode, the HTF outlet temperature is kept to the desired feed temperature of the CSP plant's steam generator (in this work 376 °C). In this way, the feed temperature of the cold molten salt tank varies according to the thermal characteristic of the heat exchanger train, i.e. it is not controlled to keep to the cold tank's design temperature of 292 °C.

Continuous PI controllers are applied for both the charging, and the discharging mass flow control. The inertia of the control system's actuator circuit (including the molten salt pumps) is modeled via an instance of a first-order block having a gain of 1 and a time constant of 30 s, i.e. 63.2% of the final molten salt mass flow rate value is reached after 30 s assuming a step-change in the control signal.

Since the HTF inlet temperatures are assumed to be constant while charging and discharging, the HTF mass flow rate variation is the only major disturbance caused. This also includes changes in flow direction when switching from charging to discharging mode, or vice versa.

The controller settings have been obtained via a so-called process reaction curve method, which can be applied to self-regulating processes that feature first-order-plus-time-delay behavior, i.e. that can be described by the three parameters as process gain K_s , dead time θ and time constant τ , as it is the case for the here considered heat exchanger in the range close to a certain operating point. In particular, the controller settings have been obtained applying the Chien-Hrones-Reswick method [29]. Evaluating open-loop step response simulations and applying the tangent method at the point of inflection [30], yields approximately 0.031 K s kg⁻¹ for the process gain K_s , 12.3 s for the dead time θ and 345.6 s for the time constant τ for charging mode, and 0.056 K s kg⁻¹ for the process gain K_s , 12.6 s for the dead time θ and 251.6 s for the time constant τ for discharging mode. This gives a controller gain K_p of 317.1 kg s⁻¹ K⁻¹ for the charge controller, and a controller gain K_p of 124 kg s⁻¹ K⁻¹ for the discharge controller. The integral time τ_i results in 414.7 s for the charge controller, and in 302 s for the discharge controller. It has to be noted that the controller output in the model is a direct mass flow signal and not a valve position or molten salt pump speed as it is the case in reality. Furthermore, the controller settings, stated above, have been obtained for flow conditions that are close to the nominal ones. However, due to non-linearities of the behavior of the heat exchanger train, its process parameters, on which the controller settings are based, typically vary depending on the actual load (HTF mass flow rate) and may not be ideal for the operation at partial loads.

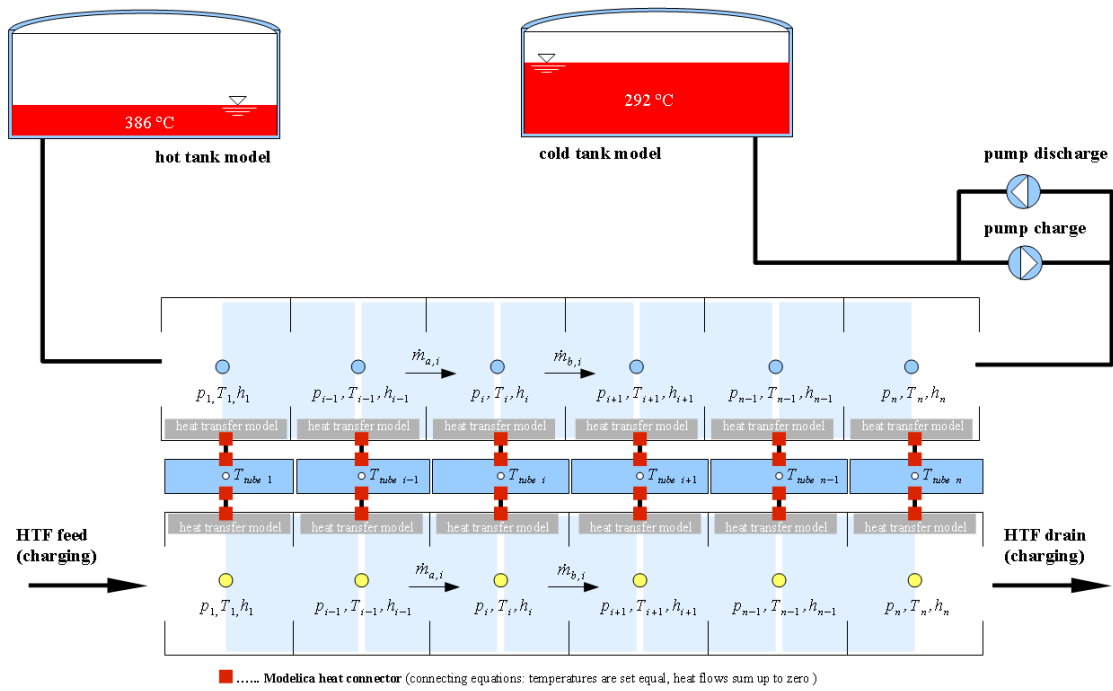


Figure 20: Conventional active indirect two-tank TES system model scheme in Modelica [24]

3.3 Comparison of the transient response of both heat storage systems for idealized changes in load

Now, having explained both models in detail, they will be used for a transient response comparison using the same idealized HTF mass flow boundary as shown in Figure 21. The simulation starts at nominal load charging (600 kg/s). After 2 hours charging at full load, the HTF mass flow is reduced to 80% (480 kg/s) nominal load. 1 hour later it is further reduced to 60% nominal (360 kg/s), then to 20% nominal load charging (120 kg/s), which remains until simulation time 5 hours. At this moment, the system is abruptly switched over to full load discharging (-600 kg/s) for one hour. At simulation time 6 hours, the system is switched again to full load charging (600 kg/s). Finally, at simulation time 7 hours, the system is switched over to full load discharging (-600 kg/s) where it remains until the end of the 8 hours simulation.

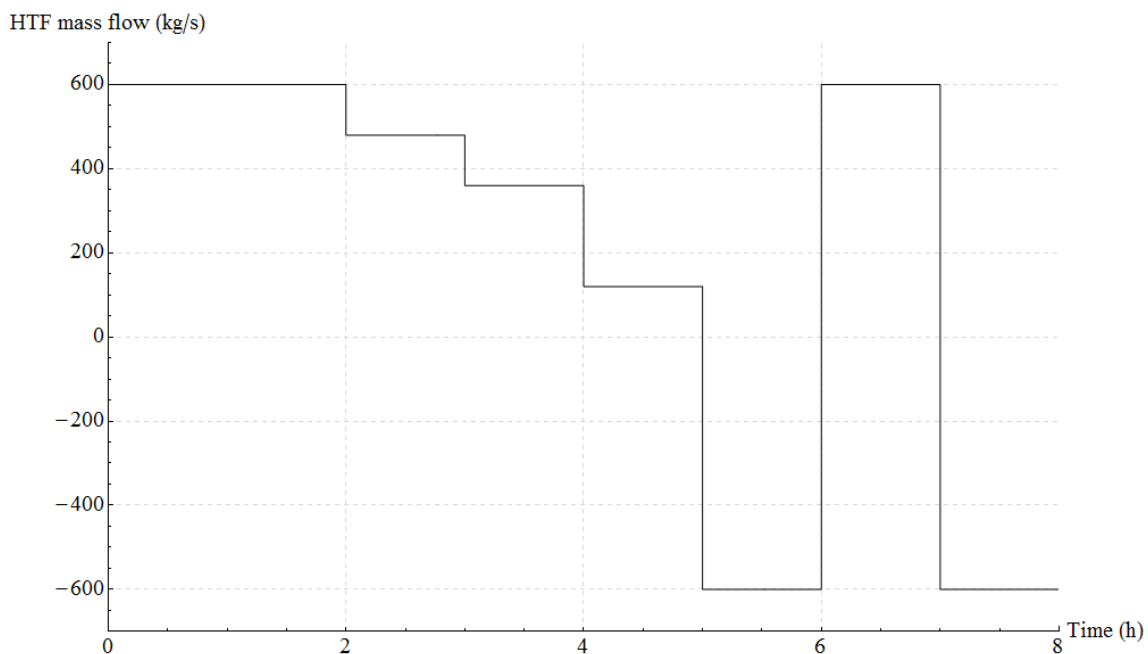


Figure 21: Idealized HTF mass flow rate boundary for the TES system (charging positive, discharging negative)

Figure 22 shows the corresponding molten salt mass flow of the conventional two-tank TES system. As the heat exchanger setup is counter-flow, the flow direction is inverted with respect to the HTF flow (see Figure 20 for positive flow directions). It can be seen well how the controller adjusts the salt mass flow rate to achieve the desired temperature set-points. In particular Figure 23 displays the molten salt outlet temperature (hot tank feed) for the first charging interval. Right after model initialization, it takes about half an hour until the nominal feed temperature (386 °C) of the hot tank is reached. Then, at the 3 following HTF mass flow reductions, the feed temperature of the hot tank is temporarily reduced until the controller balances the salt

mass flow again, which takes about 12 to 20 minutes. However, this kind of response is only relevant for the two-tank system. In the following, the temperature responses in the HTF circuit will be discussed.

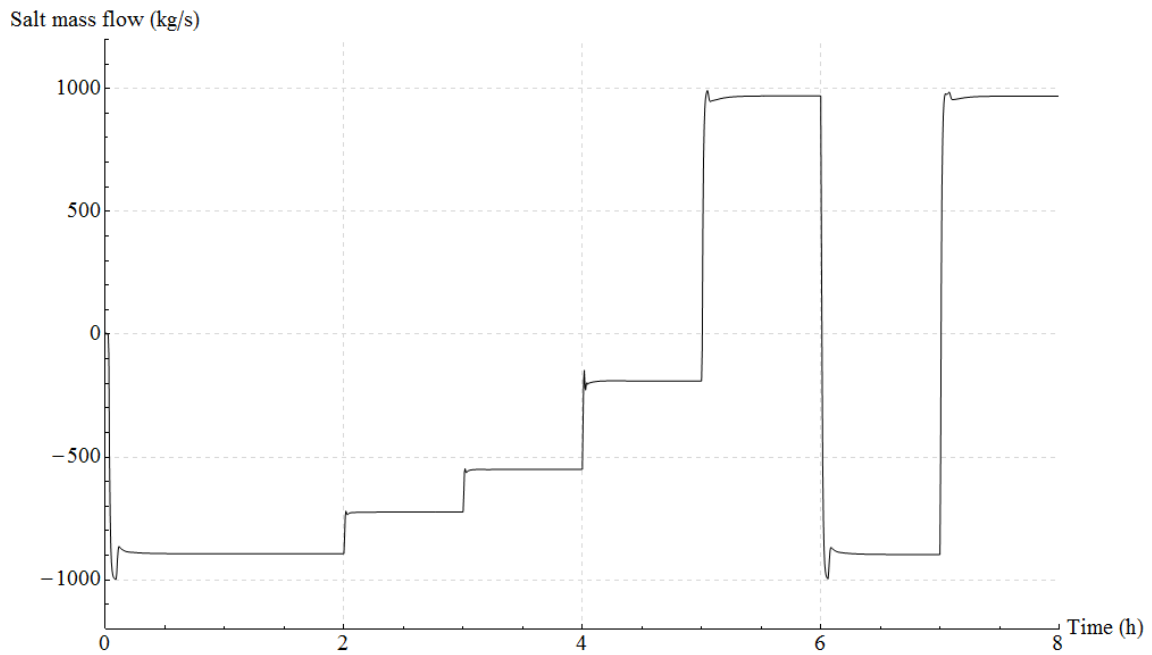


Figure 22: Molten salt mass flow rate according to idealized HTF mass flow boundary (see Figure 20 for positive flow directions)

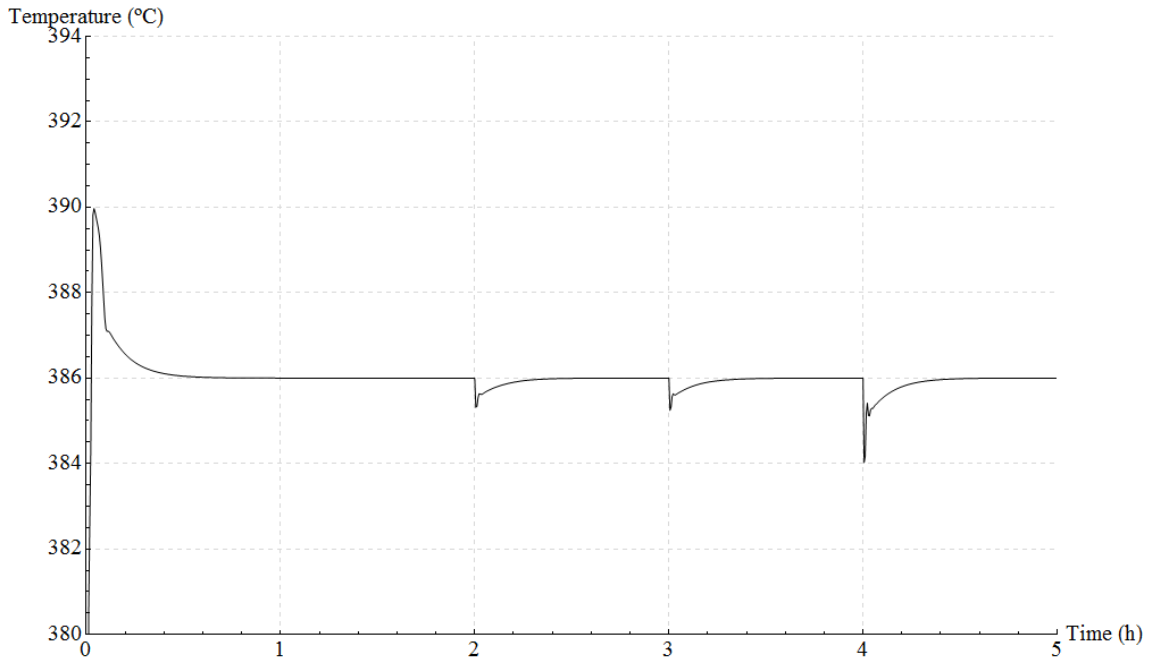


Figure 23: Molten salt temperature at heat exchanger outlet (hot storage tank inlet) – first charging interval

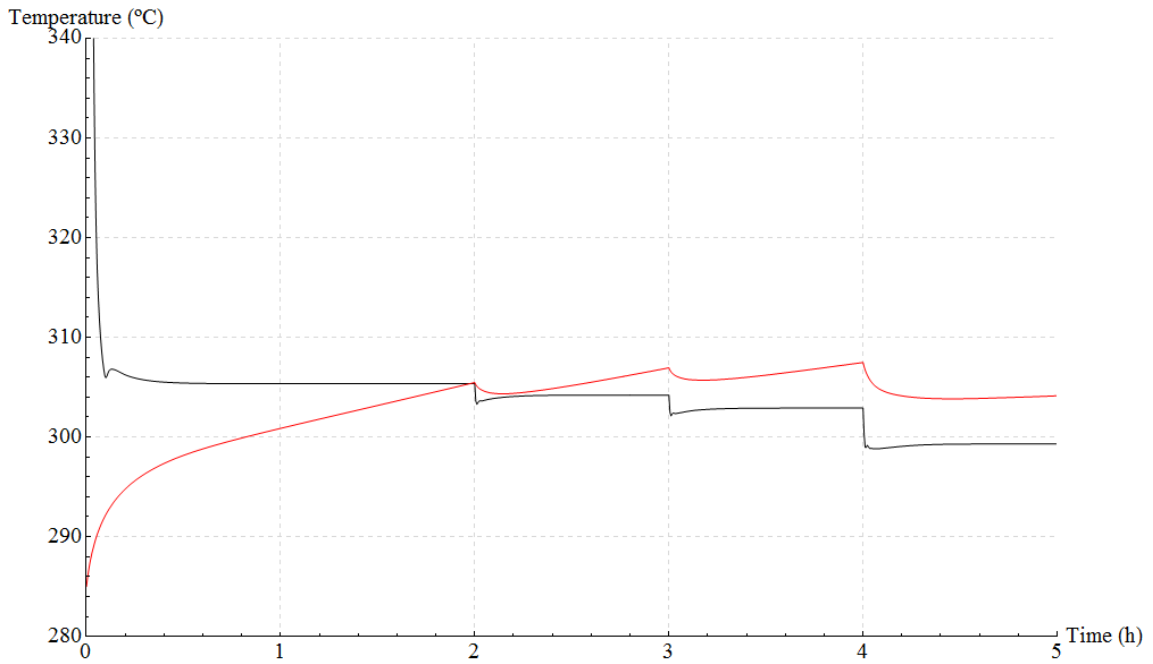


Figure 24: HTF outlet temperature (cold side) during first charging interval – two tank (black) and concrete (red)

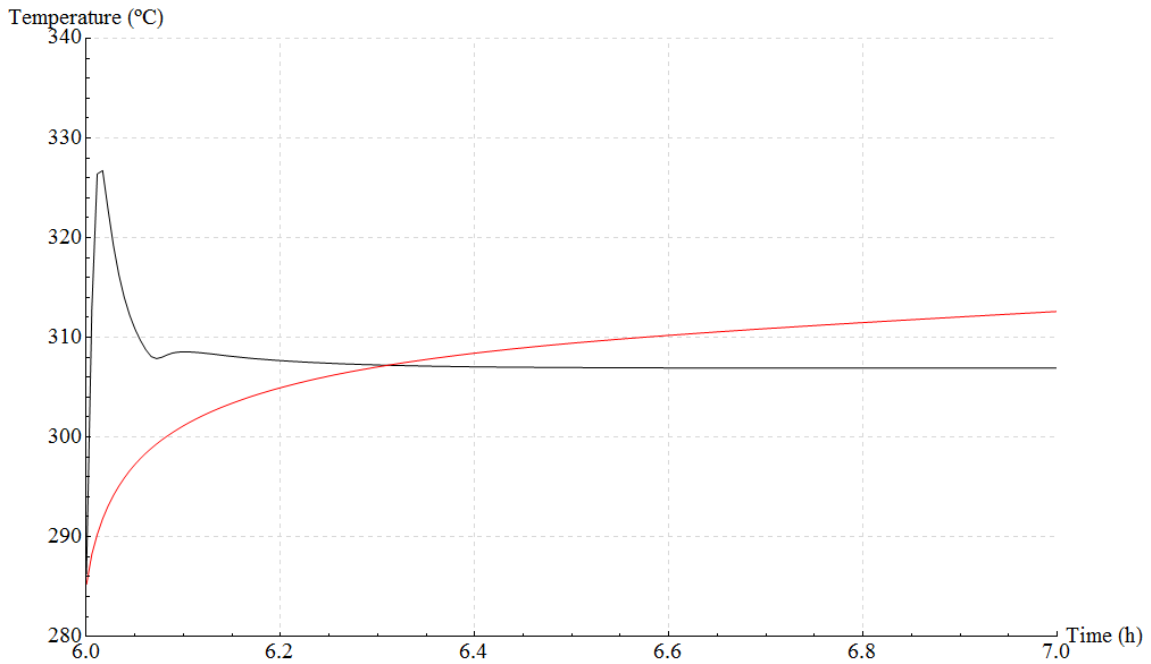


Figure 25: HTF outlet temperature (cold side) during second charging interval – two tank (black) and concrete (red)

Figure 24 displays the temperature response of the two TES systems during the first charging interval on the cold side (HTF outlet to solar field). The black solid line represents the conventional two-tank system, the red solid line represents the concrete system. The two-tank system reaches nominal steady operating conditions after 30 minutes of simulation. Then the HTF outlet temperature remains at its steady value until the HTF mass flow is reduced, where the HTF outlet temperature approaches its new steady value which is lower. The same holds for the following mass flow reductions. The concrete system on the contrary, does not have a constant outlet temperature for a given HTF mass flow rate due to the missing thermocline effect as discussed earlier. The HTF mass flow rate only influences the slope of the outlet temperature increase, which is obviously higher for higher mass flow rates. At each HTF mass flow decrease, a temporary HTF outlet temperature reduction can be observed, which is due to transients within the concrete TES system. Obviously, for the given radial temperature differences at switching time within the module, a smaller HTF mass flow will observe a larger temperature change. Also, at lower heat flows (lower charging rate), the radial temperature differences are smaller (see also Figure 28).

The systems behave correspondingly during the second charging interval, shown in Figure 25.

Figure 26 displays the HTF temperature response at the hot side (HTF outlet to steam generator) during the first discharging interval (simulation time: hour 5 to 6). The black solid line represents again the two-tank system, the red solid line represents the concrete system. At the moment of switching from charging to discharging, both systems start from the same temperature (391 °C), the solar field outlet temperature. After switching,

the two-tank system's salt mass flow controller needs to invert the salt mass flow and adjusts it such that the HTF outlet temperature set-point (376 °C) is reached. About 10 °C temperature difference remains in the heat exchanger as the molten salt inlet temperature is about 386 °C (nominal temperature of the hot tank). The new steady operating point is reached after about 24 minutes. From this point in time, the HTF outlet temperature would remain constant, if no further change in mass flow rate happened. For the concrete storage, on the contrary, no steady outlet temperature is reached. It keeps decreasing steadily until the cut-off temperature of 350 °C is reached.

Considering that the hot side of the storage system is connected with the plant's steam generator, any outlet temperature variation is transmitted to the steam generator inlet and must be taken into account for the thermal fatigue management. Typical rate-of-change limits in temperature for CSP steam generators constitute about 2-3 °C per minute, and are also indicated in Figure 26 as blue lines. The blue dashed lines are the 3 °C per minute limits (positive and negative slope), and the blue dotted lines are the 2 °C per minute limits (positive and negative slope). The constants of the line equations have been chosen such that the lines start at the upper and lower left corners of the figure. The constants of the line equations, i.e. the positions of the lines in the graphic, do not matter. Only the slope is relevant for visual comparison.

As can be observed in Figure 26, the maximum rate of change in HTF outlet temperature is much bigger for the conventional two-tank system right after the switching process is initiated, given the chosen control parameters. For the first minutes after the switching, the rate-of-change limits are clearly exceeded. Thus, the conventional two-tank system requires a certain HTF buffer volume between TES and steam generator to even out too strong temperature peaks. Advanced control methodologies could also be a solution for this issue.

The maximum rate of change in HTF outlet temperature of the concrete TES system is significantly lower than that of the conventional two-tank system (Figure 26). Nevertheless, during the first minutes after switching, the rate of change in HTF outlet temperature also exceeds the 3 °C per minute limit. Hence, also here, care must be taken considering the thermal fatigue management of the plant's steam generator.

Qualitatively, the same response can be observed for the second discharging interval (simulation time: hour 7 to 8), as shown in Figure 27. However, due to the bigger change in mass flow rate, the temperature overshoot of the two-tank system is bigger. Furthermore, due to the difference in radial temperature profile at the moment of switching (see Figure 28), the transient response of the concrete system is slightly less steep (compare red lines in Figure 26 and Figure 27).

Figure 28 shows the temperatures of the radial conduction nodes of the concrete layer at the center of the module (longitudinal grid element number 150). Concrete node 1 (CN 1) is the innermost node, concrete node 25 (CN 25) is the outermost node (see also Figure 3).

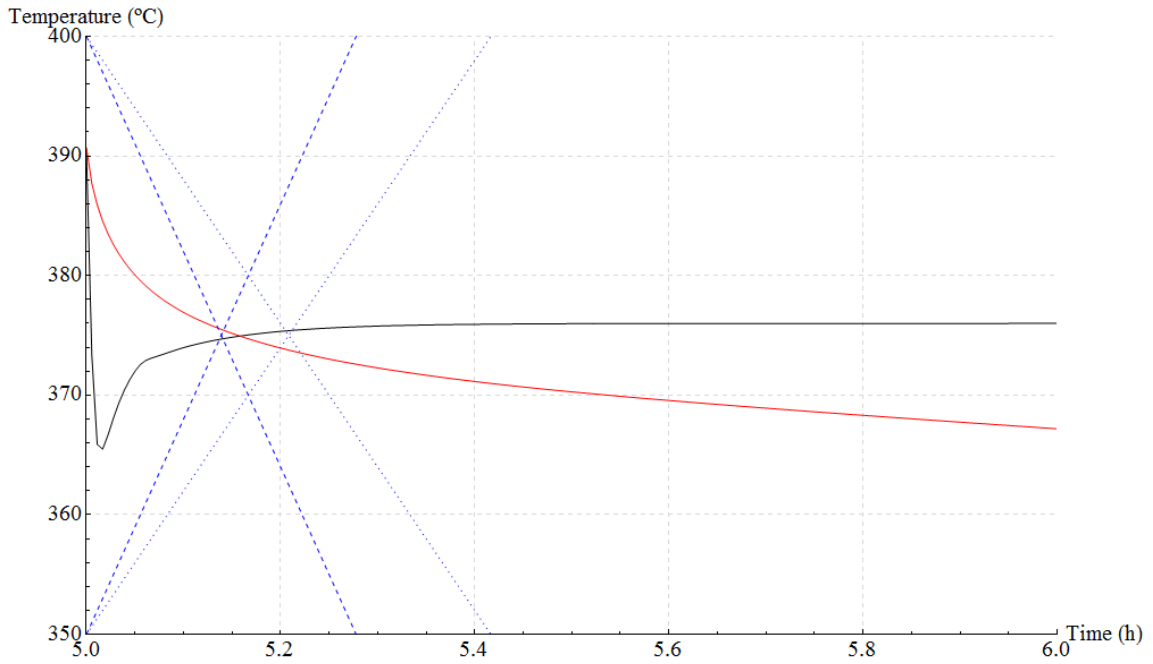


Figure 26: HTF outlet temperature (hot side) during first discharging interval – two tank (black) and concrete (red) – 3 °C per minute rate-of-change limit (blue dashed) – 2 °C per minute rate-of-change limit (blue dotted)

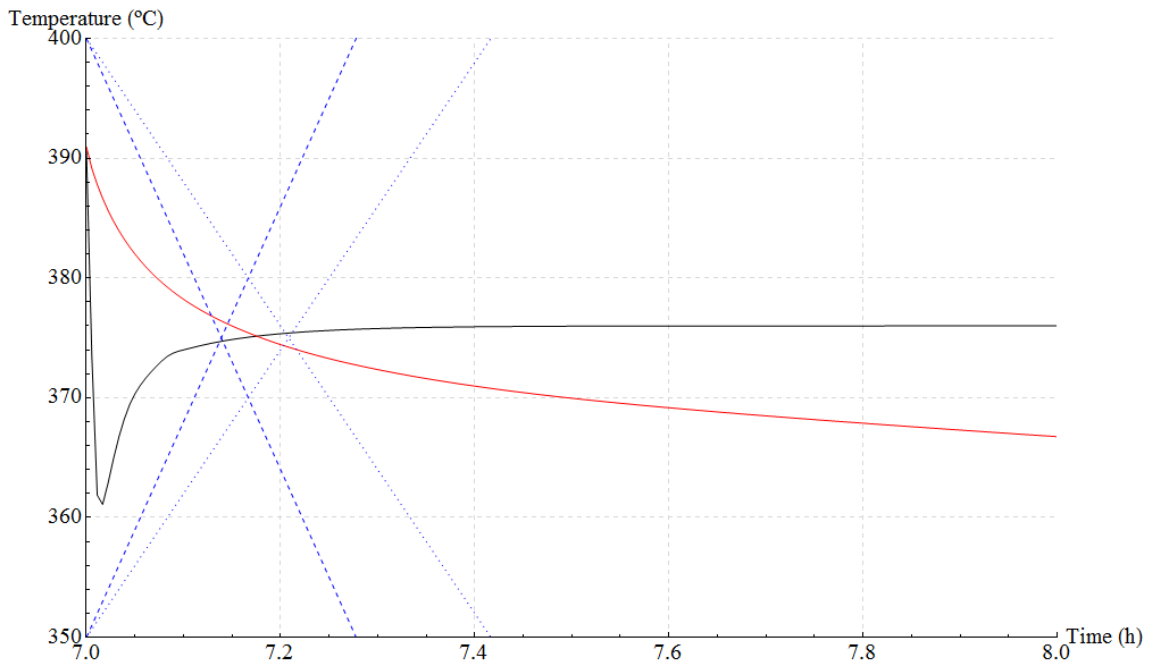


Figure 27: HTF outlet temperature (hot side) during second discharging interval – two tank (black) and concrete (red) – 3 °C per minute rate-of-change limit (blue dashed) – 2 °C per minute rate-of-change limit (blue dotted)

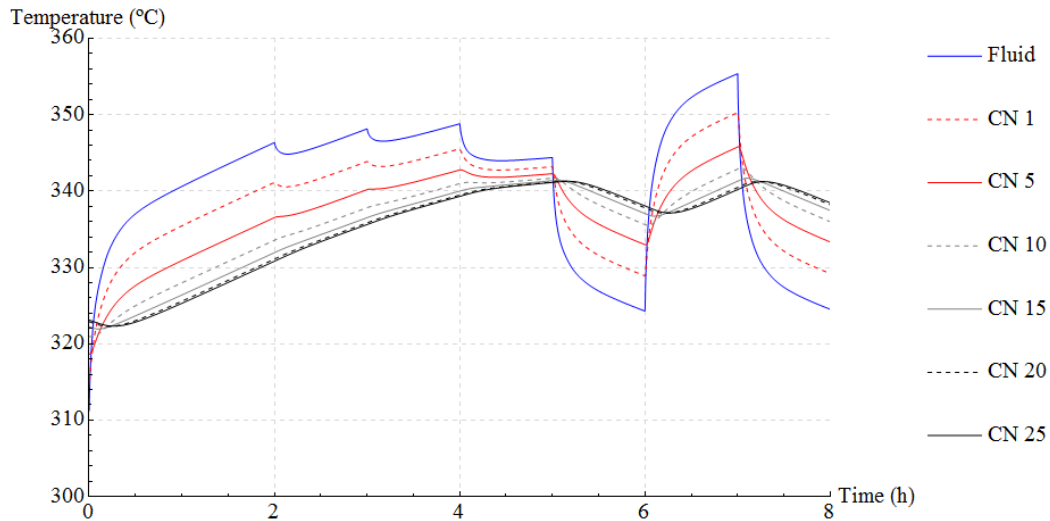


Figure 28: Temperature plot of radial conduction nodes in the concrete layer (concrete node 1 to concrete node 25) and the corresponding HTF control volume (blue) temperature at the center of the module (CV 150)

Finally, Figure 29, Figure 30 and Figure 31 display key simulation variables of the concrete TES system, in order to allow for future model comparison. Figure 29 displays the Reynolds number in the central control volume (CV 150). It can be seen how the transition region is entered at low partial charging loads (between hours 4 and 5). Figure 30 shows the corresponding Nusselt number, calculated according to Eq. (16). Figure 31 gives the forced convective heat transfer coefficient between HTF flow and tube inner surface for Newton's convective heat transfer law (see Eq. (10)).

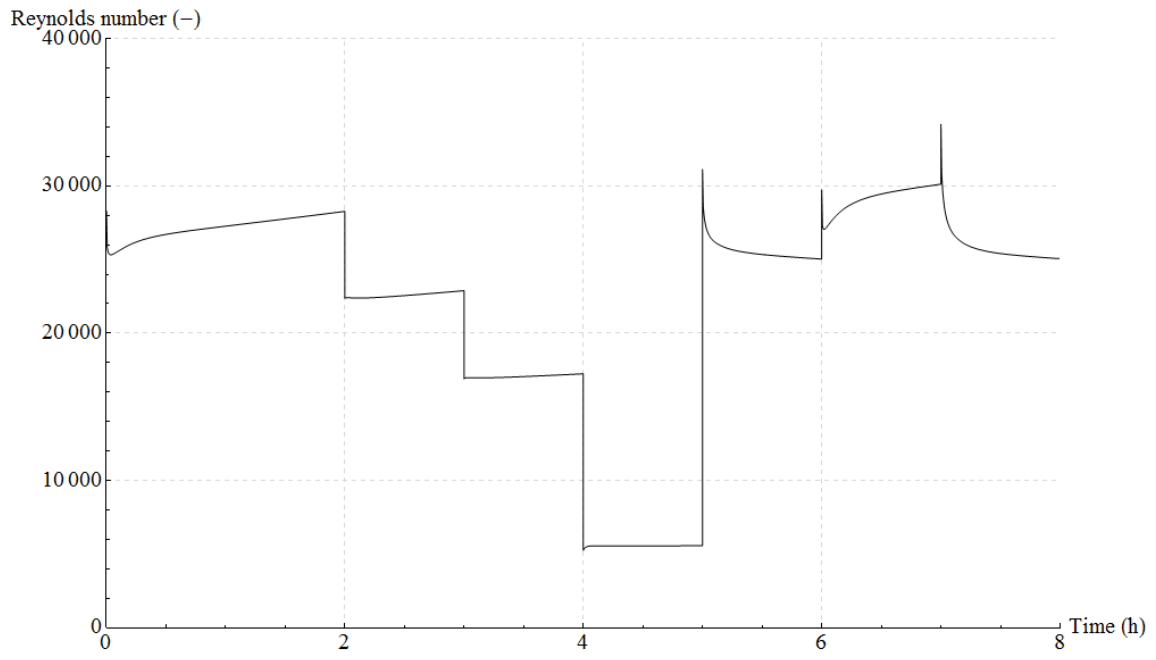


Figure 29: Reynolds number in the center (CV 150) of the concrete storage unit

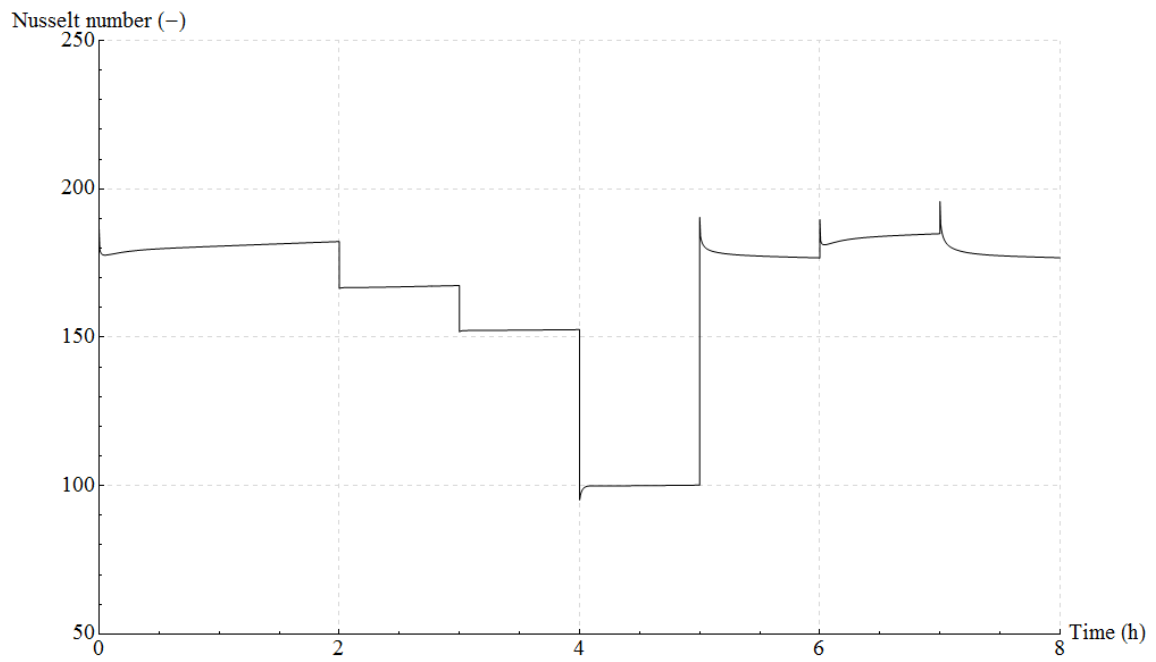


Figure 30: Nusselt number in the center (CV 150) of the concrete storage unit

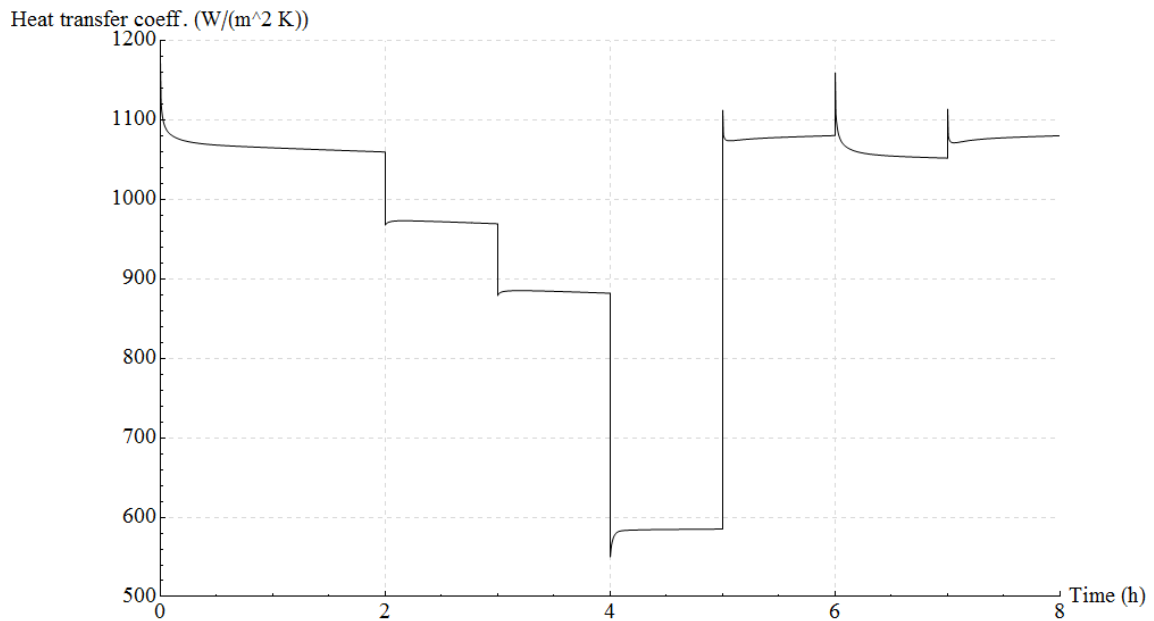


Figure 31: Forced convective heat transfer coefficient in the center (CV 150) of the concrete storage unit

In summary, in this section it is shown that the temperature response of the two evaluated TES concepts is fundamentally different. Whilst the innovative concrete TES system shows lower maximum rates of change in HTF outlet temperature right after the switching of operating modes, the conventional two-tank TES system has the important advantage of steady-state operation, providing constant HTF outlet temperature. For the concrete TES system, the HTF outlet temperature is variable over the whole operating range, due to the absence of a thermocline temperature profile, well known from packed-bed TES systems.

3.4 The impact of the HTF outlet temperature characteristics on the power cycle downstream

Besides the important influence of the transient response, which has to be taken into account for thermal fatigue management, also the impact of HTF the outlet temperature characteristic on the downstream power cycle has to be analyzed when comparing the two TES options. As it is well known from the principles of thermodynamics, the efficiency of the power cycle depends on the average temperatures at which heat is supplied to the cycle (T_{supply}), and rejected from the cycle ($T_{rejection}$). The ideal efficiency limit is given by the Carnot efficiency η_{Carnot} .

$$\eta_{Carnot} = 1 - \frac{T_{rejection}}{T_{supply}} \quad (17)$$

Considering the plant concept analyzed in this work, the upper temperature limit is defined by the HTF, which is chemically stable up to about 400 °C [12]. Thus, the nominal solar field outlet temperature is set to 391 °C to have a safety margin. The live steam temperature of the downstream Rankine cycle is typically 371 °C, considering a HTF steam generator inlet temperature of 391 °C. However, in TES discharging mode, the HTF inlet temperature is considerable reduced. In the case of the conventional two-tank TES system, the HTF inlet temperature constitutes 376 °C, which reduces the live steam temperature in discharging mode to about 366 °C. For the innovative concrete storage system, the HTF inlet temperature decrease is even down to 350 °C, which means live steam conditions at about 343 °C at 72 bar (see Figure 32 and Figure 33). This has a considerable impact on the operation of the Rankine cycle, which will be analyzed in the following.

Figure 32 shows a zoomed version of Figure 15 (cyclic steady-state simulation of the concrete TES) in order to display the HTF inlet temperature to the steam generator as function of time (red line). Since the cyclic steady-state discharging time of about 4.5 hours is quite low, two concrete TES units (252 modules each) are assumed to be discharged sequentially, that is, once the first system is empty, the HTF mass flow is redirected to the second TES unit (instantaneous switching is assumed). Thus, after half of the discharging operation we can observe a HTF temperature spike back to 391 °C outlet temperature. The corresponding HTF steam generator inlet temperature of the conventional two-tank TES unit is shown as black line (376 °C set-point). Note that the two-tank system is assumed to be slightly oversized, in order to provide 9 hours discharge operation at nominal load. The temperature profiles in Figure 32 are taken for the part load simulation of the Rankine steam cycle.

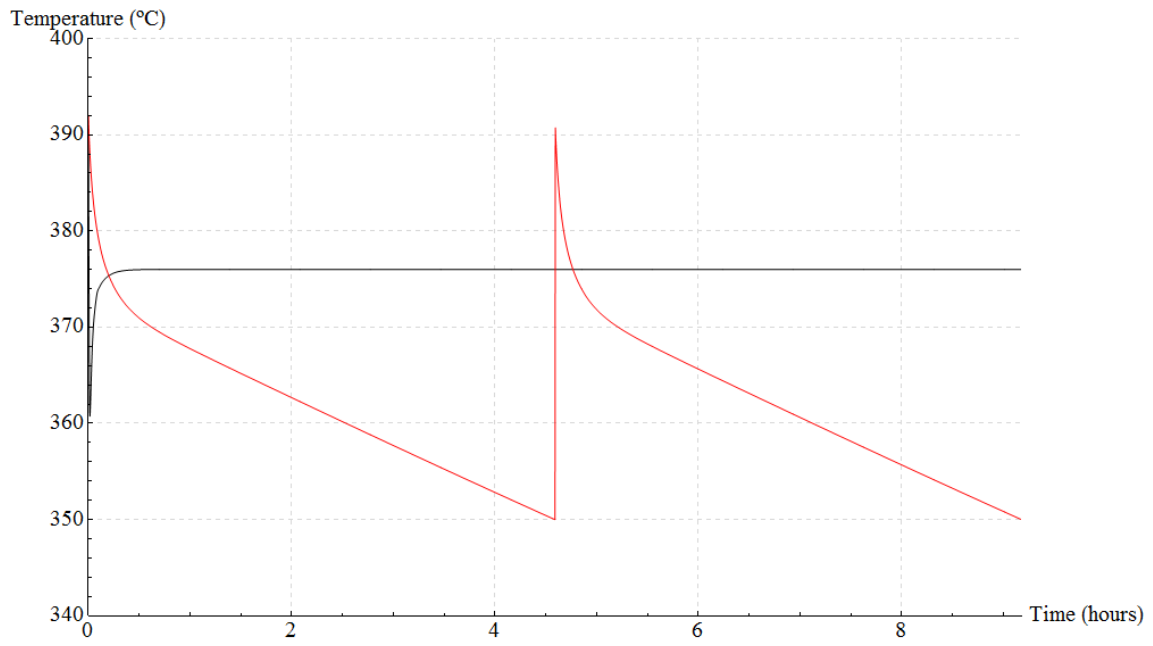


Figure 32: Storage system HTF outlet temperatures: two-tank TES (black) and concrete TES (red)

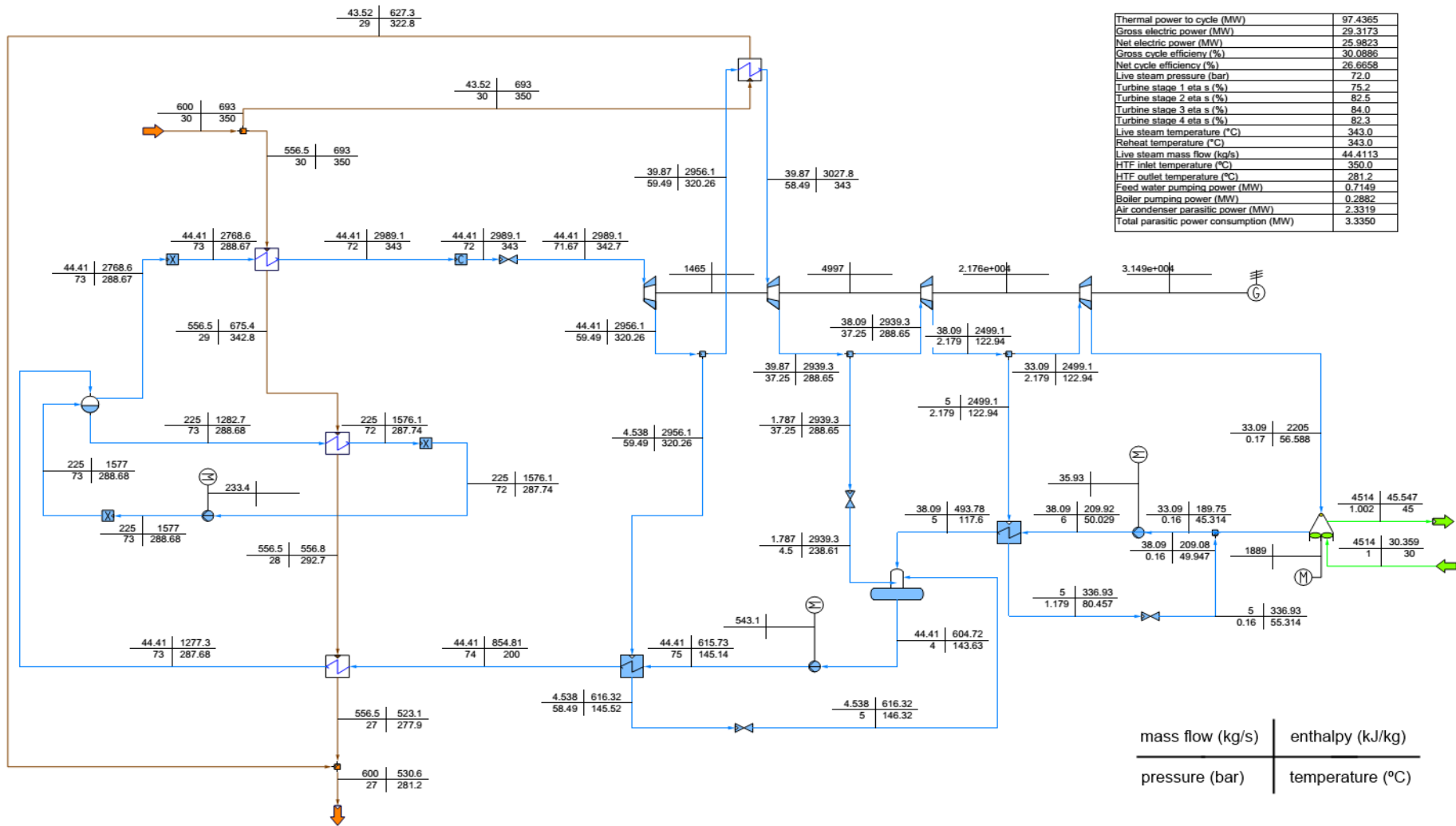


Figure 33: Rankine cycle model – 350 °C HTF inlet temperature – Live steam conditions: 72 bar, 343 °C

3.4.1 Rankine steam cycle configuration and its modeling

The assumed layout of the Rankine steam cycle is shown in Figure 33. The steam generator consists of 3 heat exchanger units in series, the economizer, the evaporator and the superheater. The evaporator is assumed as forced circulation boiler, having a recirculation ratio of about 5. A four stage extraction turbine is assumed to allow regenerative feed water preheating (two preheaters and one deaerator). The first stage is an impulse stage, followed by 3 reaction stages. The cycle has one reheat after the first turbine stage. The condenser is air-cooled (forced-draft direct air-cooled A-frame condenser units [31]). The ambient temperature is considered to be 30 °C.

Since the thermal power supplied by the TES units is variable, resulting in a variable steam mass flow, with respect to nominal operation (concrete TES in particular), it is important to model the turbine in part load. The isentropic efficiencies (η_s) of each stage are thus a function of steam mass flow. Table 3 shows the assumed nominal values and a typical part load relationship according to EDF's ThermoSysPro library [32].

Table 3: Isentropic efficiency values for the turbine stages

Mass flow ratio turbine ($\dot{m}/\dot{m}_{nominal}$)	η_s impulse stage (stage 1)	η_s reaction stages (stage 2-4)
1	0.84	0.9
0.9	0.83	0.89
0.8	0.8	0.86
0.7	0.74	0.8
0.6	0.65	0.71
0.5	0.53	0.59
0.4	0.39	0.45
0.3	0.21	0.28

The mass flow through the turbine is determined by the steam generator (live steam temperature set point). The turbine exit pressure is set to the condenser pressure level (0.17 bar) and the inlet pressure of the stages upstream is calculated according to Stodola's elliptic law. At nominal conditions (391 °C HTF inlet temperature, mass flow 600 kg/s), live steam conditions are 371 °C at 98 bar. The resulting nominal steam mass flow admitted to the turbine is 60 kg/s. The reheat temperature is 371 °C.

The power cycle has been implemented and simulated using a state-of-the-art process simulation software [33], which computes the steady-state energy and mass balance of the system shown in Figure 33. The heat exchanger component models are implemented according to the logarithmic mean temperature difference method [34] assuming pure counter flow arrangement. The HTF fluid properties are implemented according to Ref. [12]. The water/steam properties are implemented according to the IAPWS (International Association for the Properties of Water and Steam) Industrial Formulation 1997 [35]. A combination of

the constant pressure mode and the sliding pressure mode is used for part load simulation of the power cycle.

A linear part load efficiency correlation between 29.7% cycle net efficiency at 391 °C HTF inlet temperature, and 26.7% cycle net efficiency at 350 °C HTF inlet temperature has been derived from the power cycle simulations.

3.4.2 Impact of the storage units' outlet temperature characteristic on power cycle and the electric energy output

Figure 36 shows the cycle conversion efficiencies for both storage concepts based on the HTF inlet temperatures given in Figure 32. While the conversion efficiency of the conventional two-tank TES system is obviously constant ($\approx 28.6\%$) after the switching transients have faded, the cycle efficiency of the concrete TES steadily decreases during the whole discharging phase. Figure 34 shows the thermal power supplied to the cycle by both TES options (constant HTF mass flow of 600 kg/s). Figure 35 plots the thermal energy supplied to the power block (two-tank TES – black, concrete TES – red). Figure 37 shows the electric power generated, the product of thermal power and corresponding conversion efficiency. Finally, Figure 38 displays the generated electric energy for both TES configurations. It can be seen that the conventional two-tank TES unit outperforms the concrete TES configuration clearly. For a given HTF mass flow, the conventional two-tank system is able to deliver a higher thermal power due to the bigger HTF temperature difference achieved. The conventional two-tank TES provides 91 °C of HTF temperature difference (376 °C – 285 °C), whereas the concrete TES provides on average only about 77 °C HTF temperature difference during discharging (362 °C – 285 °C). Due to this difference, the concrete TES system can only provide about 85% of the thermal power, compared to the conventional two-tank system. Obviously, also the thermal energy supplied to the steam generator is lower by this fraction (see Figure 35).

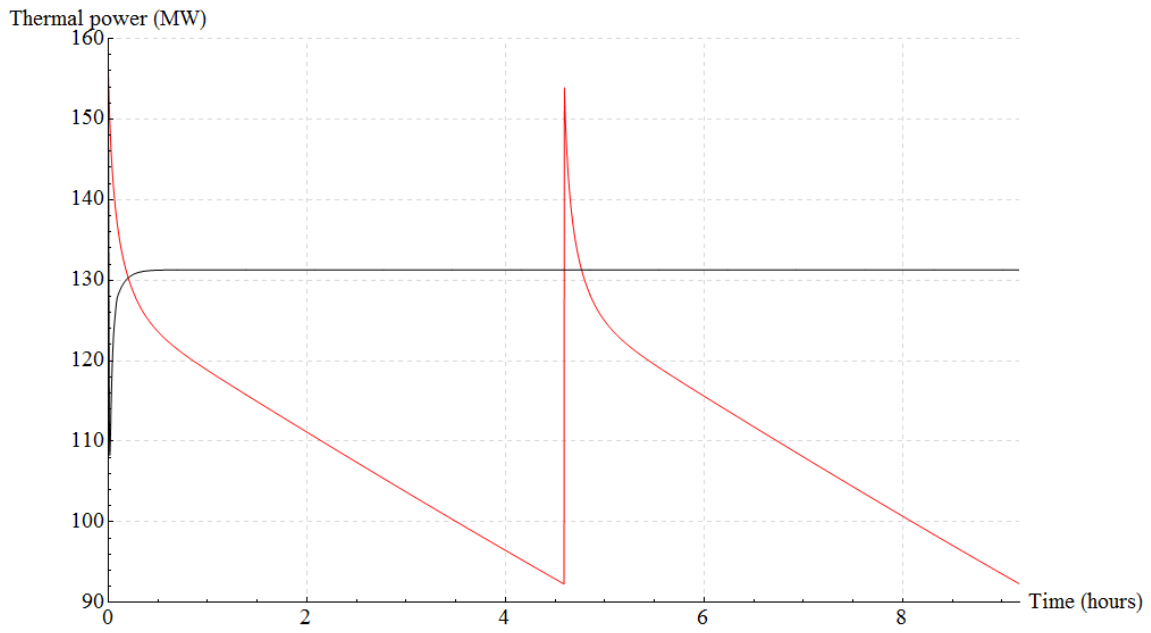


Figure 34: Thermal power to power cycle: two-tank TES (black), concrete TES (red)

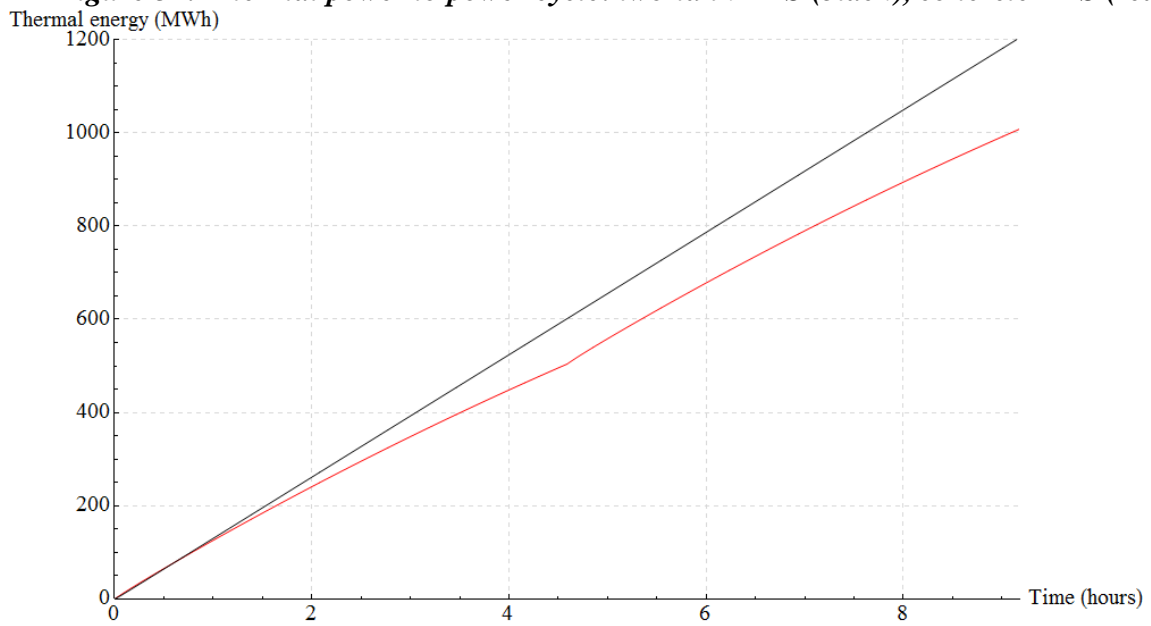


Figure 35: Thermal energy discharged to power cycle: two-tank TES (black), concrete TES (red)

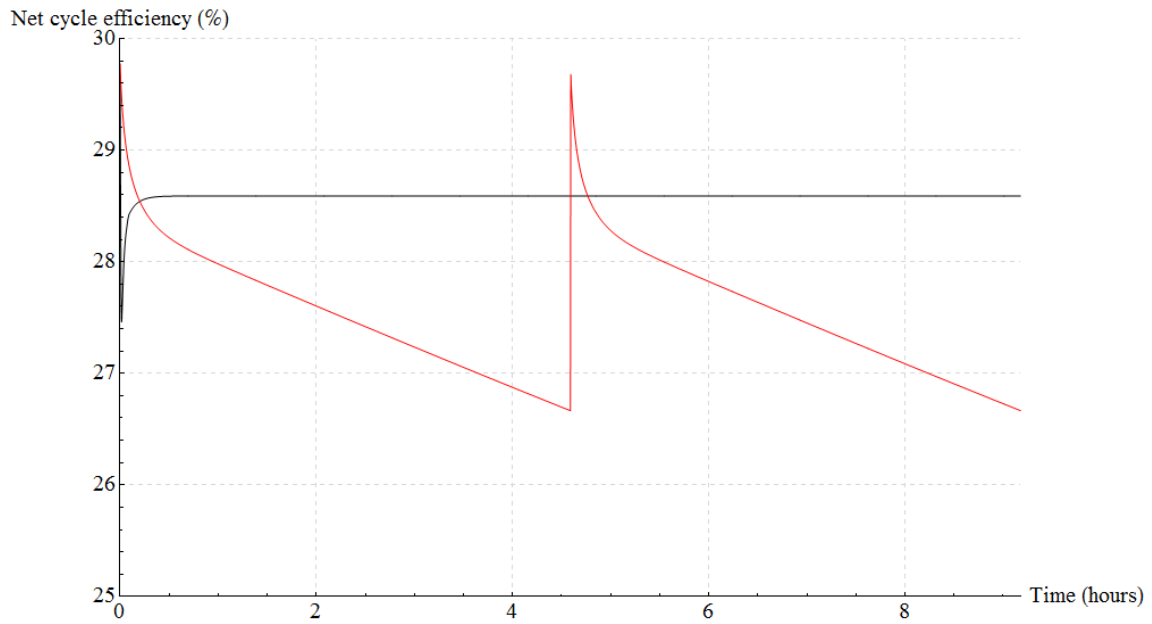


Figure 36: Power cycle net conversion efficiencies: two-tank TES (black), concrete TES (red)

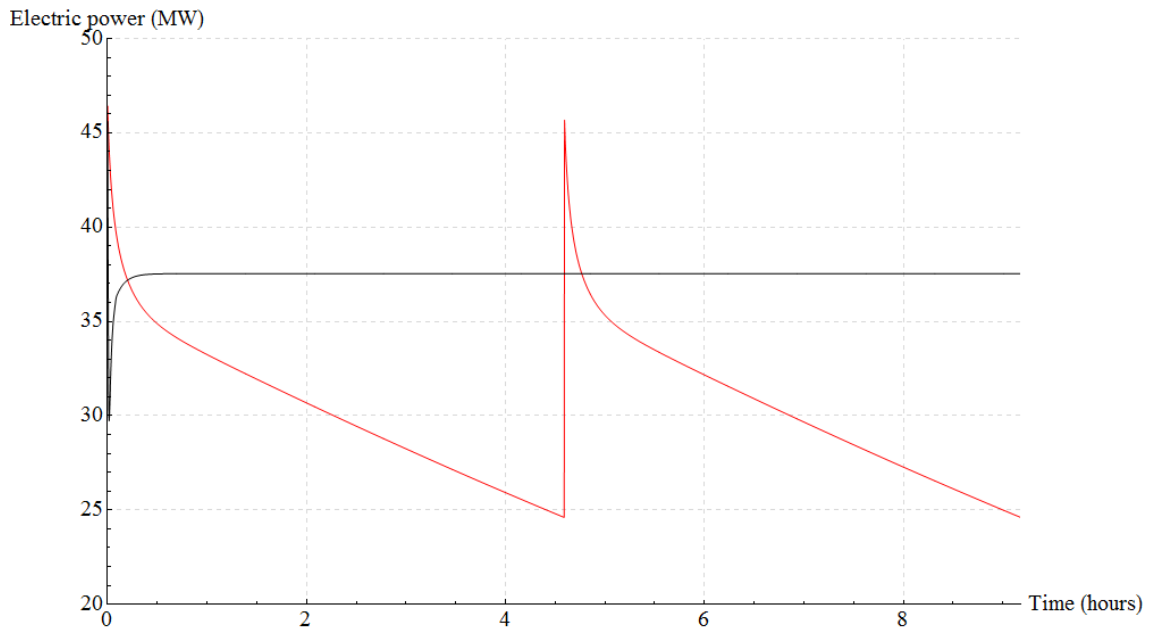


Figure 37: Power cycle electric power output: two-tank TES (black), concrete TES (red)

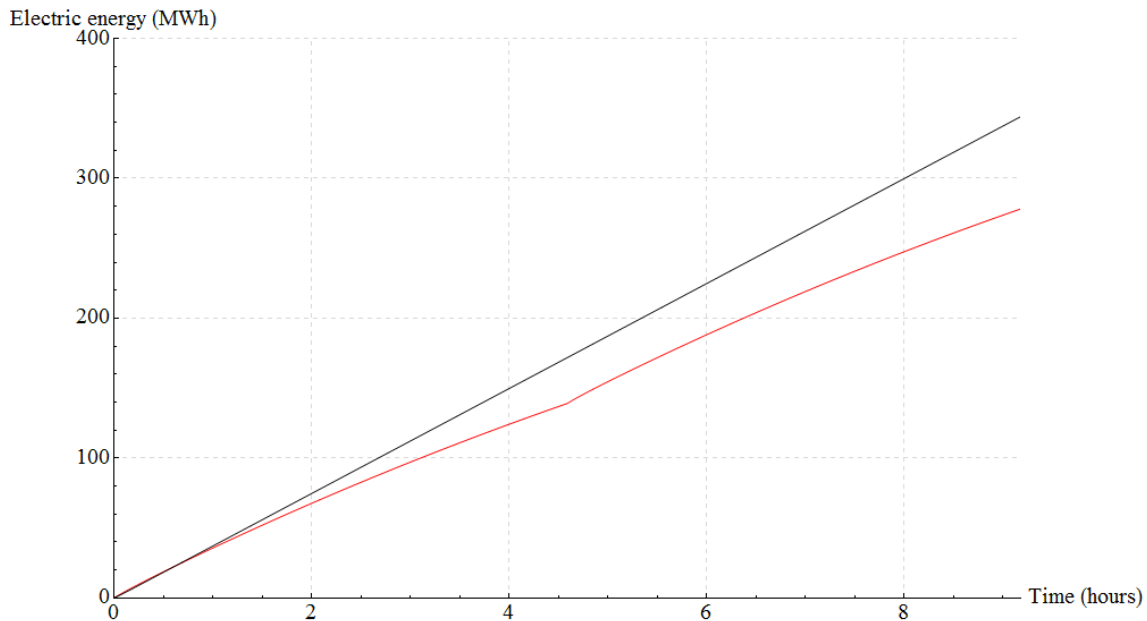


Figure 38: Electric energy generated: two-tank TES (black), concrete TES (red)

According to these simulation results, it is clear that the proposed alternative concrete TES option needs to be designed very carefully with respect to module design and connecting configuration. The proposed configuration (18 parallel rows, having 14 modules - Table 1 - connected in series in each row [2]) provides only 504 MWh of thermal capacity during discharging, in cyclic steady-state conditions. Two such systems operated sequentially provide about 1008 MWh thermal.

Furthermore, the thermal-to-electric conversion efficiency of the concrete TES system will be always lower, due to the lower HTF steam generator inlet temperature (Carnot) and the part load operation of the steam turbine. On average, the thermal-to-electric conversion efficiency is by 1.1 percentage points (or about 4%) lower (28.6% vs. 27.5%). This means that the solar field needs to be oversized by about 4%, with respect to the conventional two-tank system, in order to provide the same electric output.

In summary, for a given HTF mass flow in discharging operation, the thermal power extracted from the concrete TES system is about 15% lower, and additionally, the thermal-to-electric conversion efficiency is on average 4% lower. This leads to a reduction of produced electricity by about 19% (see Figure 38), based on the performance of the conventional two-tank system and identical HTF boundary conditions.

These disadvantages may likely neutralize the cost advantage of the concrete TES system, not to mention the increased complexity of the power cycle control during continuously varying load and temperature set-point variations (live steam and reheat temperature, and drum pressure).

3.5 Conclusions and outlook

This work presents a 1-D numerical model of a passive sensible thermal energy storage system using concrete as storage medium. It has been successfully validated against

experimental data [5] obtained from a pilot-scale concrete storage module. A specific Nusselt number correlation (Eq. (16)) has been developed providing better accuracy for the specific HTF (Therminol VP1) and observed Reynolds numbers than conventional general purpose heat transfer correlations for forced convection inside tubes. The model has been up-scaled to a commercial-size capacity, providing grid-independent solutions and cyclic-steady-state initialization values for further use in a general purpose CSP model library. The proposed implementation in Modelica provides a flexible and intuitive simulation tool, which is not limited to a single simulation platform.

Next, the presented model of the concrete TES system is used to compare its transient response with that of a conventional active indirect two-tank heat storage system. It is shown that the temperature response of the two evaluated TES concepts is fundamentally different, which is however obvious, being one of regenerator type.

Firstly, the HTF outlet temperature of the innovative concrete TES system is variable over the whole operating range, due to the absence of a classical thermocline temperature profile, which is well known from packed-bed TES systems. On the contrary, the conventional two-tank system provides for each operating point a steady-state HTF return temperature. In particular in discharging mode, the HTF steam generator inlet temperature can be kept constant at 376 °C, which is very favorable considering steam cycle efficiency and thermal fatigue management, where certain rate-of-change limits for component wall temperatures must be minded.

Secondly, the innovative concrete TES system shows lower maximum rates of change in HTF outlet temperature right after the switching of operating modes. This can be seen as slight advantage over the conventional two-tank TES system. Nevertheless, both systems require a certain HTF buffer volume between TES and steam generator to even out too strong temperature peaks. The performance of the conventional two-tank TES system could also be improved by applying advanced control methods.

Regarding the impact on the power cycle downstream the TES systems, 3 remarks can be given:

- The thermal power that can be extracted from the concrete TES system is typically lower (15% lower for the here considered parameters), due to a smaller HTF temperature difference.
- Also the thermal-to-electric conversion efficiency downstream the concrete TES system is lower (on average 4% lower, for the here considered parameters) due to a lower HTF steam generator inlet temperature (Carnot) and part load operation of the steam turbine.
- The concrete TES system must be carefully designed with respect to the cyclic steady state performance (true thermal capacity)

In order to mitigate these issues, advanced module connection configurations and operation strategies must be studied that allow for less variation in HTF outlet temperature. However, it seems to be difficult to maintain the cost advantage over the conventional two-tank TES option, due to increased complexity (additional valves, control, piping etc.).

4. Performance comparison of advanced thermal energy storage systems through simulations (FISE)

4.1 Technology overview and configurations

Different system combinations comprising different collector technologies, solar field layouts, heat transfer fluid, heat storage media and storage technologies are analyzed. The different options per category that have been analyzed are shown in Table 4:

Table 4: Analyzed options

Category	Option 1	Option 2	Option 3
Collector	PTC	LFC	
HTF	VP1	Solarsalt	Hitec
TES	Two-tank	Single-tank	
HSM	Solarsalt	Hitec	

The combinations shown in Table 5 have actually been analyzed.

Table 5: Analyzed combinations

No.	Collector	Orientation	HTF	TES	HSM
1	PTC	N-S	VP1	Two-tank	Solarsalt
2	PTC	N-S	Solarsalt	Two-tank	Solarsalt
3	PTC	N-S	Solarsalt	Single-tank	Solarsalt
4	LFC	N-S	Solarsalt	Two-tank	Solarsalt
5	LFC	E-W	Solarsalt	Two-tank	Solarsalt
6	PTC	N-S	Hitec	Two-tank	Hitec
7	PTC	N-S	Hitec	Single-tank	Hitec
8	LFC	N-S	Hitec	Two-tank	Hitec
9	LFC	E-W	Hitec	Two-tank	Hitec

Combination #1 is taken as reference case. Besides this case, 4 combinations each for PTC and LFC have been analyzed. In case of PTC the special combination is the variant to replace the two-tank system by a single-tank system. In case of LFC, the orientation is also changed to an E-W layout in addition to the N-S layout.

All the simulations are carried out for a 50 MW_{el} power block system which is air-cooled and uses single-stage reheat turbine.

4.2 System design and cost assumptions

An overview of the solar field parameter for the different collectors and HTF is shown in Table 6. Since the simulations are carried out for a wide range of aperture area, the parameters in Table 6 are given for a SM of 1.

Table 6: Design parameter for the solar field including different HTF options

		VP1	Solarsalt		Hitec	
Collector		PTC	PTC	LFC	PTC	LFC
SCA length	m	142.8	142.8	44.8	142.8	44.8
Aperture	m	5.77	5.77	12	5.77	12
SCA per loop	-	4	8	20	8	20
Loop length	m	571.2	1142.4	896	1142.4	896
Inlet temperature	°C	293	290	290	290	290
Oultet temperature	°C	393	550	550	520	520
Max. HTF flow per loop	kg/s	7.04	14.88	14.88	14.57	14.57
Design power per loop	MW _{th}	1.72	3.63	4.89	3.71	4.95
Number of loops for SM 1	-	76	36	26	36	26
Aperture area for SM 1	m ²	250483	237299	279552	237299	279552
Power for SM 1	MW _{th}	134.7	130.8	127.1	133.6	128.7
Real SM	-	0.99	1.04	1.01	1.04	1
Design HTF flow	kg/s	570	332	325	338	310

An overview of the TES system for the different HTFs is shown in Table 7. Since the simulations are carried out for a wide range of storage capacities, the parameters in Table 7 are given for a storage capacity of 12 h. In the two-tank system a minimum level of 0.9 m per tank is assumed which results in a dead volume of 7% for a tank with a height of 12.9 m.

Table 7: Design parameters for the two-tank storage system with a 12 h capacity

		VP1	Solarsalt	Hitec
Capacity	MWh _{th}	1632	1510	1546
Temperature HT	°C	386	550	520
Temperature CT	°C	296	290	265
Volume HT	m ³	25340	8522	8455
Volume CT	m ³	24523	7782	7609
Usable storage mass	t	43479	13795	13397
Discharge power	MW _{th}	120*	125.8	128.9

The design parameters of the power block system are shown in Table 8.

Table 8: Design parameter of the power block system

		VP1	Solarsalt	Hitec
Live steam temperature	°C	384	541	511
Live steam pressure	bar	100	100	100
Reheat steam temperature	°C	384	541	511
Reheat steam pressure	bar	20	20	20
Condensation pressure	bar	0.08	0.08	0.08
Efficiency HP-turbine	-	0.85	0.85	0.85

* limited by the heat exchanger in discharge operation

temperature from the steam generator system increasing the temperature rise in the system but also reducing the efficiency.

The main difference in the performed analysis is the collectors, the HTF or the HSM respectively. The specific cost of the subsystems is thus given for the different options. The specific cost for the solar field is given in Table 9. There will be no cost difference for the solar field for the different salts.

Table 9: Relative cost for the solar field[†]

	PTC + VP1	PTC + Salt	LFC + Salt
Infrastructure & Earthworks	1	1	0.86
Solar collector	9.27	9.29	6.32
HTF system	3.51	5.56	3.79
Total specific cost	13.78	15.86	10.97

In the case of the storage system the cost mainly depends on the amount and type of salt. For Solarsalt and HITEC cost, relative cost comparing with VP1 is assumed, which together with the cost of collectors are shown as in Table 9. The cost further depends on the amount of steel required for the tank wall and other minor items such as foundation, insulation, instrumentation etc. Despite the higher temperature difference in the HITEC storage system which leads to less salt inventory and smaller tanks, the specific cost for the HITEC system are slightly higher than that of the direct Solarsalt. As expected there is a large difference to the indirect system using VP1 as HTF. A specific cost comparison is shown in Table 10.

Table 10: Relative storage cost overview for the three different HTF[‡]

HTF	C_TES
VP1	1
HITEC	0.44
SS	0.42

There is a slight cost difference between the storage configurations depending on the corresponding solar field size since the cost for pumps are included in the storage cost. The cost for the cold pump which supplies molten salt for the solar field depends on the solar field size. However, cost increase for the salt pump is rather low compared to the other cost items. Beside the main pump, the cost the circulation pump during anti-freeze operation and the initial salt melting are included in the CAPEX for the storage. An exemplary cost breakdown for the storage will be shown by following.

Since the power block size is always the same for all configurations, there are only minor differences in the power block cost e.g. caused by the material for the steam generator, temperature of the turbine casing or different numbers of feedwater heater units or air cooling

[†] Reference case (PTC+VP1) cost is set as 1

[‡] Reference case (VP1) cost is set as 1

bays. The cost is independent of the collector technology and shown in Table 11 for the three different HTF.

Table 11: Power block cost overview for the three different HTFs[§]

HTF	Relative Invest Cost
VP1	1
HITEC	1.02
SS	1.05

For the calculation of the LCOE further cost items are taken into consideration such as the land or engineering cost. These costs are listed in Table 12.

Table 12: Cost items and assumptions for the LCOE calculation

Cost item	Unit	Value
PTC Land utilization factor $f_{land,PTC}$	-	0.4
LFC Land utilization factor $f_{land,LFC}$	-	2.3
Cost for land c_{land}	€ m ⁻²	2.5
Other cost C_{other}	-	0.00
Risks f_{risk}	-	0.00
EPC cost f_{EPC}	-	0.11
Taxes f_{tax}	-	0.06
Interest rate i	-	0.06
Life time l	a	30
Fix O&M cost $c_{O\&M,fix}$	€ kW _{el} ⁻¹	55
Variable O&M cost $c_{O\&M,var}$	€ MWh _{el} ⁻¹	22
Gas price for freeze	€ MWh _{th} ⁻¹	

The LCOE is calculated according to

$$LCOE = \frac{(C_{direct} + C_{indirect}) AF + C_{O\&M}}{E_{net}}$$

where the C_{direct} are the direct cost, $C_{indirect}$ the indirect cost, AF the annuity factor and $C_{O\&M}$ the cost for operation and maintenance and E_{net} the net electric yield. The direct cost consist of

$$C_{direct} = (1 + f_{risk})(C_{SF} + C_{TES} + C_{ORC} + C_{other}),$$

the indirect cost of

$$C_{indirect} = (1 + f_{land})A_{SF}c_{land} + (f_{EPC} + f_{tax})C_{direct},$$

the O&M cost have fix and variable part

$$C_{O\&M} = c_{O\&M,fix}P_{ORC} + c_{O\&M,var}E_{net}$$

[§] Reference case (VP1) cost is set as 1

and the annuity factor is calculated according

$$AF = i \frac{(1 + i)^l}{(1 + i)^l - 1}$$

which leads to an annuity factor of 0.087. The sum of direct and indirect cost represents the total CAPEX of the plant.

Using the specific cost for the solar field and design data for the solar field, the investment cost for the solar field aperture which results in SM of 1 can be calculated. The results are displayed in Table 13.

Table 13: Investment cost for the different collector technologies and HTF for a solar multiple of 1**

HTF		VP1	Solarsalt		Hitec	
Collector		PTC	PTC	LFC	PTC	LFC
Aperture area for SM 1	m ²	250483	237299	279552	237299	279552
Real SM	-	0.99	1.04	1.01	1.04	1.00
Spec. SF cost	/m ²	1	1.15	0.80	1.15	0.80

It can be seen that the systems using linear Fresnel collector have the lowest investment cost to provide the design power calculated for Solar Multiple of 1. The effect of the annual optical efficiency on the LCOE will be shown later.

4.3 Simulation and operating strategy

Simulations have been carried out with Fraunhofer ISE's system simulation software ColSim CSP. The weather and geographical data are taken for Guadix in Spain. The annual DNI of the used weather file is 2081 kWh/m²a.

** Reference case (PTC+VP1) cost is set as 1

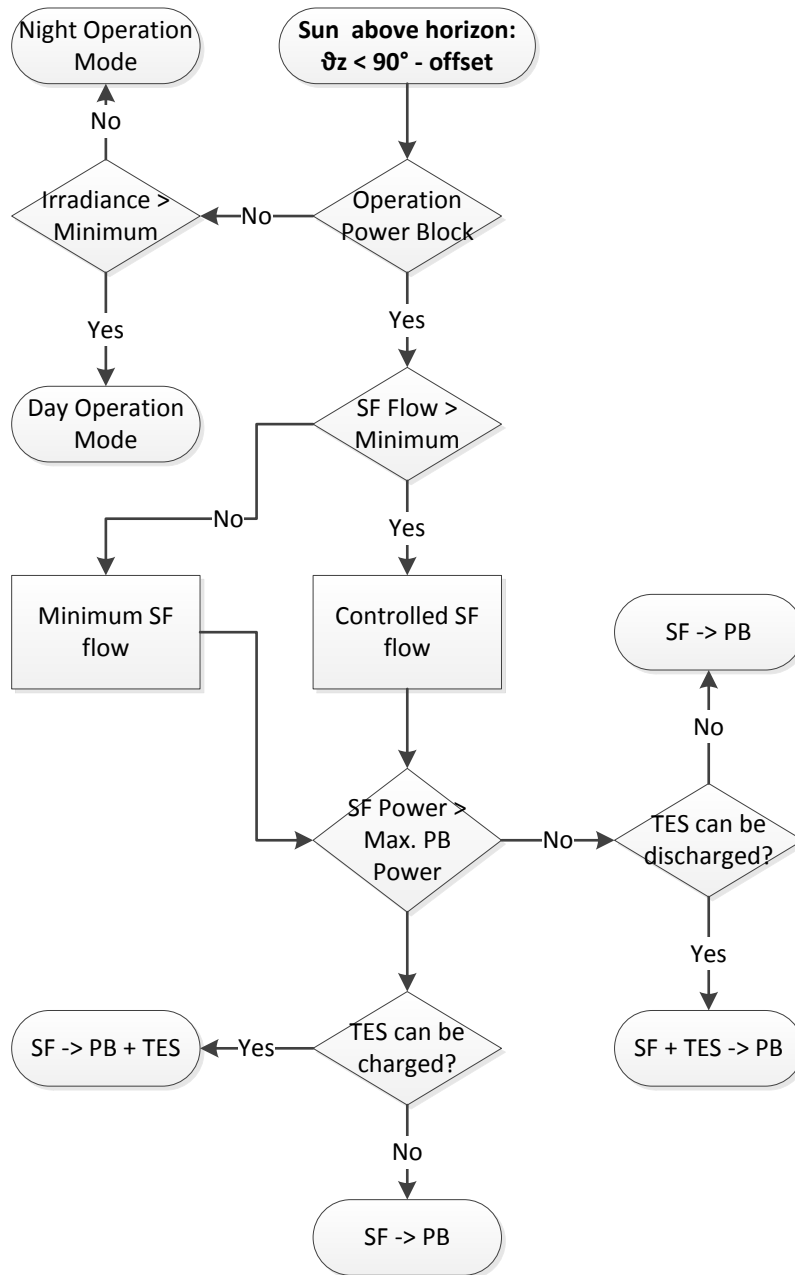


Figure 41: Operating strategy for the annual simulations

The illustrated operating strategy is equal to an “increase full-load hour” operating strategy, whenever possible the system is operated at full load.

4.4 Result

The optimization results for all configurations shown in Table 14 are shown following diagrams. Figures 42-50 show the relative LCOEs at different storage sizes and SM for each technology configuration, the average LCOE in each configuration is taken as reference.

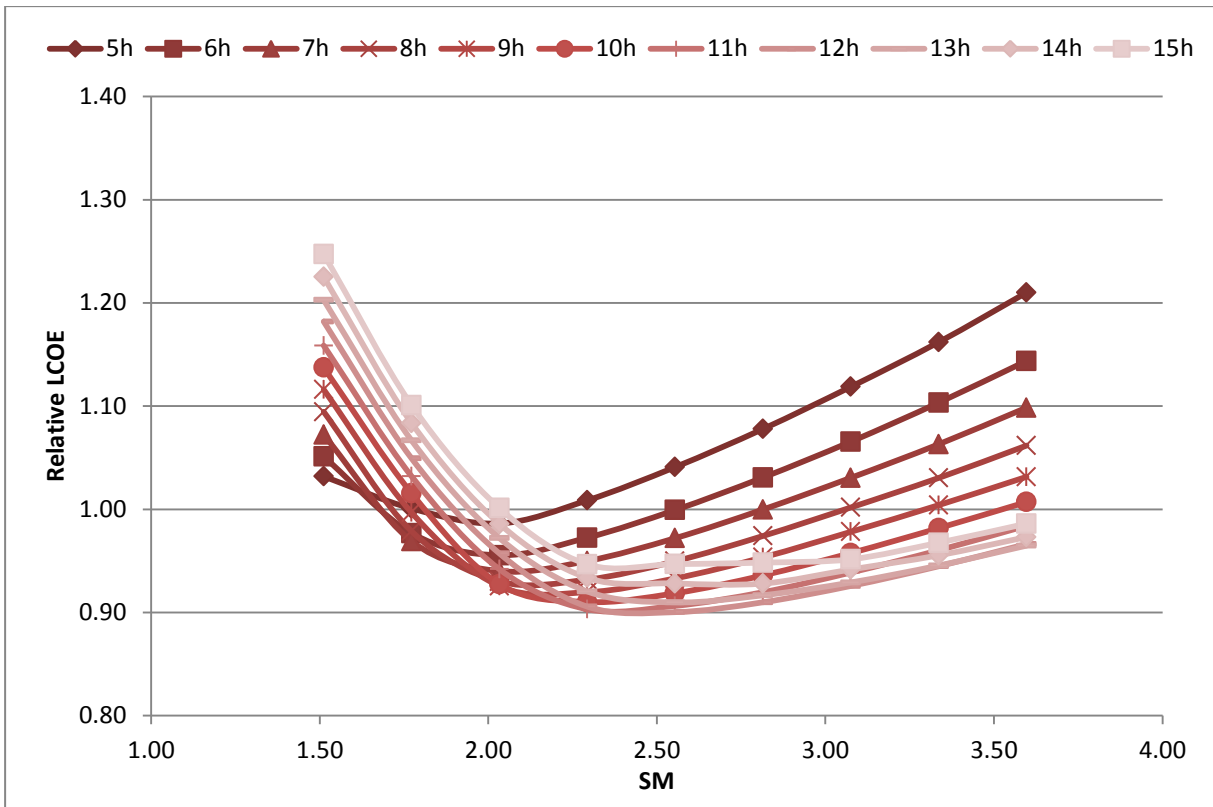


Figure 42: Relative LCOE for reference system PTC-NS-VP1-TTID at different storage sizes and SM

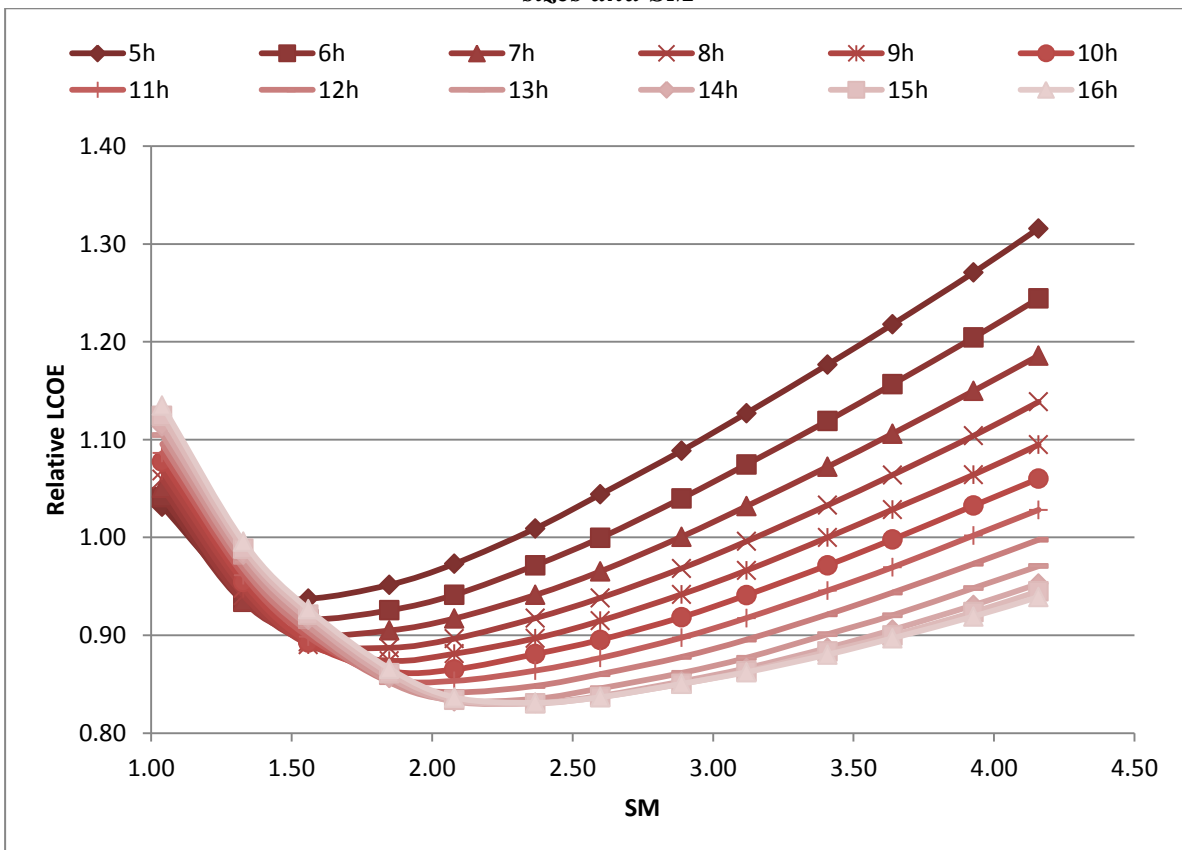


Figure 43: Relative LCOE for configuration PTC+NS+SS+TTD at different storage sizes and SM

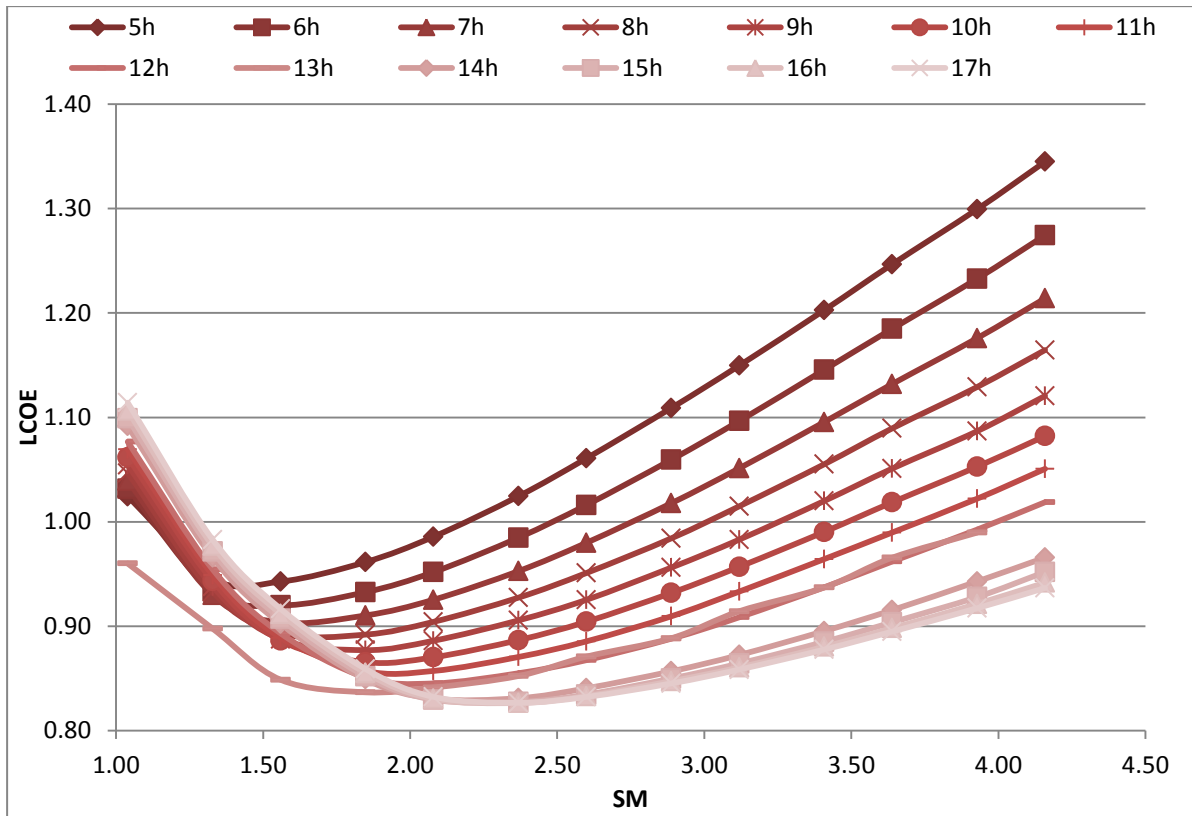


Figure 44: Relative LCOE for configuration PTC+NS+SS+STD at different storage sizes and SM

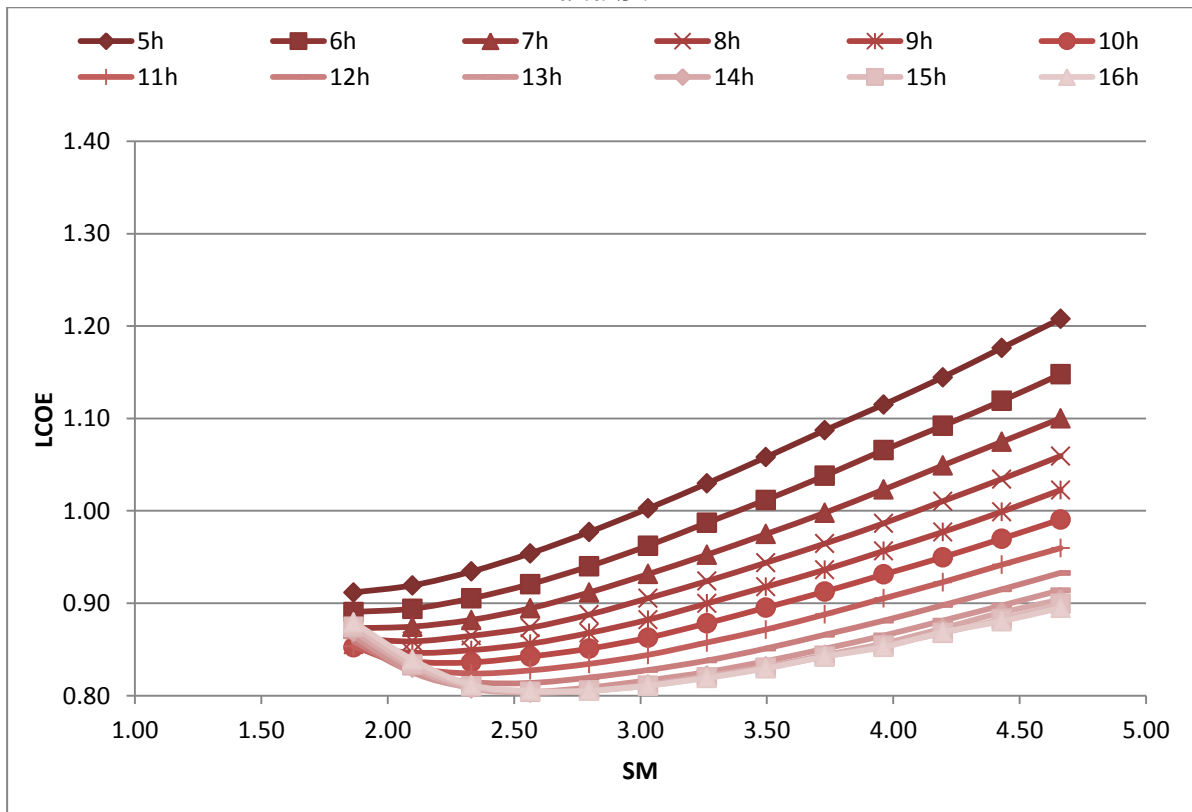


Figure 45: Relative LCOE for configuration LFC+NS+SS+TTD at different storage sizes and SM

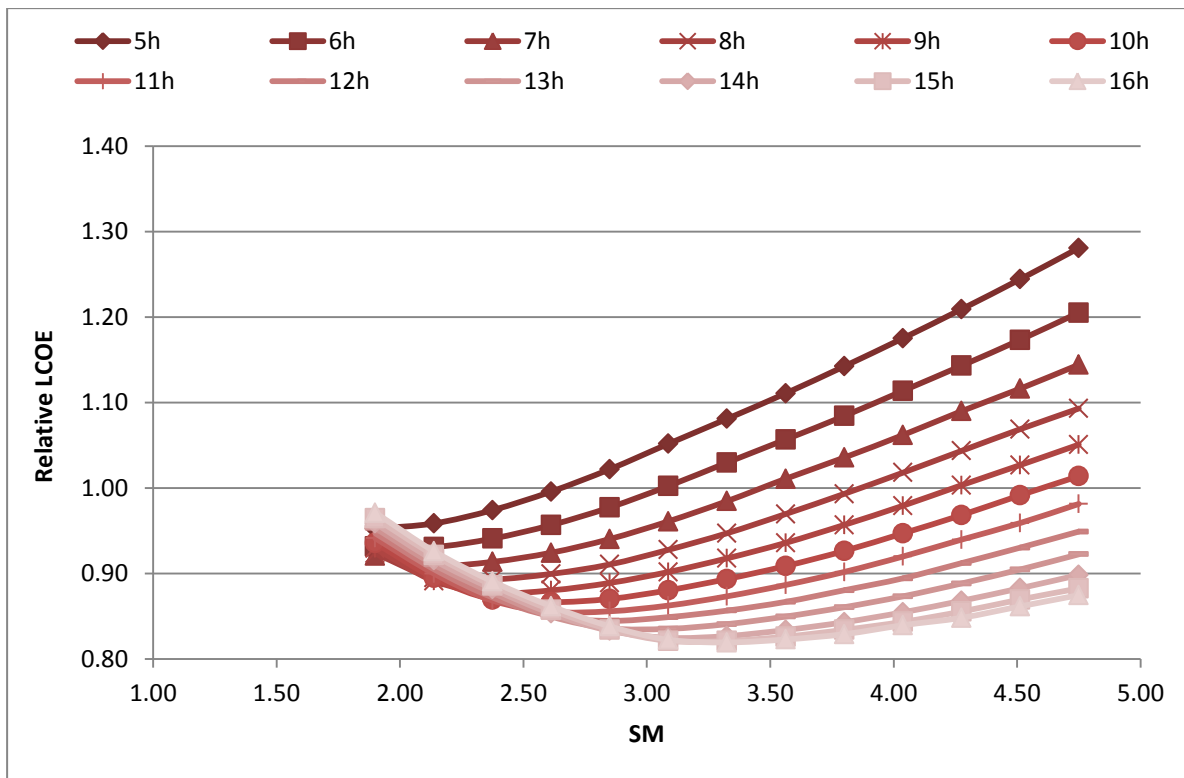


Figure 46: Relative LCOE for configuration LFC+EW+SS+TTD at different storage sizes and SM

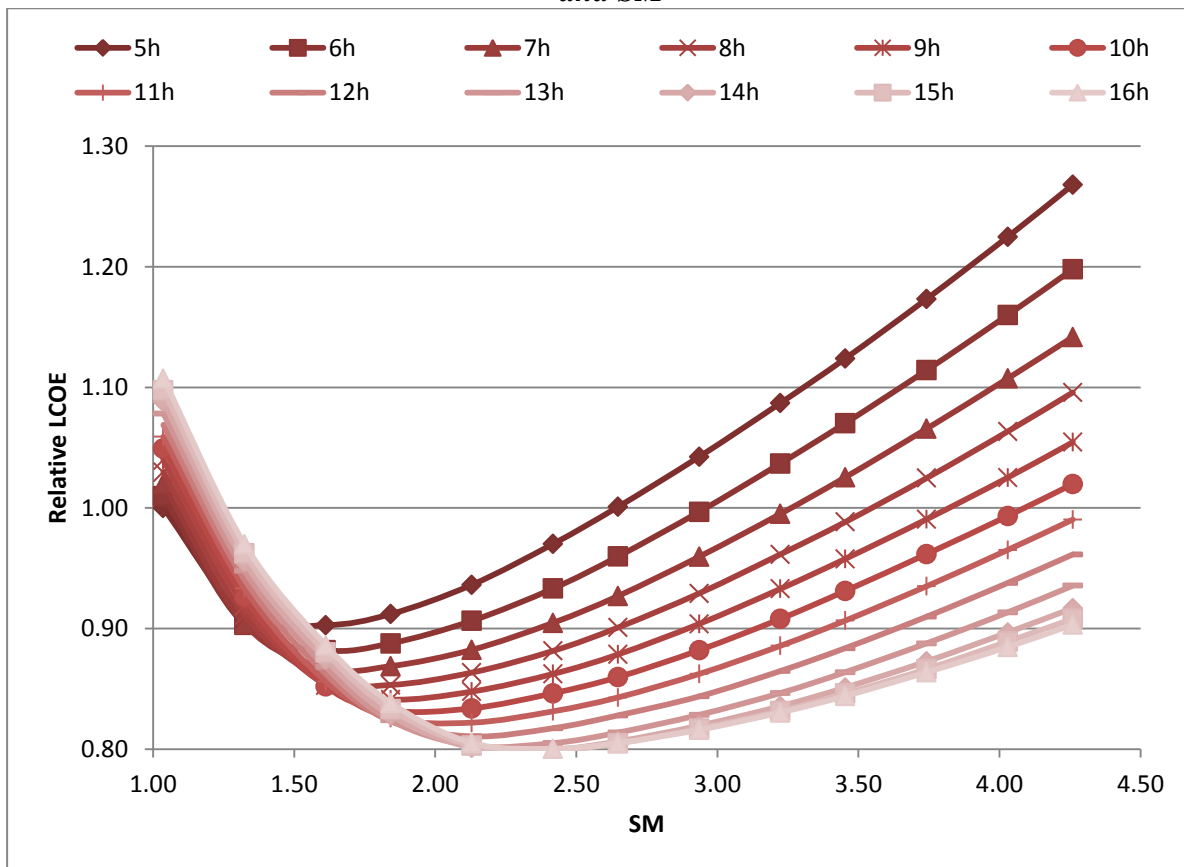


Figure 47: Relative LCOE for configuration PTC+NS+Hitec+TTD at different storage sizes and SM

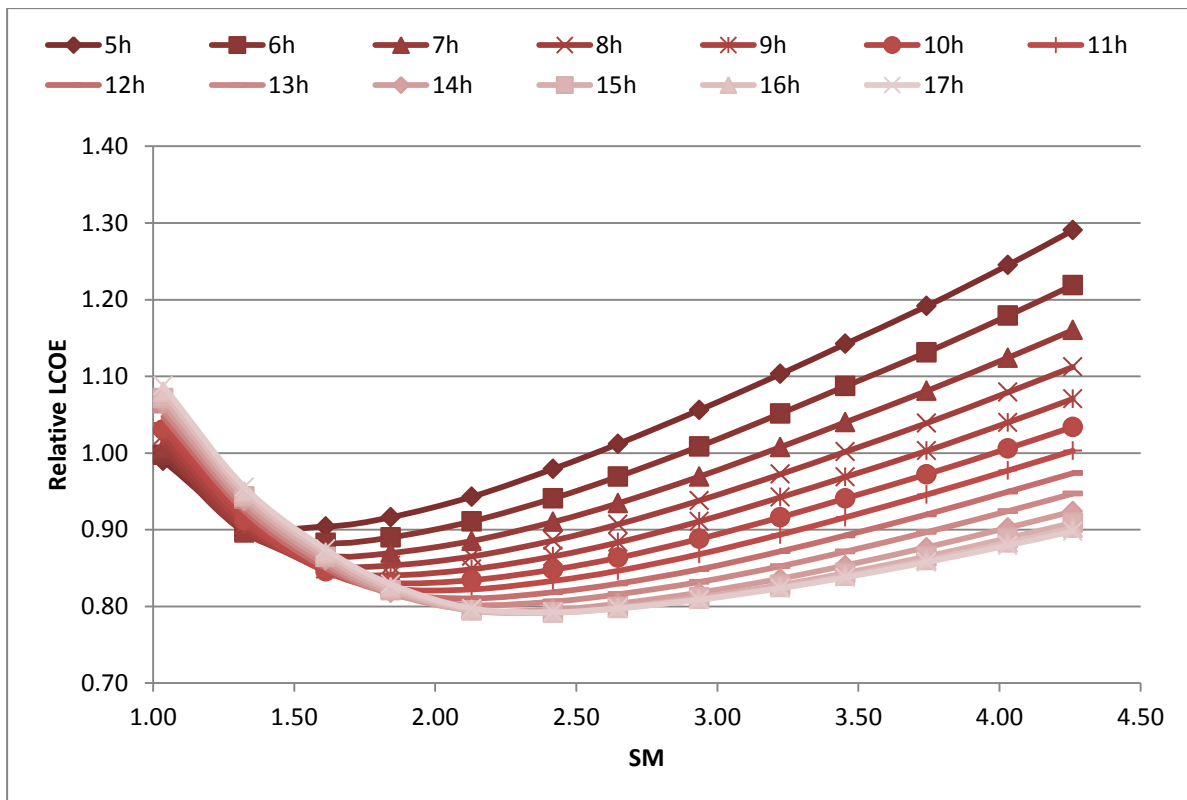


Figure 48: Relative LCOE for configuration PTC-NS-Hitec-STD at different storage sizes and SM

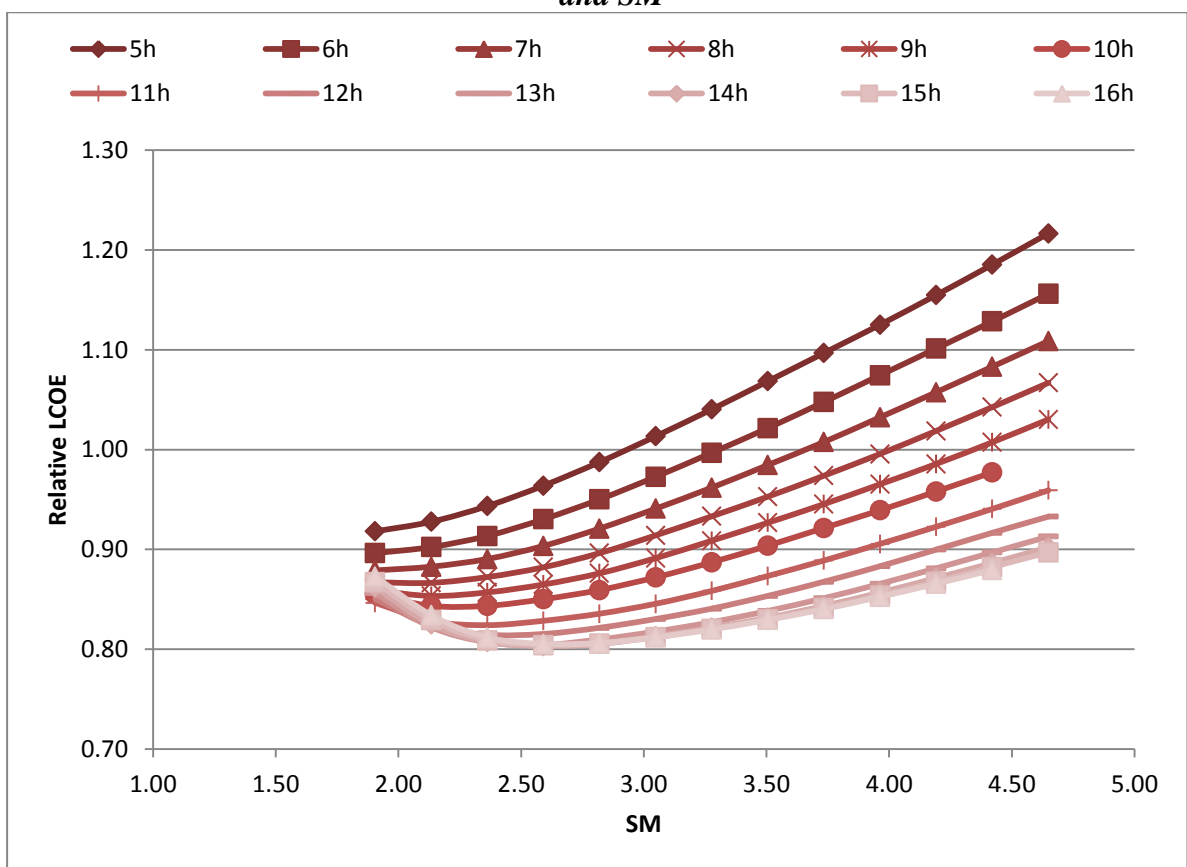


Figure 49: Relative LCOE for configuration LFC-NS-Hitec-TTD at different storage sizes and SM

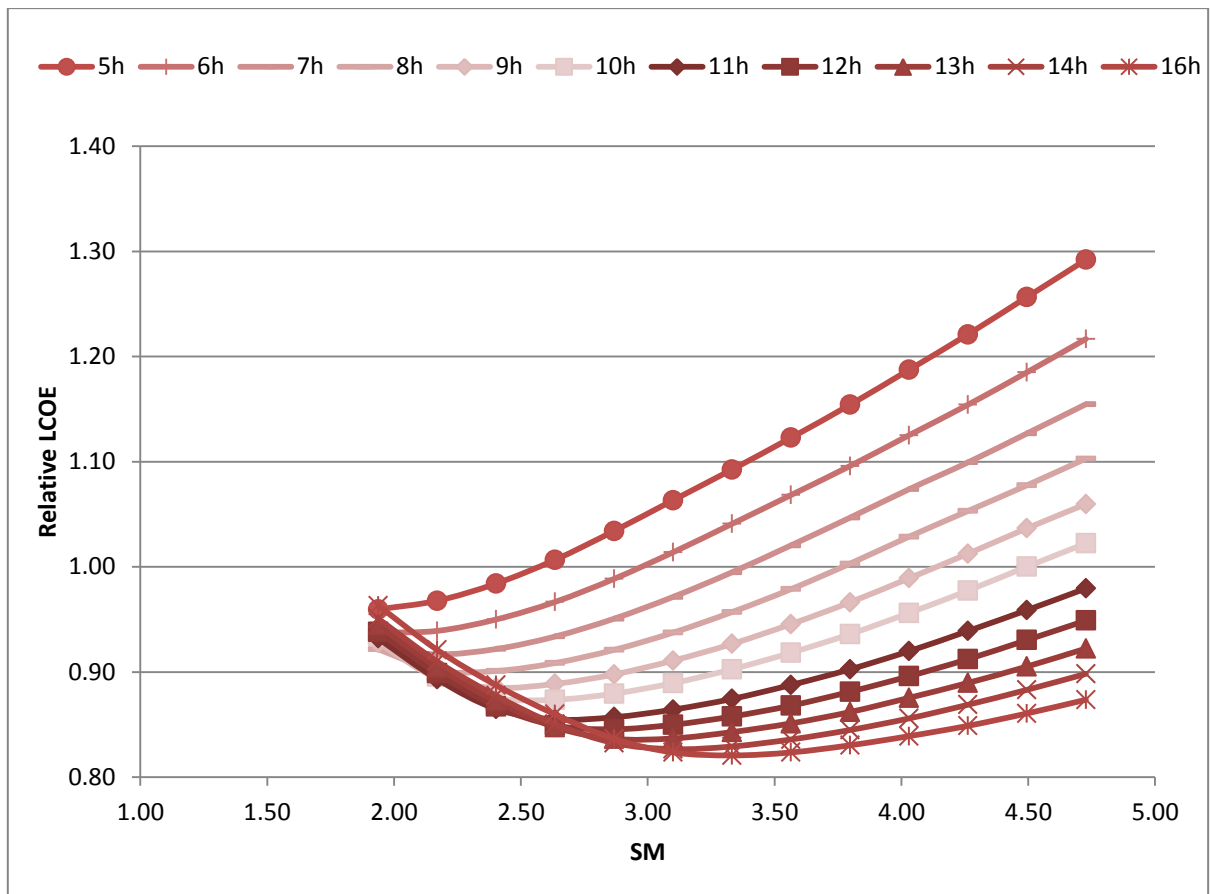


Figure 50: Relative LCOE for configuration LFC-EW-Hitec-TTD at different storage sizes and SM

An overview of the optima for all configurations is shown in Table 14.

Table 14: Plant configurations for which the lowest LCOE have been obtained^{††}

Configuration	Relative LCOE	TES Size, h	Loops, -	SM, -	CF, %
PTC-NS-VP1-TTID	1.000	12	196	2.55	44.27
PTC-NS-SS-TTD	0.922	15	82	2.37	45.11
PTC-NS-SS-STD	0.918	16	82	2.37	45.10
LFC-NS-SS-TTD	0.892	14	66	2.56	46.02
LFC-EW-SS-TTD	0.910	16	84	3.32	53.34
PTC-NS-Hitec-TTD	0.887	15	84	2.42	45.53
PTC-NS-Hitec-STD	0.880	16	84	2.42	45.82
LFC-NS-Hitec-TTD	0.892	14	68	2.59	46.17
LFC-EW-Hitec-TTD	0.912	16	86	3.33	53.14

The lowest LCOE has been obtained for the single-tank storage system using Hitec as HTF, however, one has to keep in mind that the difference between the lowest and highest LCOE for a direct system and thus definitely within the uncertainty of the simulations and the previously cost assumptions. The highest value in Table 14 has been obtained for the indirect

^{††} Reference case (PTC-NS-VP1-TTID, 12h storage) cost is set as 1

system using PTC technology and VP1 as HTF. It can also be observed that the storage size for this configuration is rather low compared to the direct system. The low cost assumptions for the direct storage system lead to relatively high storage capacity for cost-optimized configuration. The most significant highlight in Table 14 is that the LFC configurations with E-W orientation have obtained considerably higher capacity factors for the optimum and also high solar multiple which may be also caused by the relatively low invest cost for LFC technology as shown before.

The storage utilization will be highlighted for another case scenario. All the configurations with 12 h TES capacity and the SF size which led to the lowest LCOE have been analyzed and are shown in Table 15.

Table 15: Configurations with 12 h storage which have led to the lowest LCOE^{‡‡}

Configurations	Relative LCOE	Loops, -	SM, -	CF, %
PTC-NS-VP1-TTID	1.000	196	2.55	44.27
PTC-NS-SS-TTD	0.935	72	2.08	40.22
PTC-NS-SS-STD	0.939	72	2.08	39.62
LFC-NS-SS-TTD	0.904	66	2.56	44.86
LFC-EW-SS-TTD	0.938	72	2.85	45.45
PTC-NS-Hitec-TTD	0.901	74	2.13	40.66
PTC-NS-Hitec-STD	0.900	74	2.13	40.29
LFC-NS-Hitec-TTD	0.905	62	2.36	42.31
LFC-EW-Hitec-TTD	0.939	74	2.87	45.40

The lowest LCOE was again achieved for the single-tank storage system with Hitec as HTF. The highest capacity factors have been obtained for the LFC plants with E-W orientation. However, the CF difference to the PTC configuration is very low as it is also for the maximum and minimum value.

Another distinction is the difference in solar field size for which is optimum has been obtained. It can be seen that the loop number in the VP1 HTF systems is much larger than for the other configuration using PTC technology keeping in mind that 1 loop with VP1 is only half the length of the ones operated with molten salt. The 196 short loops are equivalent to 98 long loops. The other PTC configurations have 72 or 74 loops.

The impact on the storage is shown in

^{‡‡} Reference case (PTC-NS-VP1-TTID) cost is set as 1

Table 16 and Figure 42 where the daily maximum storage level is shown throughout the year.

Table 16 gives an overview of the average values which have been obtained for the daily maximum storage level, its standard deviation as well as the number of days for which a storage level above 0.97 or 0.5, respectively, has been obtained.

Table 16: Utilization numbers of the storage system for the configurations

	Max. SOC ^{§§} average, -	Max. SOC deviation, -	SOC > 0.97, days	SOC > 0.5, days
PTC-NS-VP1-TTID	0.54	0.35	97	177
PTC-NS-SS-TTD	0.43	0.35	64	133
PTC-NS-SS-STD	0.52	0.30	67	156
LFC-NS-SS-TTD	0.47	0.35	83	150
LFC-EW-SS-TTD	0.53	0.34	80	186
PTC-NS-Hitec-TTD	0.44	0.35	71	138
PTC-NS-Hitec-STD	0.52	0.30	74	161
LFC-NS-Hitec-TTD	0.44	0.34	65	136
LFC-EW-Hitec-TTD	0.54	0.34	84	188

It can be seen in

^{§§} SOC: state of charge in the storage system

Table 16 that the deviation in the storage level is rather similar, the exception are the single-tank systems. The similarity can also be seen in *Figure 51*. The average maximum storage level is between 0.43 and 0.54. This relatively low storage utilization is caused by the fact that such large capacity TES systems only performance well on days of good irradiation. The peak utilization is the best for the system with VP1 due to its large solar field size. The most number of days where the maximum storage level is above 50% of its design value, is obtained by the systems with E-W orientation. Its reduced seasonal fluctuation in daily solar field energy production leads to a better storage utilization.

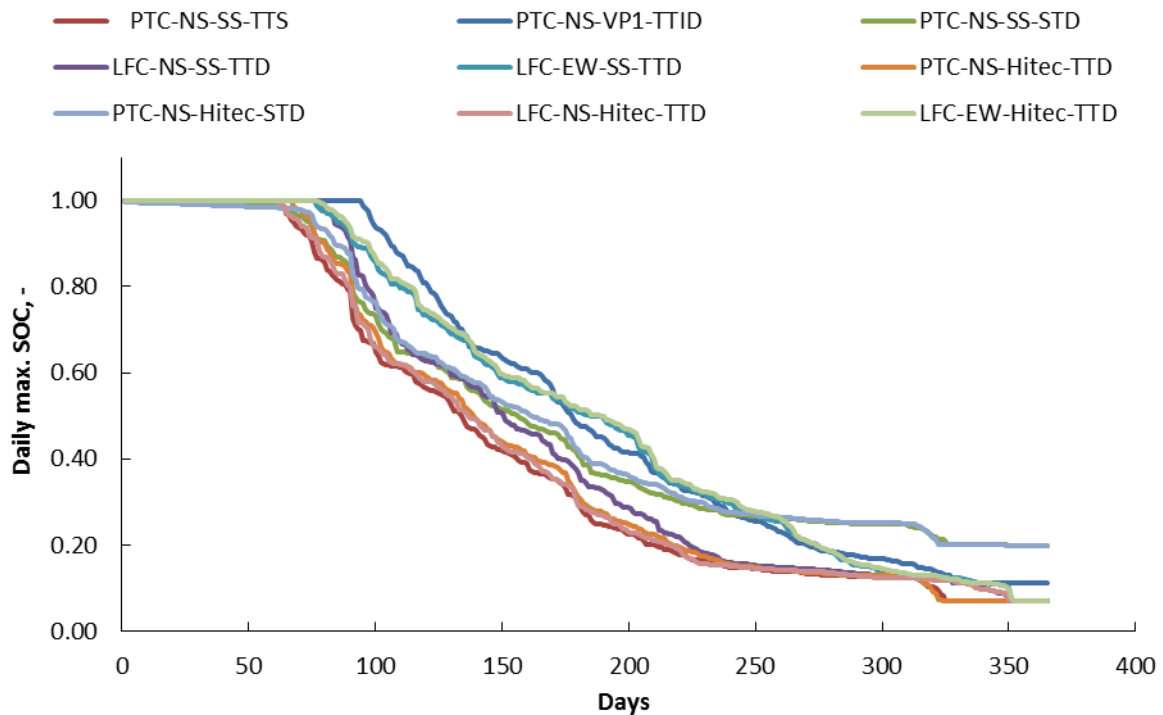


Figure 51: Max. SOC level throughout the year

It can be seen that the two single-tank systems have a relatively high minimum storage level of > 0.2 SOC, as storage discharge stops when the upper temperature in the storage is too low for steam generation even though the storage is theoretically not completely discharged.

4.5 Conclusion

The report gives an overview of the state-of-the-art technology options for CSP collectors, solar field layout, heat transfer fluid, heat storage media and storage methods. In total, 9 different combinations are analyzed, out of which the case below is regarded as reference case.

Table 17: Reference case

No.	Collector	Orientation	HTF	TES	HSM
1	PTC	N-S	VP1 (thermal oil)	Two-tank	Solarsalt

With the state-of-the-art working parameters and plant system designs, corresponding simulations were carried out for these 9 cases. Under the operating strategy of “increase full-load hour”, plant performances were obtained. The results together with plant costs were used as inputs for plant optimization towards the lowest LCOE.

The lowest LCOE has been obtained for the single-tank storage system using Hitec as HTF, however, one has to keep in mind that the difference between the lowest and highest LCOE for a direct system is below 1 €-cent and thus within the uncertainty of the simulations and cost assumptions.

Additional analyses were carried out considering systems of 12 h storage capacity, particularly on the LCOE and SOC. The lowest LCOE was again achieved for the single-tank storage system with Hitec as HTF again.

Regarding to the storage system performance, the peak utilization is the best for the system with VP1 due to its larger solar field size. Generally the deviation in the storage level for all configurations is similar, the exception are the single-tank systems which are smaller. The systems with E-W orientation gain the most number of days when the maximum storage level is above 50% of its design value, which is mainly thanks to its reduced seasonal fluctuation in the daily solar field energy production.

5. Influence of heat source location on the efficiency of small molten salts based storage for steam generation with direct immersed helical coil at steady-state (CyI)

5.1 Description of the systems

The Cyprus Institute set up a small thermal storage tank (TESLAB, Figure 52) used as test-bench for steam generation. The present section details the main steady-state results of simulation with TRNSYS based on such facility. The model has been defined according to experiments previously performed on the bench [36]. The thermal storage tank includes two cylindrical electric heaters of 9kW capacity each located on the bottom of the tank, a superheater with helical coil shape in Stainless steel AISI 316L directly immersed in molten salts.



Figure 52. TESLAB tank (left) and drawing of the helical coil (right)

The model of simulation has been developed in TRNSYS and Simulation Studio with type 155 which permits to compute directly immersed heat-exchangers with helical shape (Figure 53). It simulates the superheater (yellow coil in Figure 52) in the static molten salts mixture (layer of salts is in purple). Composition of the salts is detailed in Table 18. Use of type 155 is further described in the STAGE deliverable 7.14.

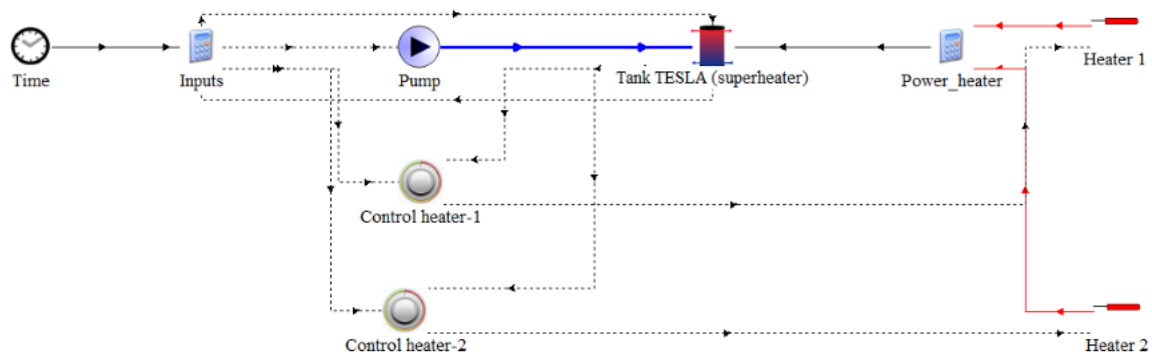


Figure 53. Simulation Studio template of TESLAB facility

Table 18. Molten salts mixture at TESLAB

Property	Value	Unit
Global mass of the salts	2161.5	kg
Mass of KNO ₃	864.8	kg
Mass of NaNO ₃	1296.7	kg
Volume of the salts	1.14	m ³

The thermal heat loss coefficient on the top and edge losses coefficient is $0.31\text{W.m}^{-2}.\text{K}^{-1}$. The bottom losses are $0.70\text{W.m}^{-2}.\text{K}^{-1}$. Steam enters into the helical coil with a flow rate of 22.46kg.hr^{-1} at 176°C with a noise:

- of 10°C of amplitude,
- with a period of 5 minutes,
- an average of 0°C .

The tank has been divided in 15 isometric nodes for the simulation. The coil is immersed from top node 1 to node 5 (Table 19). The simulation compares the performance of the facility with heaters located in the bottom (nodes 13 and 14) of the tank and heaters located closer to the heat exchanger with steam (nodes 6 and 7).

Table 19. Position of the nodes of the coil in the tank

Node of the coil	Height	Node of the tank
1	1.12m to 1.20m	1
2	1.04m to 1.12m	2
3	0.96m to 1.04m	3
4	0.88m to 0.96m	4
5	0.80m to 0.88m	5

Although heat-exchange occurs during 24 hours, heaters are activated from 8:00AM to 6:00PM reflect possible operations schedule of solar plant. In such scenario, heat source would be provided by HTF. The temperature is regulated with a thermostat or hysteresis function on both heaters. The top temperature corresponding to node 1 is the reference temperature to be monitored. The first heater (“Heater_1”) is activated if:

- the temperature of node 1 is below $550^\circ\text{C}-20^\circ\text{C}$ (half of the deadband), i.e. 530°C ,
- at previous time-step, the heater was activated and the temperature of the molten salts is below $550^\circ\text{C}+20^\circ\text{C}$, i.e. 570°C (maximum allowable temperature not to degrade the molten salts).

The second heater (“Heater_2”) is activated if:

- the temperature of node 1 is below $490^{\circ}\text{C}-40^{\circ}\text{C}$, i.e. 470°C ,
- at previous time-step, the heater was activated and the temperature of the molten salts is below $490^{\circ}\text{C}+40^{\circ}\text{C}$, i.e. 530°C .

5.2 Simulation results

5.2.1 Comparison with different location

Simulation results correspond to the steady state regime. Figure 54 presents the repetitive 48hours pattern of the steam outlet temperatures: in blue the configuration with heaters in the “bottom” and in red with heaters below the coil (“top”). By night, relying on thermal storage, the temperature of the outlet of the steam is higher with the heaters on the bottom. But as soon as the heaters are activated in the morning at 8:00 AM, the outlet temperature of the steam increases faster with the top configuration. Within the night the outlet temperature of the steam gets lower than the “bottom” configuration. Nonetheless according to Figure 55, duty cycle of heating varies from one configuration to another one. In the bottom configuration, only one heater is working during a day (9 kW) and the day after the two heaters are working together for some hours (18kW) and then only one heater is working. In the top configuration, same cycle is repeated each day. The two heaters are activated at the beginning of the day (18 kW) and then one stops. This explains the raise of temperature which is faster for the steam outlet with the configuration top as described before. The average energy delivered to the molten salts by the heaters are 110.84kWh with the heaters in the bottom and 112.51kWh with the other configuration. Eventually the energy delivered is very close (less than 1.5% of difference) but the heat transferred to the steam is 95.53kWh (bottom) and 99.69kWh (top). In the first case the efficiency is so 86.2% and 88.6% so leading to a slight improvement of 2.4%. Thermal losses are 14.39kWh and 12.84kWh in respective cases. But thermal cycling of the helical coil is bigger with the heaters close to the heat-exchanger. Indeed steam temperatures vary more with the most efficient configuration from 406°C to 568°C for an absolute difference of 162°C . Instead the difference is only 119°C from 420°C to 539°C for the heaters located in the lower part.

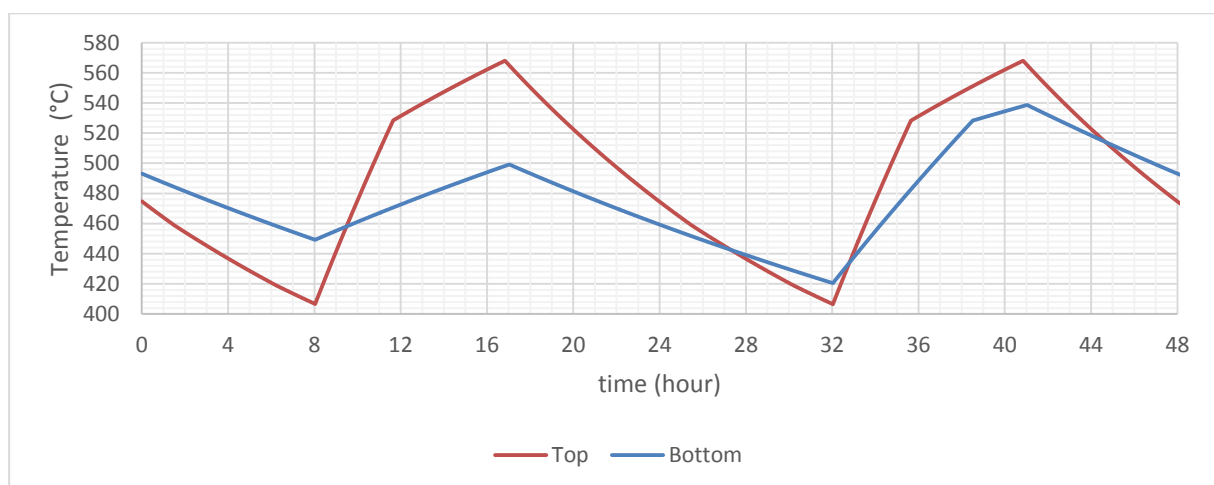


Figure 54. Comparison of the outlet steam temperatures (with different locations of the heaters)

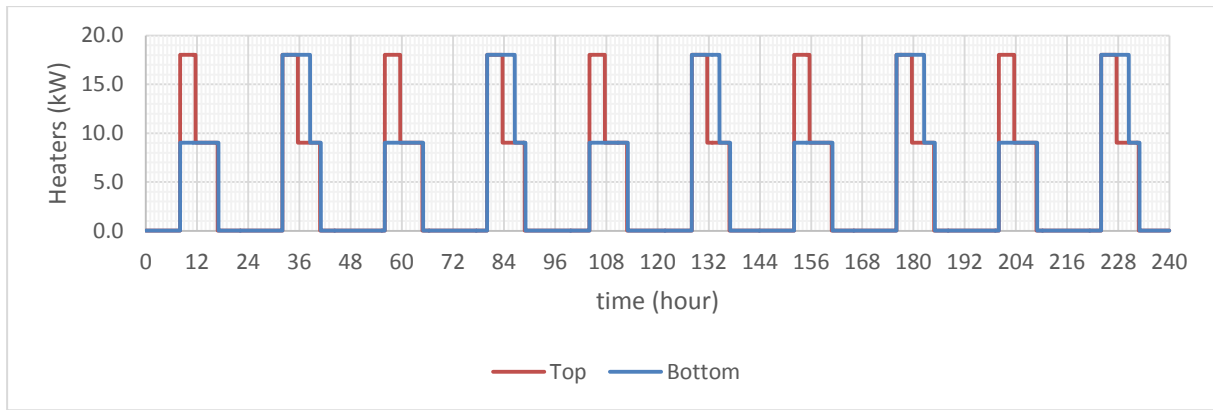


Figure 55. Duty cycle of the heaters

Looking more specifically into the temperatures of the molten salts, the distribution is different. On one hand, as shown in Figure 56, the temperature evolution is similar between the layers when the heaters are in the bottom. Node 15, lowest one, is the coldest node and oscillates less temperature wise. Globally the tank temperature remains above 400°C, but cycling affects all the nodes except the lowest one (119°C), independently to the proximity to the coil.

On the other hand, as shown in Figure 57, cycling affects less layers with the top configuration. Temperatures of layers 11 to 15 are stable and perfectly stratified between 258°C and 368°C. Temperatures of nodes 8, 9 and 10 are still stratified but cycling occurs up to 74°C for node 8. Upper layers then are hotter but thermal cycling is more consequent (169°C). With heaters lower, temperatures of the 14 upper layers oscillate less (121°C).

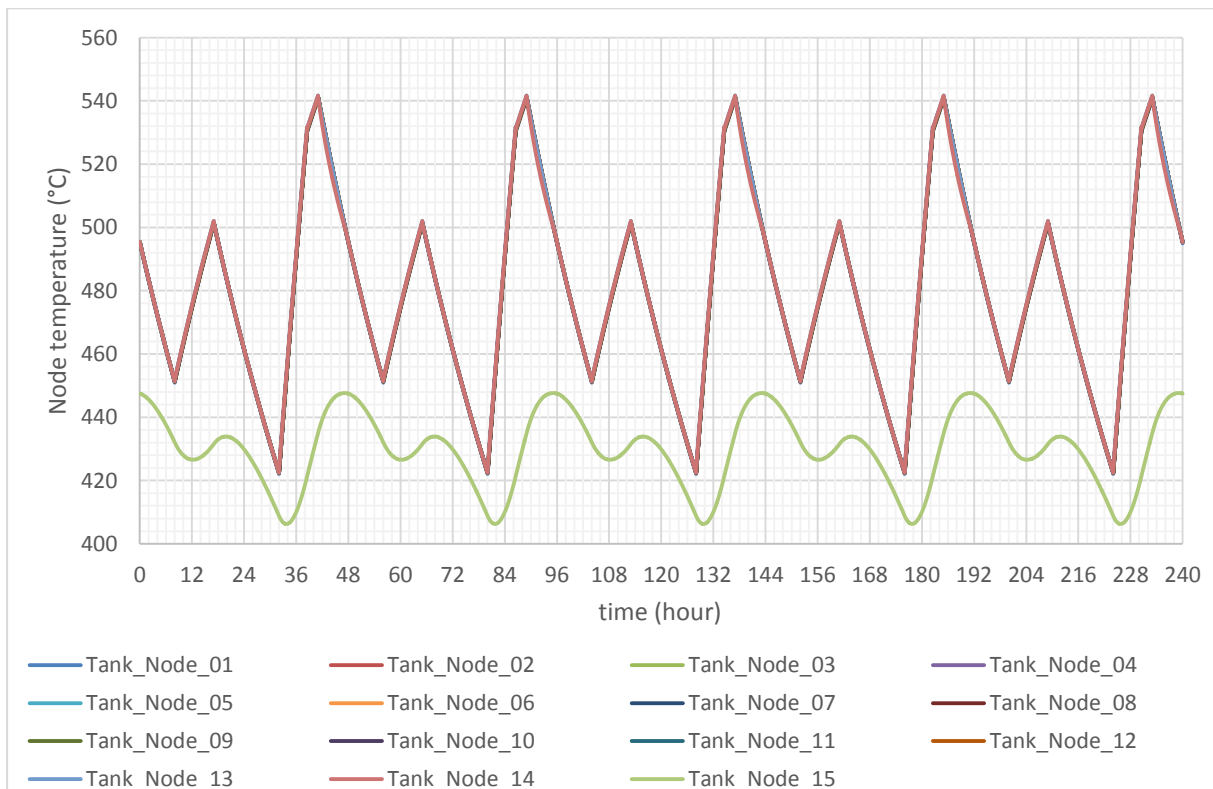


Figure 56. Nodal temperature with bottom configuration

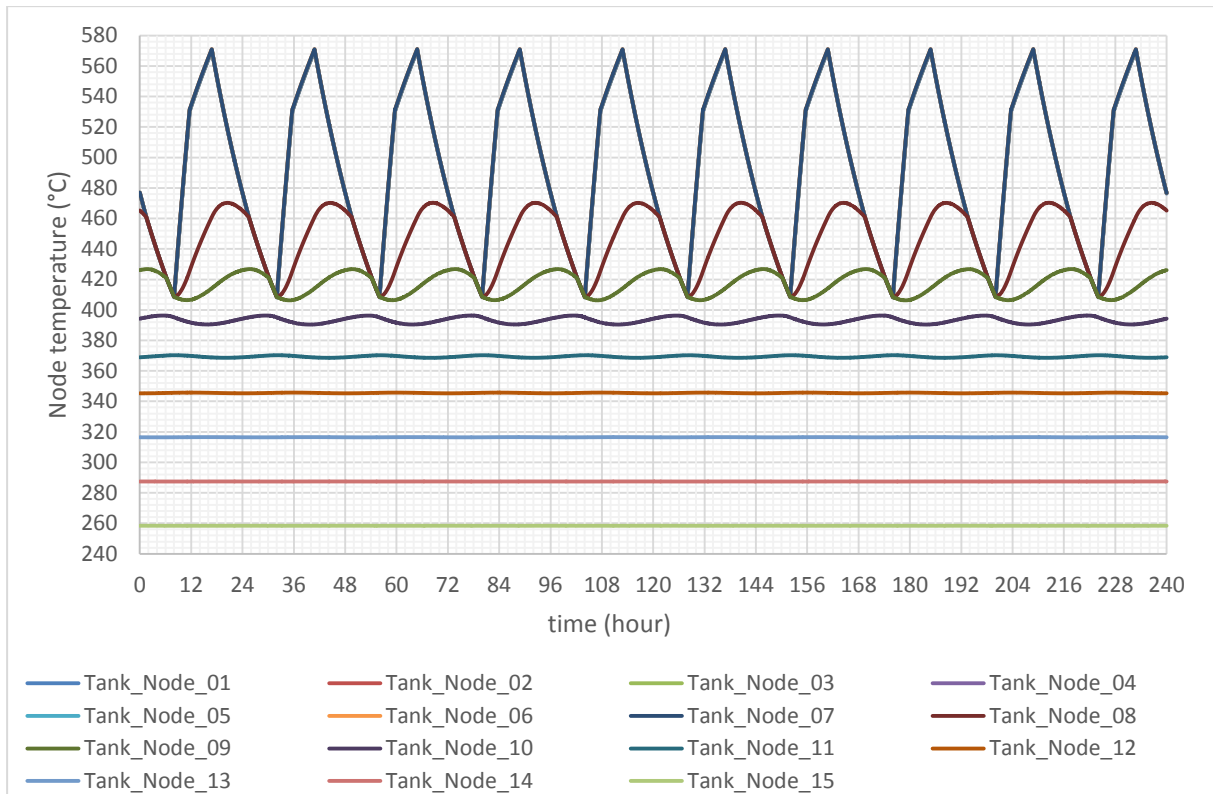


Figure 57. Nodal temperatures with top configuration

These considerations are correlated to the behaviour of steam temperature with higher cycling with heaters on the top. With the heaters close to the heat-exchanger, temperatures of lower layers are close to the freezing point of the salts which is 238°C. Next paragraph evaluates the solution of a smaller tank with heaters below the heat-exchanger.

5.2.2 Comparison with a smaller tank

Since the temperatures of the layers 11 to 15 are stable and low independently to the duty cycle of the heaters and the operation of the steam loop, a shorter tank is analyzed with 10 layers instead of 15 layers. The height of the tank is reduced to 0.8m (instead of 1.2m) and volume of the salts to 0.76m³. Heaters are located at layers 6 and 7 in both cases. Based on simulation, Figure 58 shows that eventually the outlet temperature of the steam is similar. So removing salt layers leads to the same output power:

- 99.81 kWh daily average energy with the reduced tank,
- 99.69 kWh daily average energy with the initial bigger tank.

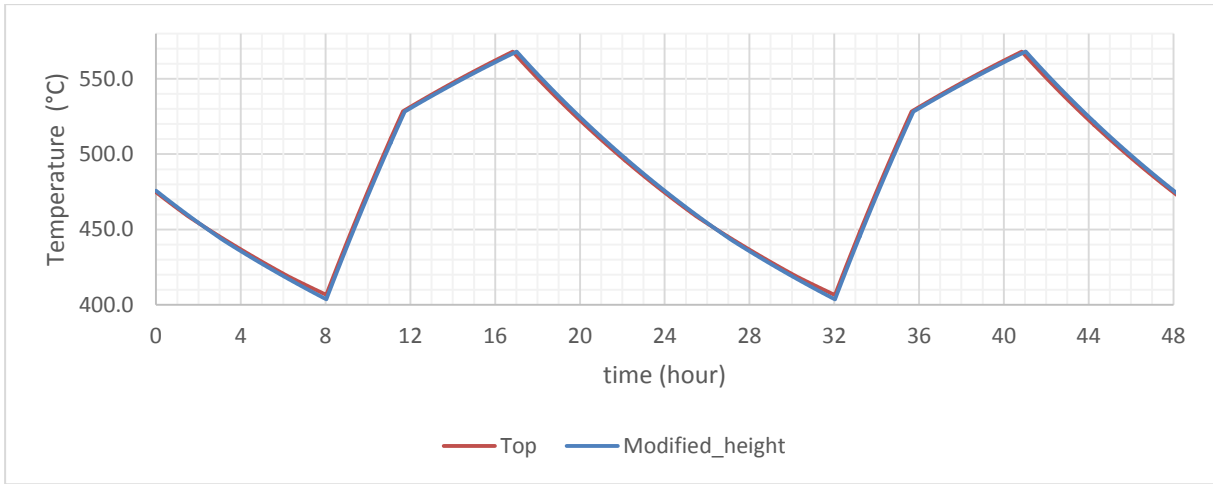


Figure 58. Comparison of the outlet steam temperatures (with reduced tank)

With the reduced tank the temperatures are much higher than the freezing point of molten salts as it can be seen in Figure 59. The final efficiency of the tank heat-exchange is 87.4% with reduced tank instead of 88.6%.

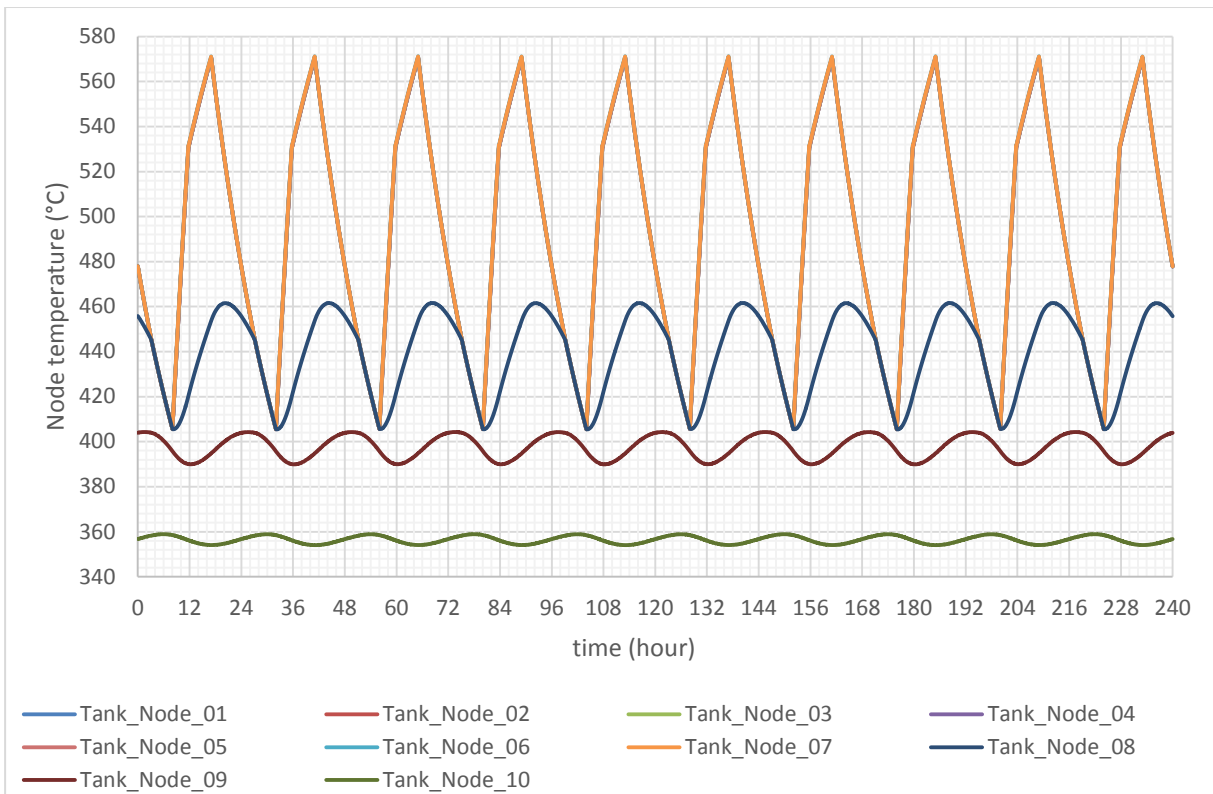


Figure 59. Nodal temperatures with reduced tank

Table 20. Performance of the tanks

Type of configuration	Tank with heaters on the bottom	Tank with heaters below the heat-exchanger	Modified tank
Layers of the heater	13-14	6-7	6-7
Daily energy	95.53 kWh	99.69 kWh	99.81 kWh
Heat transfer efficiency	86.2%	88.6%	87.4%
Thermal cycling of steam	118°C	162°C	164°C

5.3 Conclusion

The simulation with TRNSYS approach permitted to compare the importance of the location of the heat source in a small molten salt storage like in TESLAB (1.14m³). Table 20 summarizes the results of the three configurations. Even with similar heat input, installing the heat source close to the helical coil ensures a better efficiency, 88.6% instead of 86.2%, reducing the thermal losses and improving the heat transfer rate. But simulation also shows that cycling of the steam outlet temperature is higher with such solution affecting the end use. Also, capacity of superheating decreases faster when relying on overnight storage. The Cyprus Institute configured the tank with heaters on the bottom with a conservative approach in order to avoid freezing that may occur if heaters are closer to the coil. To avoid this, it is possible to reduce the height of the tank and locate the heaters close to the heat-exchanger. Eventually raw materials will be less costly (stainless steel and molten salts).

6. Design of a Fresnel Concentrator Type Collector (Uni Evora)

In solar thermal concentrator technology, larger concentration values bring lower thermal losses per unit aperture area. This will result in higher collector efficiency at higher operating temperatures and, in turn, higher thermodynamic conversion efficiency from heat to electricity.

A possible approach is to use Linear Fresnel Reflector (LFR) concentrators which are renowned for their potential cost-effectiveness. In fact, conventional LFR technology has been developing at a slower pace than other technologies like those based PT (Parabolic Trough). Many reasons can be given for this fact, not the least relevant being the fact that the bankability of PT technology has been much more significant, thus leading towards a (initial) stronger expansion. The large experience available via SEGS plants which were built in California, USA, gave experience and confidence to the CSP investors, banks and promoters that relied on PT technology using thermal oil being in operation since the mid 80's.

Due to the low-profile reflector architecture and consequently reduced wind loads, the use of flat mirrors, fixed receivers and other characteristics, LFR has a good potential for a substantially lower cost per sqm of installed concentrator (when compared with that of PT concentrators) but, at present, on the market, a substantially lower yearly efficiency, induced by the additional transversal cosine losses and the typically focusing type optic kind of configuration, very far from the limits allowed by non-imaging optics, with flawed etendue matching and non-optimized second stage optics (when it exists).

Table 21: Comparison of ground area for Fresnel and PTC commercial solutions for the same mirror area.

	Ground Area per MWe (ha/MW)	Ground Area for 50MWe (ha)
Fresnel	1.2	60
PTC	2	100

Recently, proposals for Advanced LFR solutions were presented taking advantage from non-imaging optics configurations [37, 38], as shown in Figure 60 and Figure 61.

These configurations are designed to have higher concentration factors than conventional LFR solutions (> 45X). For the purpose of this deliverable a summary of an Asymmetric LFR concentrator (ALFR), developed by UEVORA, will be presented.

The main characteristics of this concentrator are [38]:

- A dual receiver configuration but with the receivers placed on a single tower;
- An dual asymmetric macro-focal Compound Elliptical Concentrator solution for the second stage;
- A flat etendue matching curve for the primary to be closer to conventional practice in LFR collectors;
- A second stage configuration involving a V-groove section in order to eliminate gap losses

The final configuration can be seen in Figure 60 and Figure 61.

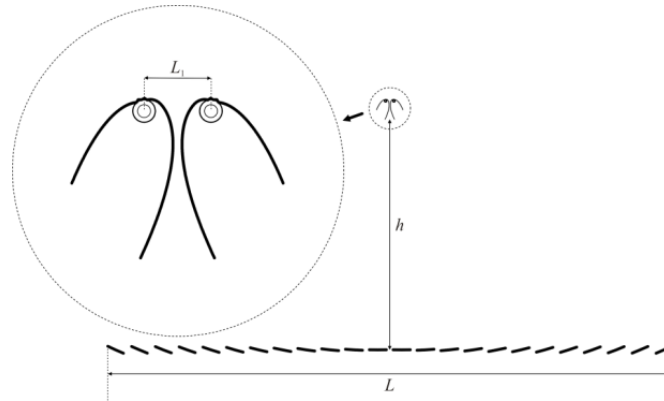


Figure 60: Proposed cross section of the ALFR (Dual asymmetric macro focal CEC Concentrator), notice the two CEC, each for its own evacuated tube and illuminated by an asymmetric primary, on the single tower.

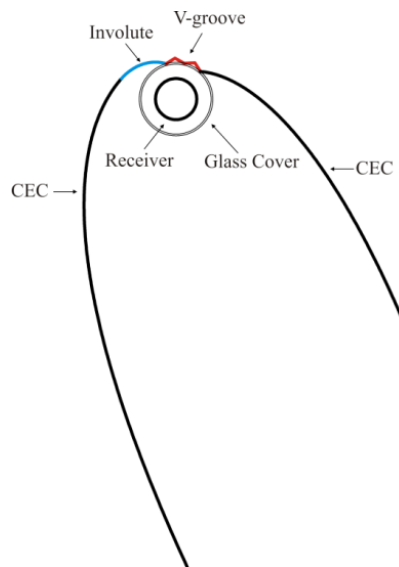


Figure 61: Detail of the second stage showing the asymmetric CEC, the involute part and the V-groove addition, for zero gap losses.

Looking in detail, the main characteristics of this concentrator are:

1. It is a compact concept because it uses two receivers, even though it places them on a single elevated structure at a height $h > 7\text{m}$ (see Figure 60).
2. In this new solution there are two asymmetric sets of primary/second stage CEC combinations, for each one of the two evacuated tubular receivers, forming a symmetrical optic whose left and right sides are mirror images of each other (see Figure 60);
3. The primary, in both cases, can be very large ($L > 20\text{ m}$, see Figure 60) thereby contributing to a substantial reduction of rows in the Linear Fresnel collector field; the primary discussed in this paper is 26m wide, formed by $\approx 1\text{m}$ width mirrors distanced from each other in a way as to minimize etendue losses;
4. The two evacuated tubular receivers can either be fed by a single pipe and merge in a single exit pipe, or can be used with all piping only at one end (the inlet), with one of the tubes as the inlet and the other as the outlet one, with a free expanding U-connection at the opposite end; both these concepts contribute to a pipe length reduction of the system pipe manifold in comparison with other configurations studied elsewhere; the proximity between the two receivers L_1 (Figure 60) enables the use of a single elevated supporting structure (tower) and the same connecting pipe hence reducing both costs and thermal losses;
5. The secondary mirror is composed by three parts: the CEC portion, the involute portion and V-grooves portion (see Figure 61). Ideally, the secondary mirror would only use the CEC and involute parts; however since an evacuated tube is used, the mirrors cannot touch the receiver due to the glass cover. Therefore, there is a gap between the secondary mirror and the receiver which, in turn, corresponds to optical losses (light that escapes through the gap without reaching the receiver). By using the V-grooves mirrors this effect eliminated or at the very least severely reduced.

Table 22 summarizes the geometrical and optical details of the concentrator and Figure 62 shows a render view of the concentrator.

Table 22: Geometric characteristics of the ALFR concentrator

	Aperture width (m)	Total mirror aperture length(m)	Receiver radius (m)	Receiver height (m)	Number of mirrors	Mirror width (m)	C_g (X)	ϕ (°)
ALFR concentrator	26	22	0.035	10.8	22	1	45	49.7 3

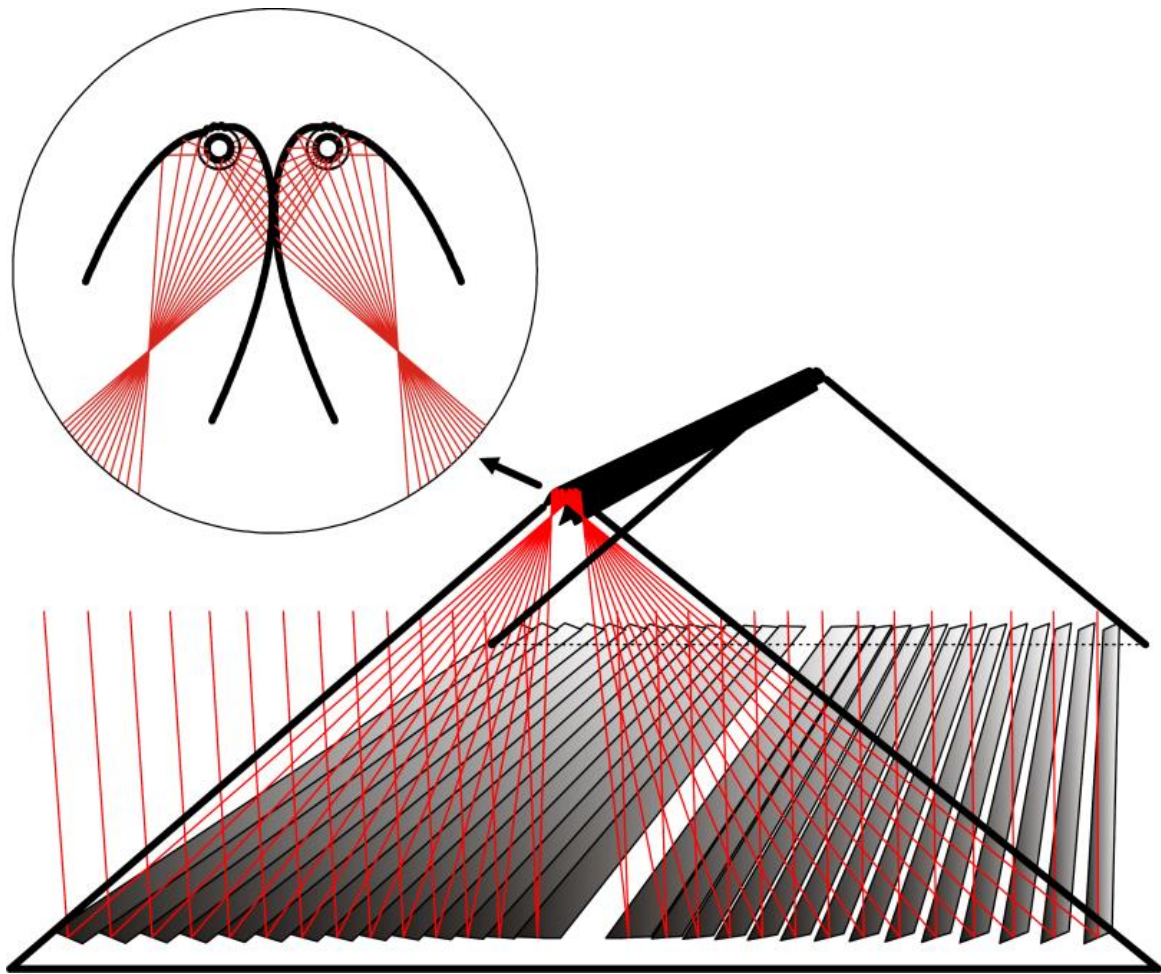


Figure 62: Render view of the ALFR solar concentrator

Using a raytracing software it was possible to estimate the overall performances of the system. Table 23 shows the optical efficiency at normal irradiance (η_{opt0}), the half-acceptance angle (θ) and the Concentration-Acceptance Product (CAP).

Table 23: Optical performance of the concentrator

	η_{opt0}	θ (°)	CAP
Dual Asymmetric CEC LFR Concentrator	0.70	0.75	0.59

Finally Table 24 shows the overall performance for two locations Hurghada (Egypt) and Faro (Portugal) for an operation with molten salts at 565°C and no storage.

Table 24: Yearly results, energy and final conversion efficiency for ALFR (corresponding to 58MWe_p at 950 W/m² DNI) concept plant collector with a total mirror area of 250 000m² (no storage)

Location	Thermal energy delivered (kWh)	Electricity produced (kWh)	Total average yearly efficiency
Faro, Portugal	2.11 x 10 ⁸	8.38 x 10 ⁷	0.147
Hurghada, Egypt	3.02 x 10 ⁸	1.22 x 10 ⁸	0.163

Regarding electricity production costs, taking into account the results from another work in which a conventional LFR concentrator with 4 hours of storage at nominal power was analyzed [37], it is expected that values below 10 eurocent/kWh can be achieved in a Southern European location like Faro and even reach 8 eurocent/kWh at lower latitudes and higher DNI radiation sites. The basic assumption for this calculation is the possibility of reaching a target cost for primary mirrors between 100 and 150 euro/m² installed. The remaining costs in the calculation performed were taken from present day conventional plants, with no attempt at optimizing, for instance, items like storage size and cost or BOP (Balance of Plant) costs concerning the reduced number of components, pipe length, fluid volume, etc., inherent to a higher concentration situation as mentioned. In short, once low cost mirrors are available (and that should happen with rising market penetration) optimized advanced LFR plants should constitute a very serious opportunity for low cost electricity production at solar thermal electricity plants.

7. References

- [1] R. Tamme, D. Laing, and W. D. Steinmann, "Advanced thermal energy storage technology for parabolic trough," presented at the ISEC 2003: International Solar Energy Conference, Hawaii, USA, 2003.
- [2] D. Laing, D. Lehmann, M. Fiß, and C. Bahl, "Test Results of Concrete Thermal Energy Storage for Parabolic Trough Power Plants," *Journal of Solar Energy Engineering*, vol. 131, pp. 041007-041007, 2009.
- [3] D. Laing, W. D. Steinmann, R. Tamme, and C. Richter, "Solid media thermal storage for parabolic trough power plants," *Solar Energy*, vol. 80, pp. 1283-1289, 2006.
- [4] D. Laing, C. Bahl, T. Bauer, M. Fiss, N. Breidenbach, and M. Hempel, "High-Temperature Solid-Media Thermal Energy Storage for Solar Thermal Power Plants," *Proceedings of the IEEE*, vol. 100, 2012.
- [5] A. Stückle, "Analyse und Modellierung gekoppelter Regeneratoren zur Speicherung sensibler und latenter Wärme für den Einsatz in Dampfkraftwerken," in *Fortschritt-Berichte VDI - Energietechnik* vol. 6, ed. Düsseldorf, Germany: VDI Verlag GmbH, 2013.
- [6] D. Laing, W. D. Steinmann, P. Viebahn, F. Gräter, and C. Bahl, "Economic Analysis and Life Cycle Assessment of Concrete Thermal Energy Storage for Parabolic Trough Power Plants," *Journal of Solar Energy Engineering*, vol. 132, pp. 041013-041013, 2010.
- [7] Y. Jian, F. Bai, Q. Falcoz, and Z. Wang, "Control Strategy of the Module Concrete Thermal Energy Storage for Parabolic Trough Power Plants," *Energy Procedia*, vol. 69, pp. 891-899, 2015.
- [8] M. J. Peet, H. S. Hasan, and H. K. D. H. Bhadeshia, "Prediction of thermal conductivity of steel," *International Journal of Heat and Mass Transfer*, vol. 54, pp. 2602-2608, 2011.
- [9] H. Elmqvist and S. E. Mattsson, "Modelica - The next generation modeling language - An international design effort," presented at the Proceedings of the 1st World Congress on System Simulation, Singapore, 1997.
- [10] Modelica-Association, "Modelica Standard Library 3.2 - Free library from the Modelica Association to model mechanical (1D/3D), electrical (analog, digital, machines), thermal, fluid, control systems and hierarchical state machines," ed. <http://www.modelica.org> (accessed 14.11.2012): Modelica-Association, 2010.
- [11] H. Tummescheit, "Design and Implementation of Object-Oriented Model Libraries using Modelica, PhD Thesis ", ed. Lund, Sweden: Department of Automatic Control - Lund Institute of Technology, 2002.
- [12] Solutia-Inc., "Therminol VP-1 Heat Transfer Fluid by Solutia - Vapor Phase, Liquid Phase Heat Transfer Fluid (Technical Bulletin 7239115C)," ed. St. Louis, Missouri, USA: Solutia Inc., 2008.
- [13] M. Wetter, "Modelica Buildings Library - A free open-source library for building energy and control systems," ed. <http://simulationresearch.lbl.gov/modelica> (accessed: 11.02.2013): Lawrence Berkeley National Laboratory, 2013.
- [14] V. Gnielinski, "Neue Gleichungen für den Wärme- und den Stoffübergang in turbulent durchströmten Rohren und Kanälen," *Forschung im Ingenieurwesen A*, vol. 41, pp. 8-16, 1975.
- [15] T. D. Bui and T. R. Bui, "Numerical methods for extremely stiff systems of ordinary differential equations," *Applied Mathematical Modelling*, vol. 3, pp. 355-358, 1979.
- [16] L. R. Petzold, "A description of DASSL: A differential/algebraic system solver," ed. Albuquerque, New Mexico, USA: Sandia National Laboratories, 1982.

- [17] K. E. Brenan, S. L. Campbell, and L. R. Petzold, *Numerical Solution of Initial-Value Problems in Differential-Algebraic Equations*. Philadelphia, USA: SIAM - Society for Industrial and Applied Mathematics, 1996.
- [18] J. Pérez de Zabalza Asiain, "Desarrollo de sistemas innovadores de regulación/control de potencia térmica y temperatura de salida de sistemas de almacenamiento térmico avanzados para plantas termo solares - MSc Thesis," ed. Pamplona, Spain: Public University of Navarre (UPNA), 2016.
- [19] S. Wischhusen, "Simulation von Kältemaschinen-Prozessen mit MODELICA / DYMOLA - Diploma Thesis," ed. Hamburg, Germany: Hamburg University of Technology, Institute of Thermofluidynamics, 2000.
- [20] Dow-Chemical-Company, "Syltherm 800 - Silicone Heat Transfer Fluid - product data sheet," ed. Midland, USA: The Dow Chemical Company, 2001.
- [21] Z. Yang and S. V. Garimella, "Thermal analysis of solar thermal energy storage in a molten-salt thermocline," *Solar Energy*, vol. 84, pp. 974-985, 2010.
- [22] Modelica-Association, "Modelica® - A Unified Object-Oriented Language for Systems Modeling - Language Specification - Version 3.3," ed. <https://www.modelica.org> (accessed 14.11.2012): Modelica-Association, 2012.
- [23] I. Hernández Arriaga, F. Zaversky, and D. Astrain, "Object-oriented Modeling of Molten-salt-based Thermocline Thermal Energy Storage for the Transient Performance Simulation of Solar Thermal Power Plants," *Energy Procedia*, vol. 69, pp. 879-890, 2015.
- [24] F. Zaversky, "Object-oriented modeling for the transient performance simulation of solar thermal power plants using parabolic trough collectors - A review and proposal of modeling approaches for thermal energy storage, PhD Thesis," ed. Pamplona, Spain (<http://academica-e.unavarra.es/handle/2454/16705>): Public University of Navarre, 2014.
- [25] F. Zaversky, M. M. Rodríguez-García, J. García-Barberena, M. Sánchez, and D. Astrain, "Transient behavior of an active indirect two-tank thermal energy storage system during changes in operating mode – An application of an experimentally validated numerical model," *Energy Procedia*, vol. 49, pp. 1078-1087, 2014.
- [26] F. Zaversky, M. Sánchez, and D. Astrain, "Object-oriented modeling for the transient response simulation of multi-pass shell-and-tube heat exchangers as applied in active indirect thermal energy storage systems for concentrated solar power," *Energy*, vol. 65, pp. 647-664, 2014.
- [27] S. Relloso and J. Lata, "Molten Salt Thermal Storage: A Proven Solution to Increase Plant Dispatchability. Experience in Gemasolar Tower Plant," presented at the SolarPACES, Granada, Spain, 2011.
- [28] TEMA, "Standards of the Tubular Exchanger Manufacturers Association ", J. Harrison, Ed., ed. New York, USA: TEMA-Tubular Exchanger Manufacturers Association, Inc., 1999.
- [29] H. Lutz and W. Wendt, *Taschenbuch der Regelungstechnik - mit MATLAB und Simulink*, 8th ed. Frankfurt am Main, Germany: Wissenschaftlicher Verlag Harri Deutsch, 2010.
- [30] D. E. Seborg, T. F. Edgar, D. A. Mellichamp, and F. J. Doyle, *Process Dynamics and Control*, 3rd ed. Hoboken, New Jersey, USA: John Wiley and Sons, Inc., 2011.
- [31] A. E. Conradie and D. G. Kröger, "Performance evaluation of dry-cooling systems for power plant applications," *Applied Thermal Engineering*, vol. 16, pp. 219-232, 1996.
- [32] D. Bouskela and B. El Hefni, "ThermoSysPro Version 3.0," ed. Paris, France: EDF, 2012.
- [33] SimTech-Simulation-Technology, "IPSEpro - Integrated Process Simulation Environment," ed. <http://www.simtechnology.com> (accessed 30.4.2013), 2011.

- [34] R. K. Shah and D. P. Sekulic, *Fundamentals of Heat Exchanger Design*. Hoboken, New Jersey, USA: John Wiley and Sons, Inc., 2003.
- [35] W. Wagner and A. Kruse, *Properties of water and steam: the industrial standard IAPWS-IF97 for the thermodynamic properties and supplementary equations for other properties: tables based on these equations*: Springer-Verlag, 1998.
- [36] C. Marakkos, E. Stiliaris, E. Guillen, A. Montenon, and C. N. Papanicolas, "Temperature and Thermal Power Measurements for a Helical-Coil Steam Generator in a Thermal Storage Tank of Molten Solar Salt," in *SolarPACES*, Abu Dhabi, United Arab Emirates, 2016.
- [37] L. Guerreiro, D. Canavarro, and M. Collares Pereira, "Efficiency Improvement and Potential LCOE Reduction with an LFR-XX SMS Plant with Storage," *Energy Procedia*, vol. 69, pp. 868-878, 2015.
- [38] D. Canavarro, J. Chaves, and M. Collares-Pereira, "New dual asymmetric CEC linear Fresnel concentrator for evacuated tubular receivers," *AIP Conference Proceedings*, vol. 1850, 2017.